Spring 5-11-2024

UNBOXING THE COMPLICATED NEAR TERM CLIMATIC AND GEOMORPHIC HISTORY OF MARS

Joshua Matthew Williams
University of New Mexico - Main Campus

Joshua Williams

Candidate

Earth and Planetary Science

Department

This dissertation is approved, and it is acceptable in quality and form for publication:

Approved by the Dissertation Committee:

Louis Scuderi, Chairperson

Horton Newsom

Tyler Mackey

McKenzie Day

UNBOXING THE COMPLICATED NEAR TERM CLIMATIC AND GEOMORPHIC HISTORY OF MARS

by

JOSHUA MATTHEW WILLIAMS

B.S. Earth and Planetary Sciences, University of New Mexico, 2014
M.S. Geology, Western Washington University, 2017

DISSERTATION

Submitted in Partial Fulfillment of the
Requirements for the Degree of

Doctor of Philosophy

Earth and Planetary Sciences

The University of New Mexico
Albuquerque, New Mexico

March, 2024

DEDICATION

This dissertation is dedicated to my wife Rachael Williams, my son Pavel, and my daughter Rosalind.

ACKNOWLEDGEMENTS

First, I would like to thank my advisor, Lou Scuderi. I simply could not have had a better advisor for graduate school. After receiving my master's at Western Washington University, I had a few options for PhD, but when I heard Lou Scuderi was interested in mentoring me for my PhD the decision was easy, and I came back to New Mexico. Lou has been by far the best mentor I could have asked for. He continues to inspire, support, encourage and guide me along the way. Thank you to Horton Newsom for inspiring me to get into Planetary Sciences and for being an amazing advocate. I would also like to thank my other committee members for their help and patience in the process of achieving my goals: Mackenzie Day and Tyler Mackey. Thanks also to my NASA Technical Advisor, Tim McClanahan, who greatly aided with machine learning study. I would also like to thank the rest of the Goddard team; Maria Banks and David Hollibaugh Baker who gave their knowledge during the CNN cirque study. Thank you to NASA for funding me and my research. Thank you to Xi Gong who was an extremely good professor during my PhD courses.

I'd also like to thank all of the EPS administrative staff, specifically Paula Pascetti for putting up with endless questions. The department would cease to function without you.

Thank you to my fellow EPS graduate students, particularly those in Mars group: Foteine Dimitracopoulos, Zach Gallegos, Megan Hoffman, Sebastian Los, Dan Mason, Tim McNagle-Naughton and Matt Nellessen. I could not think of better people to work and collaborate with.

To my other friends: Rob Urias, Marty Crandall, Stephen Byars and John Donga for always listening to my never-ending tales of my geomorphology work. To Matt and Sara Dickens and who supported me in many ways during my PhD.

Lastly, I would like to thank my family for their love and endless support through this long process. To my grandmother Christine Williams, who always believed in me from the start, you are dearly missed. I want to especially thank my wife Rachael, for her endless support and love during this process, from the dark days of 2020 to our bright future.

UNBOXING THE COMPLICATED NEAR TERM CLIMATIC AND GEOMORPHIC HISTORY OF MARS

by

Joshua Matthew Williams

B.S. Earth and Planetary Sciences, University of New Mexico, 2014
M.S. Geology, Western Washington University, 2017
Ph.D., Earth and Planetary Science, University of New Mexico, 2024

ABSTRACT

It has long been thought that glacial processes were unlikely within the tropical regions of Mars. However, growing evidence, including this work has identified and quantified relic glacial forms within the equatorial regions. These findings have major implications for understanding Martian climate history and its sensitivity to changes in insolation. As well, the presence of ice in the equatorial region of Mars has significant implications for the past global redistribution of the water ice in the Martian cryosphere. In this manuscript, I clarify and refine our understanding of the morphology of glacial features in the equatorial zone by applying novel methods never used within the tropical regions on Mars. The results support the hypothesis that glacial processes were a common and major geomorphic force within the Martian equatorial zone. The work reported herein also helps to create pathways and prototype methods for future research on these forms on Mars.

TABLE OF CONTENTS

PREFACE

The three chapters of this dissertation are each a separate manuscript that have already been published or are in review and slated for publication in the near future. As such, each chapter stands alone with a structure mirroring the submitted manuscript: an introduction, methods, results, discussion, and conclusion. References are located after each chapter and are in the original formatting associated with each journal.

Each manuscript was written by me, and I am the first author on each. My PhD advisor, Dr. Louis A. Scuderi, is a co-author on every manuscript, and my NASA Technical Advisor, Dr. Timothy P. McClanahan, is a co-author on chapter 2. Dr. Horton Newsom is the coauthor of chapters 1 and 3.

CHAPTER ONE

Numerical Analysis of Putative Rock Glaciers on Mount Sharp, Gale Crater, Mars

Citation:

Williams, J. M., Scuderi, L. A., & Newsom, H. E. (2022). Numerical Analysis of Putative Rock Glaciers on Mount Sharp, Gale Crater, Mars. *Remote Sensing,* 14(8), 1887.

Abstract

The presence of buried glacial ice and putative extinct rock glaciers in Mars' equatorial regions has implications for understanding its climate history and sensitivity to changes in insolation and has significant implications for past global redistribution of the water ice cryosphere. We quantify the morphology of rock glacier- "like" features on the northern slopes of Aeolis Mons (known also as Mount Sharp) within Gale crater and use this information to evaluate a possible rock glacier origin for these forms. Detailed morphometric evaluation of cross and long profiles of these lobate features, which exhibit higher slopes at their heads, lower slopes at their distal edge, and a convex upward cross-sectional profile and oversteepened sides, resembles active terrestrial rock glaciers. However, the absence of a chevron wrinkle pattern and sublimation features could indicate extensive aeolian reworking and the lack of deflation could indicate a higher rock to ice mixture. The lack of cratering surfaces relative to the cratered surfaces that they overly could indicate a younger age and are possibly indistinguishable in age from the capping units of Mount Sharp, which may have once been more laterally extensive and may have been the source of these mass wasting forms.

1. Introduction

Documenting evidence of past glacial and periglacial activity in the equatorial region of Mars is critical for understanding its climatic history and its sensitivity to insolation variability due to changes in orbital elements. At present, the equatorial region, while cold, receives insolation sufficient to prevent significant ice formation; hence, it is currently impossible to form and retain substantial volumes of surficial ice [1–4]. In contrast, the polar regions of Mars display CO2-rich ice caps that wax and wane at their equatorward margins, suggesting current conditions that are seasonally sensitive to changes in insolation and temperature [5,6].

Mid-latitude glacial forms have been documented by a number of researchers [7–18]. Baker et al. [7], using crater size frequency distributions, constrained the dating of the youngest of these cold-based glacially emplaced lineated valley fill (LVF) and lobate debris apron (LDA) features to ~100 Ma. While water ice at these mid-latitude sites is not currently stable [19–22], using a high-resolution climate simulation model and assuming a modern Mars water cycle, found that mid-latitude, and even low-latitude, sites could maintain water ice at obliquity angles approaching 45◦ [20]. Current Mars obliquity is 25.1◦ [23].

While glacier-like forms (GLF) and viscous flow features (VFF) [13,14,24] have been documented in the mid-latitudes, evidence of past glaciation and periglacial activity along the equatorial portion of the dichotomy boundary is incomplete, inconclusive, and/or missing. The dichotomy boundary, a global escarpment, stands several kilometers above datum and separates the northern lowlands (~−8000 m elevation locally) from the southern highlands (~3000 m elevation locally) and is high enough to be the first portion of the equatorial region capable of supporting long-lived ice, assuming insolation conditions are favorable. Modeled past obliquity change suggests that glacial ice may have formed several times over the past 200 MY

[10,12,25–35]. This insolation change may have produced glacially modified forms in the equatorial portion of the dichotomy boundary [36], as well as periglacial features and rock glaciers [37,38].

During periods of high obliquity, past studies [39,40] suggest that Mars' low latitudes/equatorial regions would see a decrease in average annual temperatures (<−50 ◦C), not an increase. However, these studies typically did not include the radiative effects of water vapor and clouds, including exchanges with the subsurface and water vapor. Some current studies suggest that further warming of the atmosphere by clouds during periods of high obliquity (~35 ◦C) modifies water cycles and increases temperatures. Further, the interaction of atmospheric dust particles obscures surface ice, which aids in reducing summer sublimation and provides dust nuclei for cloud production [41]. Therefore, higher obliquity rates that are necessary to transport water ice equatorward could also warm and enhance glacial flow rates [40] in the near past.

In our analysis, we quantify the morphology of rock glacier- "like" features on Mount Sharp within Gale crater, located on the dichotomy boundary, and use this information to evaluate a possible rock glacier origin for these forms. While initially documented by Anderson and Bell [42], and interpreted as potential rock glacier features [38,43], a detailed morphometric evaluation of their form and their potential flow rates has not been conducted. Here, we also analyze the potential relationship between flow rates and insolation variability.

In addition to the lobate features investigated in this paper, other features in Gale crater, associated with Mount Sharp and the crater floor, possibly attributable to glacial activity, have been noted by authors in the past [38,43], and with the present level of investigation, the possibility of their glacial origins range from likely to disproven. Quantitative analysis of most

of the features has not been conducted, usually due to limitations of resolution or absence of topographic data. Long inverted channel deposits on the crater floor that have features in common with esker-type subglacial deposits have been rejected as glacial [43], but newer studies support a glacial hypothesis [44]. Recently, features on the rim of Gale crater and nearby, in the dichotomy boundary, have been attributed to glacial activity. Detailed examination of the Gale rim watersheds for Dulce Vallis and Peace Vallis (Figure 1c), in particular, have a sculpted surface and do not show evidence for a highly integrated and incised channel system consistent with the formation of the massive lake present in Gale, based on the lake deposits studied by Curiosity [45]. In addition, the crater rim topographic drainage floors contain inverted features, also suggestive of esker-like deposits [44,45]. Moreover, also present are rounded knobs on the slopes, extending down from the crater rim, that exhibit plucking on the downslope side, which are strongly similar to terrestrial roche moutonnée, formed from flowing ice [45]. Similar features have been observed on the lower slopes of Mount Sharp, but formed in the sediments making up the basement. Confirming this hypothesis from rover observations is difficult because the sub-ice features common in terrestrial situations are not present in the sediments, such as retention of glacial striations, and formation of glacial till with rounded and faceted boulders. Some features attributed to periglacial activity in Gale, including the presence of ice-wedge polygons [38], may be supported by observations in some formations in Gale [46].

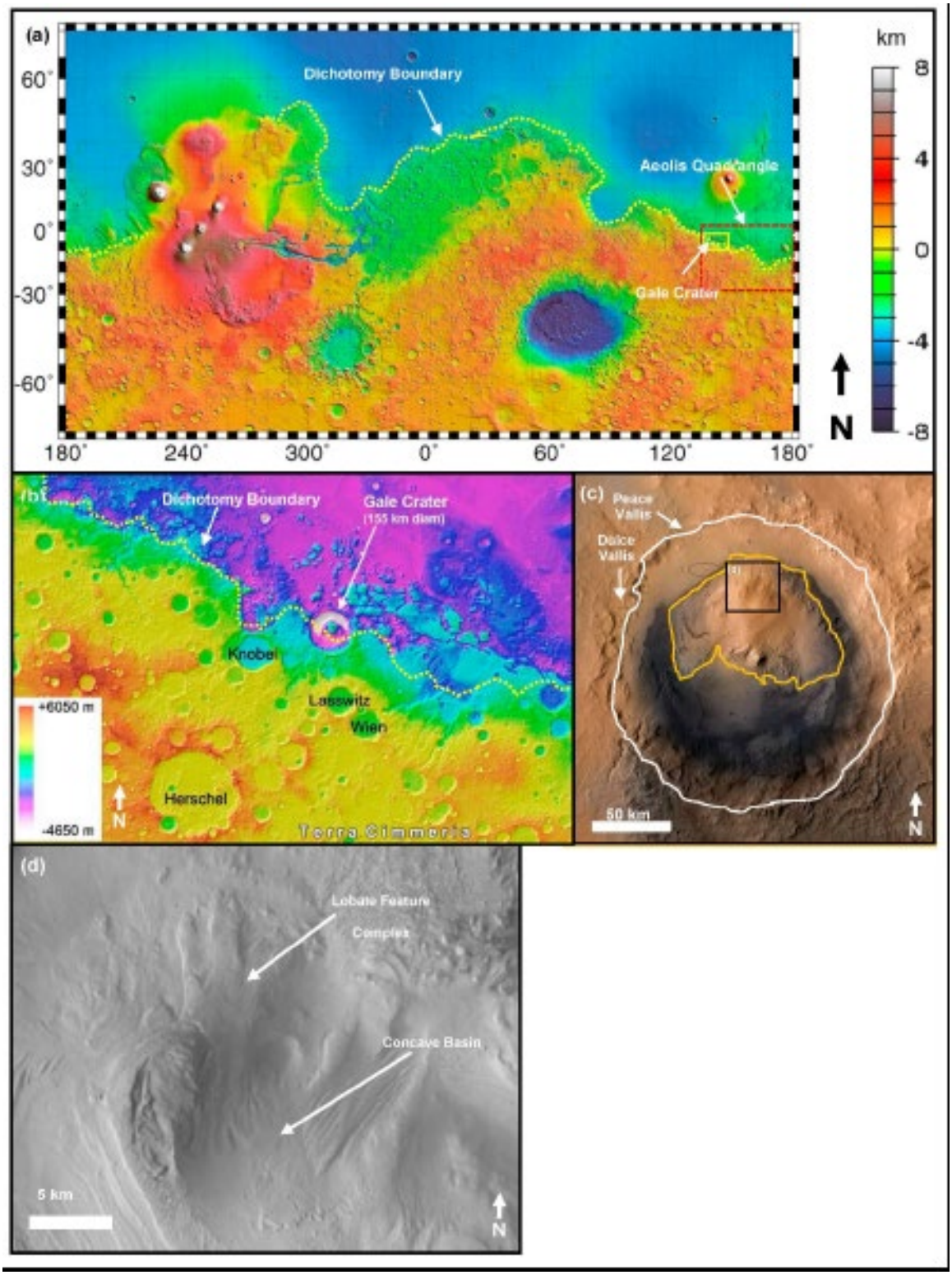

Figure 1. (a) Mars MGS MOLA Global Color Shaded Relief 463 m/pixel context map; (b) inset (yellow box) showing location of Gale crater and dichotomy boundary in the northwest portion

of low box) showing location of Gale crater and dichotomy boundary in the northwest portion of the Aeolis Quadrangle (red dashed box); (c) HRSC DEM combined with CTX image data and Viking Orbiter imagery. White: outline of Gale crater, yellow: outline of Mount Sharp. Brown oval: MSL landing ellipse; (d) HRSC image mosaic of the lobate feature complex and concave basin. Photo credit: NASA/JPL-Caltech/ESA/DLR/FU Berlin; Williams, J.M.

An aim of this study was to quantify the morphology of the lobate features located on the northern face of Mount Sharp (Figure 1), and if they conform to a rock glacier morphology, to use their form to determine flow rates and possible formation times. The significance of a periglacial origin would imply that cold-based processes may have had a much larger role in the formation of the current landscape than previously thought, implying that the Martian climate may have been more variable than previously believed.

1.2 Study Area

Gale (5.4◦S 137.8◦E) is a 154 km diameter crater located on the Martian dichotomy boundary (Figure 1a,b). Gale formed during the late Noachian to early Hesperian epochs (~3.6–3.8 Ga) [43,47,48] and has a thick sedimentary sequence, located in a central mound [47,49–51]. Gale's floor, known today as Aeolis Palus, consists of a series of fluvial and fluvial deltaic sandstones and conglomerates [47]. Infilling of materials on the crater floor began shortly after crater formation and continued throughout the late Hesperian period, and likely into the Amazonian [43,47,48]. Ground-based observations by the Curiosity rover Mars Science Laboratory (MSL) [47,50] have confirmed the presence of fluvial, deltaic, lacustrine and aeolian sedimentary deposits on the floor of Gale crater.

After infilling, sedimentary deposits in Gale crater were likely exhumed by aeolian-driven erosion events, resulting in the creation of the central mound, Aeolis Mons—informally known as Mount Sharp [42,48,50,51]. Mount Sharp consists of a 5.2 km thick sequence of layered sedimentary deposits (Figure 1c), mantling a central uplift and is ~100 km at its widest, with an area of ~6000 km2 [38,42,51] (Figure 1c). Interpretation from orbitally derived data suggests that this sedimentary complex consists of phyllosilicates and sulfates, suggesting both a lacustrine and aeolian origin [48,50,52–54]. Multiple aeolian-driven erosion events, resulting in unconformities in the rock record are also evidenced by the decameter thick sandstone Stimpson formation, unconformably overlying the lacustrine Murray formation [53]. These stratigraphic relationships suggest a period characterized by multiple transitions between sustained cold wet and cold dry climates [54].

A lobate feature complex and associated mass wasting deposits on the north face of Mount Sharp (Figure 1c,d) extends nearly to the floor of Gale crater [42]. The complex appears to originate north of a concave depression, located close to the summit of Mount Sharp [38,42,43], and consists of at least 11 discrete lobate features that display a range of preservation states, from pristine forms to highly degraded remnants. The stratigraphically higher lobate features mantle other more degraded lobate features, suggesting multiple episodes of activity. La Deit et al. [37] suggests that the lobate deposits formed after the deposition of the early Hesperian Syu1 unit, which they overly at their western edge, and before the deposition of the late Hesperian to Early Amazonian Cyu and Bu units. Le Deit et al. [37] and Fairén et al. [38] have suggested that these lobate features could have had an origin as rock glaciers, but to date, no quantitative analysis using morphometric data has been conducted to test this hypothesis.

1.3 Scientific Background

Currently, Mars is a cold hyper-arid planet, with little to no liquid water phase. Geomorphically, it is dominated by aeolian processes, with wind-formed features found across the equatorial to mid latitudes. Aeolian erosion is the likely driving mechanism for removing many tens of thousands of cubic kilometers of sediment across Mars [49,51]. This interpretation is based primarily on irregularly distributed large kilometer-scale features that include kilometer-scale yardangs, decimeter-scale escarpments, and finer-scale ventifacts [49,55–62]. Aeolian deposition and erosion are believed to have played an important role in the genesis of Mount Sharp within Gale crater [50].

1.3.1 Water, Ice and Glacial Forms on Mars

Water is currently stored as ice in the Martian cryosphere at high latitudes (45–90◦) in each hemisphere, primarily in the polar zone ice caps and other surface expressions, with buried ice deposits further equatorward [63]. A wide range of features at high latitudes, including banded terrain, lineated valley fills (LVF's) and lobate debris aprons (LDAs) [15,37], suggest past and possibly even relatively recent glacial and periglacial activity. This is especially evident in lobate forms, such as those seen in LDAs that are clearly visible at high latitudes on the dichotomy boundary. These features, including the broadening and extension of valleys that create isolated mesas, suggest a retreat of the dichotomy boundary by many hundreds of kilometers [12,29].

This range of glacial morphologies is interpreted as likely representing disparate formative/ evolutionary processes. LDA (Figure 2) and LVF are the most prevalent and common glacial modification features documented at higher latitudes [15]. LDAs, which are similar in appearance to terrestrial rock or debris glaciers [9,64], hold significant amounts of water ice, as

evidenced by data from the Shallow Radar (SHARAD) instrument on board the MRO [65], further supporting a glacial origin. However, LDA and LVF at lower latitudes are interpreted as having lost much, if not all, of their internal water ice and, therefore, represent relict forms that once held much larger ice volumes [9,14,19,66].

LDAs, found on low angled slopes and characterized by lobate outlines, have historically been interpreted to be evidence of debris flows, lubricated by basal ice or groundwater [9,66–69]. These features, typically sourced from arcuate valley-wall alcoves, extend onto lower adjacent lowlands and commonly exhibit down-valley flow, merging of multiple flow lines into a single main trunk valley form, and termination into lobe-shaped deposits.

They are usually found in fretted valleys, an abrupt escarpment of highly irregular planimetric configuration [60,70], on or near the dichotomy boundary and are widespread at mid-latitudes between 30◦ and 60◦ in both hemispheres [60]. However, while appearing analogous to terrestrial valley rock glaciers consisting of rocky debris material with interstitial pore ice [71–73], there is some question as to their actual genesis and formative process on Mars [66].

1.3.2 Terrestrial Rock Glacier Characteristics

Terrestrial rock glaciers, typically found in high mountainous regions, are defined as lobate, or tongue-shaped landforms. They consist of angular, poorly sorted rock debris, with either an ice core or an ice-cemented rock matrix, with a surface characterized by a coarse-grained debris layer that acts to insulate ice contained in the cemented matrix. Terrestrial rock glacier clasts range in size, from pebble (4 mm) to boulder (>25 cm). Rock glacier surfaces are characterized by a distinctive series of linear to arcuate ridges and furrows, commonly known as a “wrinkled” pattern (Figure 3a), that typically run perpendicular to the flow direction [74,75].

Active rock glacier distal slopes are typically over-steepened (Figure 3b), with slopes of up to 40–45◦ [76]. Source zones are associated with the heads of steep-walled valleys and are typically part of a wide amphitheater-like catchment, such as a cirque basin or nivation hollow [73,77,78] (Figure 4). The ice/water accumulation zones of these features are associated with scree-covered slopes at the base of a cliff or steep rocky headwall that have accumulated through periodic rockfall (Figure 4).

Rock glacier origin and formation models fall into three categories: (i) glacial (or former/relict glacial), (ii) permafrost, or (iii) landslide (mass wasting) (Figure 4) [79,80]. Glacial and permafrost models (Figure 4a,b) invoke the flow via creep, which acts through movement

between or within ice crystals, as ice behaves as a nonlinear viscous material [79]. In contrast, the landslide model (Figure 4c,d) postulates origins by mass-wasting emplacement [80].

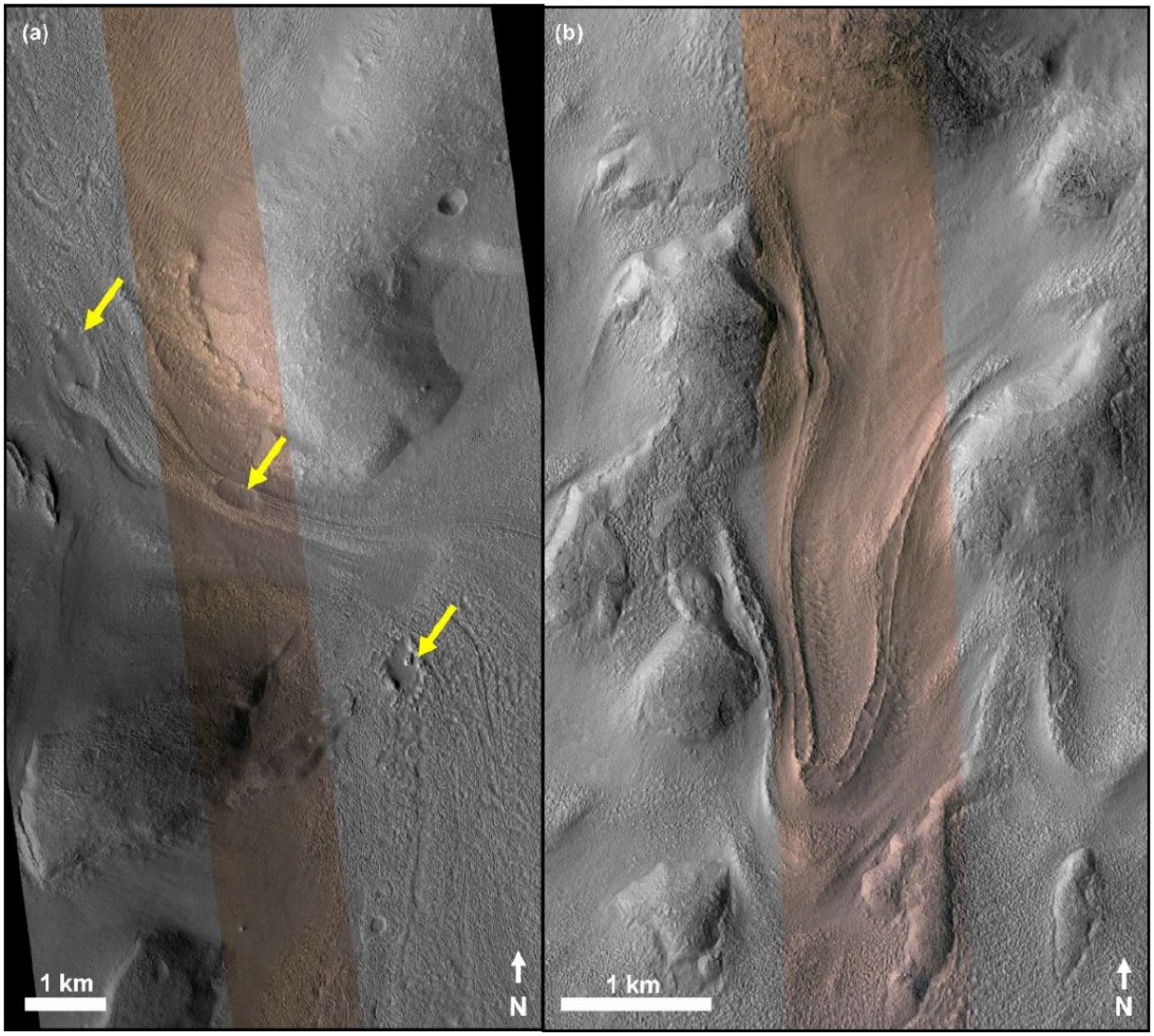

Figure 2. Examples of lobate debris aprons (LDA) in Deuteronilus Mensae (mid-latitude, Mars) and a tongue-shaped flow feature in eastern Hellas Planitia (mid-latitude, Mars): (a) Deuteronilus Mensae LDA. Feature shows possible sublimation pits (yellow arrows). HiRISE/MRO image ESP_028721_2225_MIRB; (b) tongue-shaped lobate flow feature along an interior crater wall with a length approximately 5 km, width of 1 km. Feature portrays a double inner ridge and raised outer margin and surface is generally devoid of impact craters. HiRISE/MRO image PSP_003243_1415_MIRB. Image credit: NASA/JPL.

The ‘Glacial’ model depends directly on the preservation of a thin (<50 m) body of ice, insulated by a mantle of rock debris [74,80]. In this model, the thin glacial-derived ice creeps at lower rates than traditional valley glacial bodies. The debris mantle acts as a protective layer from ablation; therefore, these features are ‘azonal’ and can cross climatic zones, allowing a longer active period, even after climatic conditions become unfavorable for glacial processes. A subcategory of the glacial model is the ‘Protalus rampart’ model, typically associated with debris covering snow or ice accumulations or micro-glaciers [80] (Figure 5). ‘Protalus lobes’ are generally not thought to be associated with glacial processes, yet do not necessarily require permafrost conditions. These features may be preserved depending on azonal conditions (debris thickness, altitude, aspect and thermal conditions) [82,83] (Figure 5).

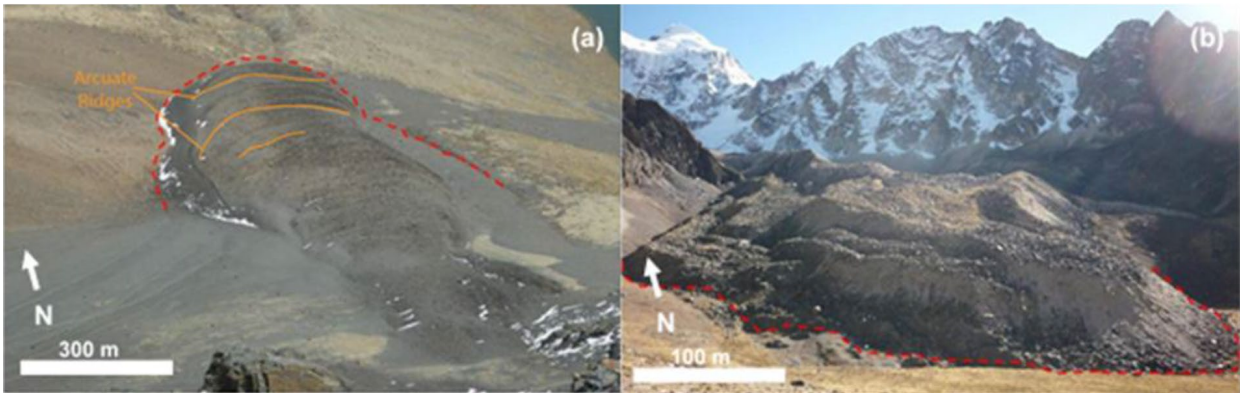

Figure 3. Terrestrial rock glacier Martian analogs. Bolivian rock glaciers; (a) well-defined arcuate ridges and depressions extent marked orange at Pico Austria, Tuni Condoriri region; (b) rock glacier front analog at Huayna Potosi, rock glacier with an over-steepened front slope ~43. Photo credit: S. Rangecroft, July 2011, August 2012.

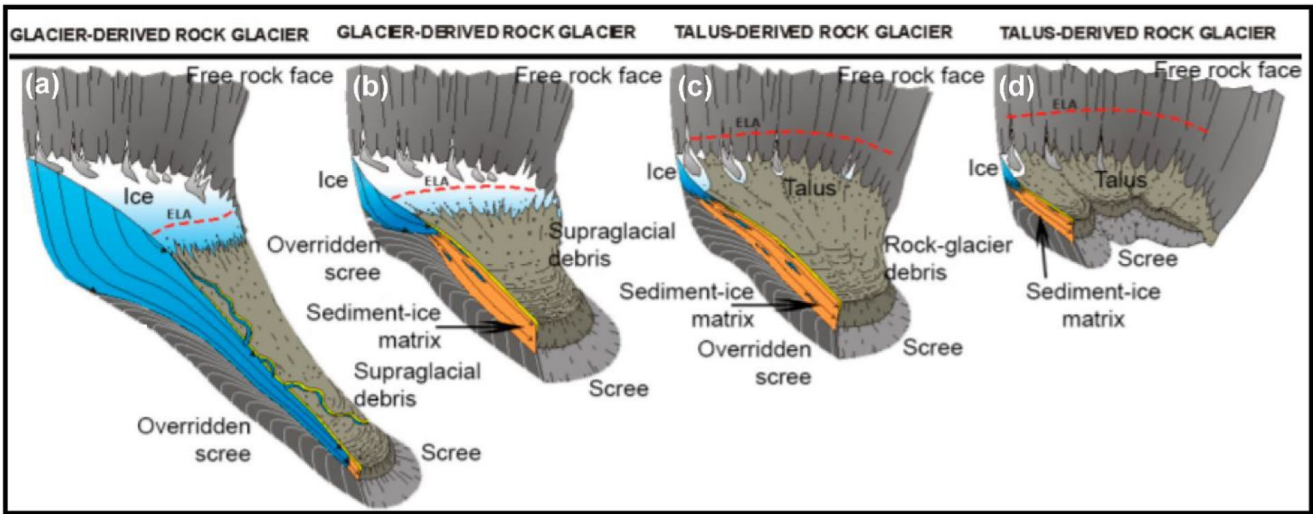

Figure 4. Glacier-derived rock glacier to talus-derived rock glacier examples. Images with higher elevation equilibrium lines (decreasing ice accumulation) towards the right. (a) Glacier-derived rock glacier, ELA present on glacial body; (b) glacier-derived rock glacier, ELA migrated up closer to rock face; (c) talus-derived rock glacier, ELA now above glacier body; (d) talus-derived rock glacier, ELA migrating further above glacier body. Figure adapted from Humlum et al. [81].

The 'Permafrost' model implies that the rock glacier ice is formed from freezing water injected under pressure or by ice segregation. This results in the formation of discrete layers or lenses of ice in freezing talus pore spaces, due to the migration and subsequent freezing of pore water [85]. Rock glacier features in this 'talus-derived' or 'ice-cemented' model typically have low flow rates due to ice creep in the pores and ice lenses associated with permafrost development. In this model, rock glaciers are typically found in climatic regimes with low precipitation and extreme temperature ranges [86]. However, the 'zonal' permafrost model implies a thermal condition, requiring an annual air temperature maximum of -1.5 °C, therefore, indicating relict or present-day permafrost [80].

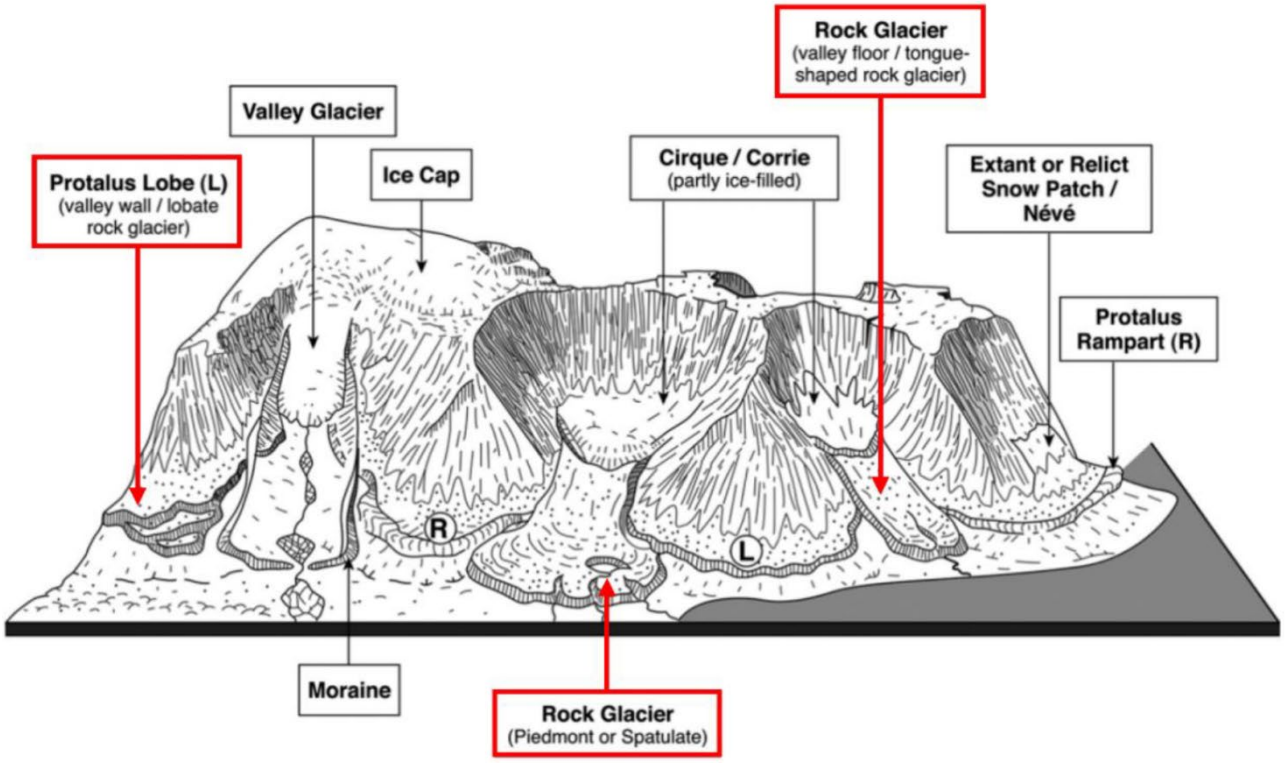

Figure 5. Three classifications of rock glaciers geometry; lobate rock glacier, piedmont/spatulate rock glacier and tongue-shaped rock glacier (indicated in red). After Humlum et al. [81], Martin Whalley [74], and Hamilton and Whalley [84].

The landslide genesis model implies that rock glaciers can be derived from rock avalanches [86,87]. Typically, these forms will not flow after emplacement. They can also be described as "instant" rock glaciers, as some rapid landslides or 'Bergsturtz/Sturtzstroms' fall on down-wasting/retreating glaciers [80] and are possibly a variation of the glacier ice core model. The three models produce forms that are, in theory, very similar, if not morphometrically identical. As such, it is important to note that the genesis for rock glaciers is widely debated, with no one theory accepted at this time. Ice content in terrestrial rock glaciers ranges from none (relict forms, no movement [64,88]), to minor ice (stagnant forms, minor movement) to a nearly 100% ice composition, with a variable thickness debris mantle (active forms). Transitions between these stages are continuous [64]. While identification of the ice to rock volume is

exceedingly difficult for terrestrial rock glaciers, studies have used ranges of rock/ice between 35/65 and 50/50 [89]. This range of compositions coupled with morphometrics (length, slope, height, surface curvature, etc.) can be used to reconstruct possible past flow dynamics. Virtually all terrestrial rock glaciers form in cryo-conditioned landscapes due to precipitation, groundwater or meltwater permeating into mechanically weathered debris, typically derived from headwalls and scarps, and subsequently freezing [90–92]. Surface mass exchange includes additions from snowfall, hoar frost, diamond dust and avalanche accumulations, as well as freezing rain, refreezing of meltwater, snow or ice melt, sublimation, redistribution through aeolian souring and calving of ice blocks at glacier terminus. For rock glaciers, the mass balance gradient differs significantly from debris-free glaciers; hence, debris cover can insulate glaciers from ablation [93]. Therefore, rock glaciers can persist in landscapes well beyond debris-free glaciers because they have a much longer response time to climate change [52].

1.4 Equations Controlling Rock Glacier Flow

Rock glaciers flow slowly, typically at a rate of <1 m/yr [94], an order of magnitude slower than pure ice glaciers [75,80,88]. Like traditional glaciers, they flow in response to stress produced by the gravity-driven deformation of ice, internal sediment/ice interactions, or by sliding at the ice–bed interface. Resistance to this strain depends on ice temperature, crystal structure, bed roughness, debris content, water pressure and other factors [95]. The surface pattern of transverse ridges and furrows is thought to be caused by fractures and debris bands, resulting from extensional flow [38,80].

Morphometric analysis of surface forms combined with calculations of the possible range of basal shear stress and subsequent flow rates can aid in determining whether they are in accord with similar rock glacier features on Earth.

Typically, basal shear stress (τ_b) is calculated as [96]:

$$\tau_b = \rho g h (\tan\alpha), \quad (1)$$

where, ρ is the average density of the glacial body (kg/m^3), g is the gravitational force of the planetary body, α is the slope at points along a transverse (center) of the form, from the head of the lobe to its distal end (Figure 6), while h is the height or thickness of the glacial body at each point along the central traverse.

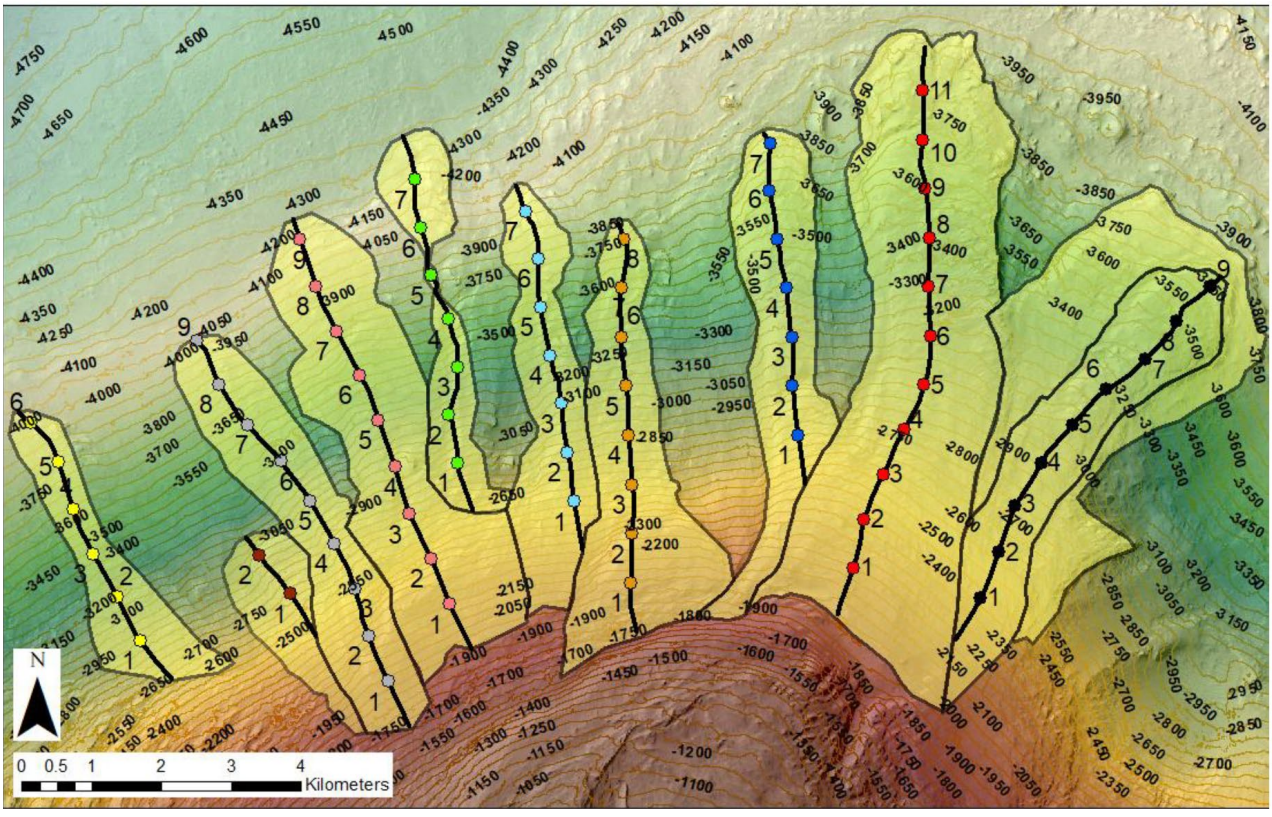

Figure 6. Lobate features on the north face of Mount Sharp. Eleven lobes mapped (0–10) and ten analyzed (1–10). Lobe (0) is overlapped and partially obscured by lobe (2), therefore, was not included in this study. Lobe-center transect lines with corresponding equidistant points.

Point colors indicate lobe color designation used in text. CTX base image: B16_016085_1750_XN_05S222W and CTX DEM derived from CTX stereo pairs P01_001422_1747_XN_05S222W and P18_008002_1748_XN_05S222W. Image: NASA/JPL-Caltech/MSSS; DTM: NASA/JPL-Caltech/MSSS/NHM; the stereo DTM processing was carried out at the Natural History Museum, London; slope and contour overlay map: Williams J.M.

Shear strain flow rate (") is calculated using the Glen-Nye Flow Law [78], which quantifies the relationship between creep and stress:

$$\varepsilon = k\,\tau_b^{n}, \tag{2}$$

where, " is the strain rate, k ($s^{-1}(kPa^{-3})$) is a constant defined by a material parameter that is dependent on the ice temperature, crystal orientation, impurity content and other factors [76,97–99], τ_b is the calculated basal shear stress (kPa) and n is the stress component constant. The exact value of the stress exponent for rock glaciers is typically difficult to determine [100], but it is at least larger than in the case where material moves as creep (i.e., Newtonian fluid). For pure Newtonian stresses, $n = 1$, while for pure non-Newtonian stresses, $n = 3$ [100]. Since rock glaciers rheology is complicated, relative to pure water ice glaciers and dominated by dislocations (non-viscous responses due to rock and ice mixture), the stress exponent for terrestrial rock glaciers is typically taken as 3 [76]. However, Mars' gravity is approximately 1/3rd of Earth and, therefore, due to reduced stress on the glacial body, ice deformation is dominated by grain-size dependent deformation ($n = 2$) [101]. In order to calculate the surface flow rate (U_s), we used the following formula [98]:

$$U_s = U_b + ((2k)/(n + 1))\,\tau_b^{n}, \tag{3}$$

where, U_b is the base velocity (m/s), Us is the surface velocity (m/s), k, *n* and τ_b defined above (Formula (2)). Since we are assuming a cold base glaciation and no basal slip, $U_b = 0$.

This gives us:

$$U_s = ((2k)/(n + 1))\tau_b^n, \quad (4)$$

Variables defined above (Formulas (2) and (3)).

1.5 Methodology

In order to assess evidence supporting the hypothesis of a glacial or periglacial origin of lobate features on Mount Sharp, we performed a numerical analysis on the lobate forms. We first extracted morphometric data from each lobate feature, compiled using high resolution orbitally derived imagery from two instruments on the Mars Reconnaissance Orbiter (MRO), the ~0.25 m/pixel resolution High Resolution Imaging Science Experiment (HiRISE) [102] and the ~6 m/pixel resolution Context Camera (CTX) [103].

A Geographical Information System (GIS) database, consisting of the CTX and HiRISE imagery and DEM data, and vector outlines and center transect lines of 10 lobate forms (Figure 6) was compiled using ArcMap 10.8.1. Because of significant overlap of lobe (0) only lobes 1–10 were retained for analysis. The boundary outline of each lobate form was captured with heads-up vectorization using the 3D Analyst Interpolate Polygon tool in ArcGIS. The Identify tool was used to capture equidistant points for flow analysis at ~700 m spacing along each transect (Figure 6). A finer extraction was not merited due to the resolution of the source data. The CTX DEM and HiRISE imagery were used in ArcGIS to derive slope, aspect, contour, and shaded-relief layers as well as cross sections. Lobe length and area, and the elevation profile

along each transect and cross-section, were calculated in ArcGIS and added to the database. Morphometric information for each of the lobate features is shown in Table 1.

The underlying ground elevation below each lobate feature was derived by creating a perpendicular line through each transect point drawn to the edge of the lobate feature (Figure 7a). A line drawn connecting the ground elevations at endpoints of each perpendicular (yellow arrows Figure 7a) was used to estimate the ground elevation below each transect point. Maximum thickness at each transect point (h) was then estimated by subtracting the underlying ground elevation from the lobate spot elevation (Figure 7b). We did not include basal scouring

and deepening effects as we believe these forms to be periglacial and therefore likely frozen to the underlying bedding at the time of formation.

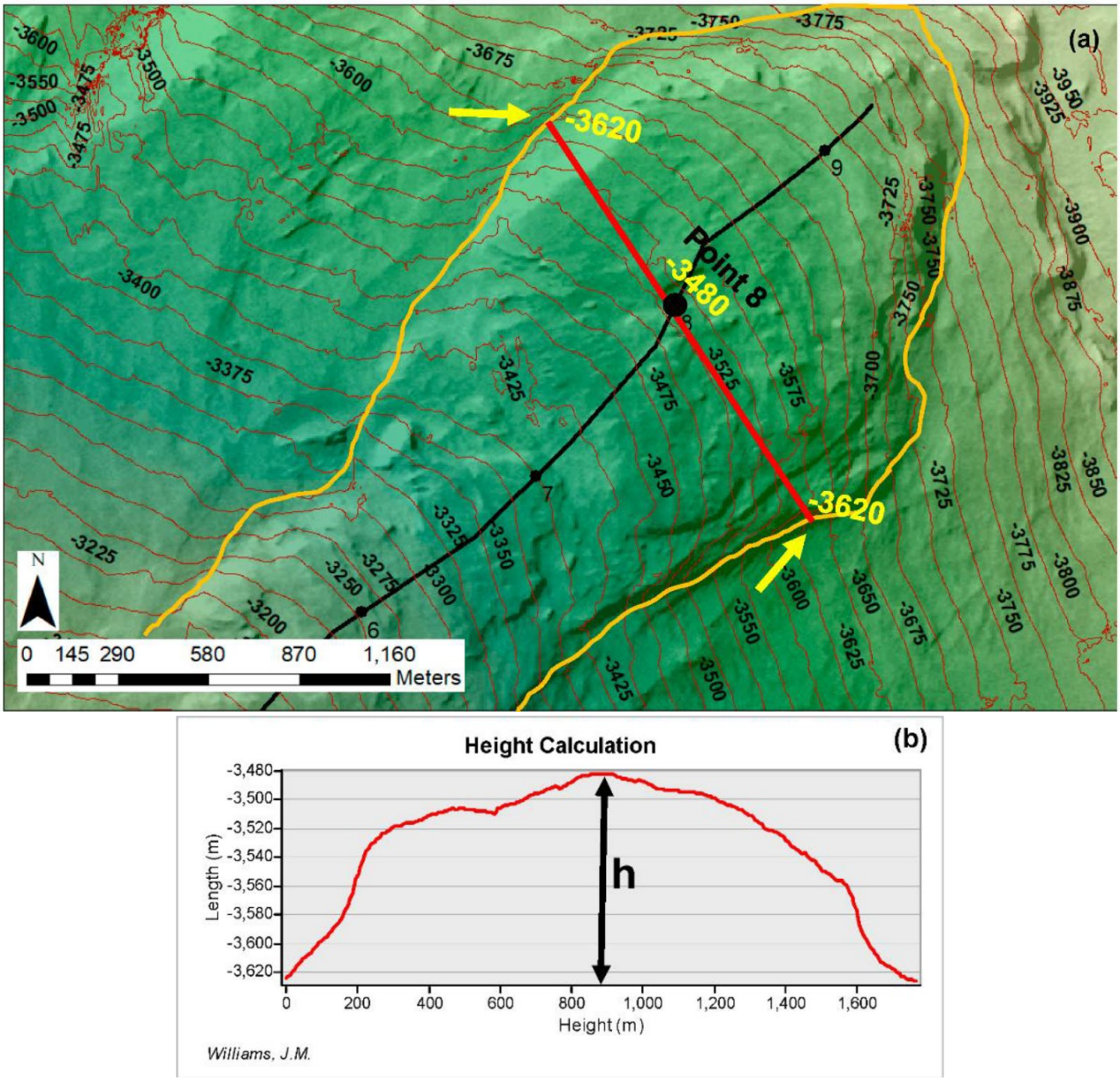

Figure 7. (a) Ground estimation method using bounding elevations of a perpendicular drawn line to a lobate feature boundary (orange line) and from the centerline transect point. In this example, the Point 1 elevation is -3000 m and basal elevation is -3100, giving a height of 100 m. (b) Basal elevation range below the cross-sectional profile and the underlying ground elevation with no basal scouring. The maximum thickness h corresponds to the center of the

transect line. Vertical exaggeration 10X. CTX image: B16_016085_1750_XN_05S222W. CTX DEM derived from CTX stereo pairs P01_001422_1747_XN_05S222W and P18_008002_1748_XN_05S222W. Image: NASA/JPL Caltech/MSSS; DTM: NASA/JPL-Caltech/MSSS/NHM; the stereo DTM processing was carried out at the Natural History Museum, London; slope and contour overlay map: Williams J.M.

The proportion of thickness attributable to rock and ice assuming admixtures ranging from 35/65 to a 50/50 basaltic rock/water ice mix was calculated at each location and used in subsequent flow modeling. Assuming modern ice content is zero, we added back ice from a 35/65 and a 50/50 basaltic rock/water ice mix and adjusted the past height with these percentages. The adjusted thickness (h) at the transect points (Figure 7b) was used to calculate basal shear stress (τ_b) (Formula (1)), where the average density (ρ) is the mixture of rock and ice (~1800 kg/m^3) with Martian gravity (g) of 3.711 m/s^2. Slope (α) was calculated for each transect point from the head of the lobe to its distal end (Figure 6).

Flow rate (ε) (Formula (2)) was calculated for a range of temperatures; the lowest estimated temperature value (-50 °C) has a flow parameter k of 3.6 x 10-^{18} ($s^{-1}(kPa)^{-3}$) while the rate for the highest possible temperature value is 0 °C and has a flow parameter k of 6.8 x 10^{-15} ($s^{-1}(kPa)^{-3}$) (Table 2). However, it is important to note that this simplified model did not account for possible hardening effects of suspended lithic fragments. At colder temperatures (-131 C to -50 ℃) the effect of particulates is hardening due to

tortuosity of ice flow paths around lithic particle and viscous drag of flowing ice. At warmer temperatures (-50 °C +) the effect of lithic particles actually impedes ice grain growth and thus retains creep within the GSS regime [101]. Glen Flow Law values were calculated for the lobe points using the estimated shear stress at both the 35/65 and 50/50 basaltic rock mix and water

ice for the lowest (-50 °C) and highest (0 °C) temperatures (Tables 2 and 3). Finally, we vertically integrated the strain rate to ice body surface flow velocity (Us) (Formula (4)) for both the lowest (-50 °C) and highest (0 °C) temperatures (Tables 2 and 3).

1.6 Analysis

Figure 8 illustrates our mapping of lobate forms interpreted as rock glaciers (Anderson et al., (2010; La Deit et al., 2013; Fairén et al., 2014), an ~20km long, low slope angle (~4.5%) lobate spatulate feature that is 10-12km at its widest, and the concave basin from which this spatulate feature originated. The spatulate form identified as a "fan-like" feature by Le Deit et al. (2013) and mapped as a mass wasting unit, extends from an elevation of ~ -3600m and reaches to a lower elevation of -4250m. It is sourced from the headwall and drainage of the concave basin that has a maximum elevation of +400m.

In contrast, the lobate forms extend downslope from a pronounced break in slope between -1100m and -1450m along an apparent northeast dipping bedding plane on the north side of Aeolis Mons. The longest and best-preserved lobate feature has a width of 1.8km, an area of 18.64 km2 and extends downslope ~8.5 km from this slope break (Fig. 8) to ~ -3595m. The lobate forms, unlike the relatively flat spatuate feature, exhibit surface slopes of ~10-12° that are similar to, and which appear to be draped unconformably on, Mt. Sharp's northern slopes. Their upper surfaces tend to exhibit a convex upward form in cross-section, a concave downslope surface that follows the underlying slope of Mt. Sharp (Fig. 7 Bottom, Fig. 9) and highly oversteepened terminal and side slopes estimated of up to 35o using shadow lengths. Both the convex upward cross-sectional form and oversteepened feature edges (Fig. 9) are typical of terrestrial rock glaciers (Fig. 2). These features, which have been interpreted to underlie the younger thin Bu capping member (La Deit et al., 2013), may be in part mass

wasting features derived from erosion of the Bu member and thus may be younger, rather than older than the Late Hesperian Bu unit.

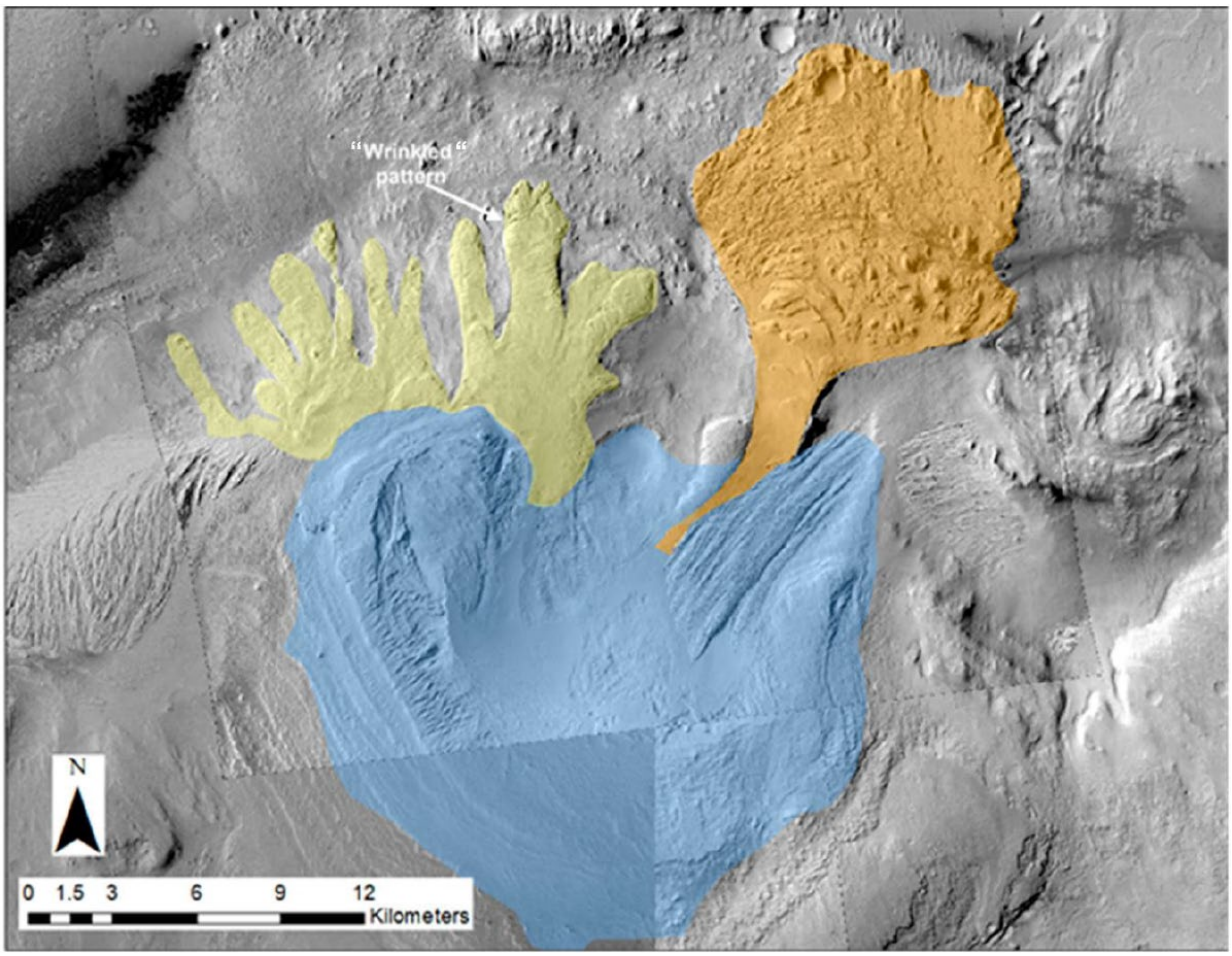

Figure 8. CTX Mosaic image of the north Mount Sharp features. Yellow: Lobate Feature Complex; Orange: Spatulate feature; Blue: Concave Basin. Slope break occurs at the boundary of the concave basin and the upper edge of the lobate feature complex boundary. Background image credit: NASA/JPL-Caltech/ESA/DLR/FU Berlin.

While the composition of the lobes is uncertain, they most likely comprise the capping Bu sedimentary unit aeolian lithologies, identified by Le Deit et al. [37] and Anderson et al. [52]. Analysis of lobate feature surface roughness indicates that the surfaces have few boulders and, in general, display a relatively smooth texture. Past studies [38] have suggested that, on a coarser

scale, and similar to terrestrial rock glacier analogs, the lobate surfaces exhibit arcuate ridges, furrows and a wrinkled pattern, consistent with pressure ridges (Figures 2 and 3). However, on further study, the aforementioned wrinkled pattern or pressure ridges texture are not arcuate, but rather appear to be linear, finely lamented features, similar to that of the nearby Light-Toned Yardang Unit (LTYu) [104] (Figure 11). Further, the average spacing between ridges is virtually identical, on average ~93 m (Figure 11). This suggests that the pattern seen on the lobate features

are actually aeolian reworking of the surface and not pressure ridges associated with rock glaciers.

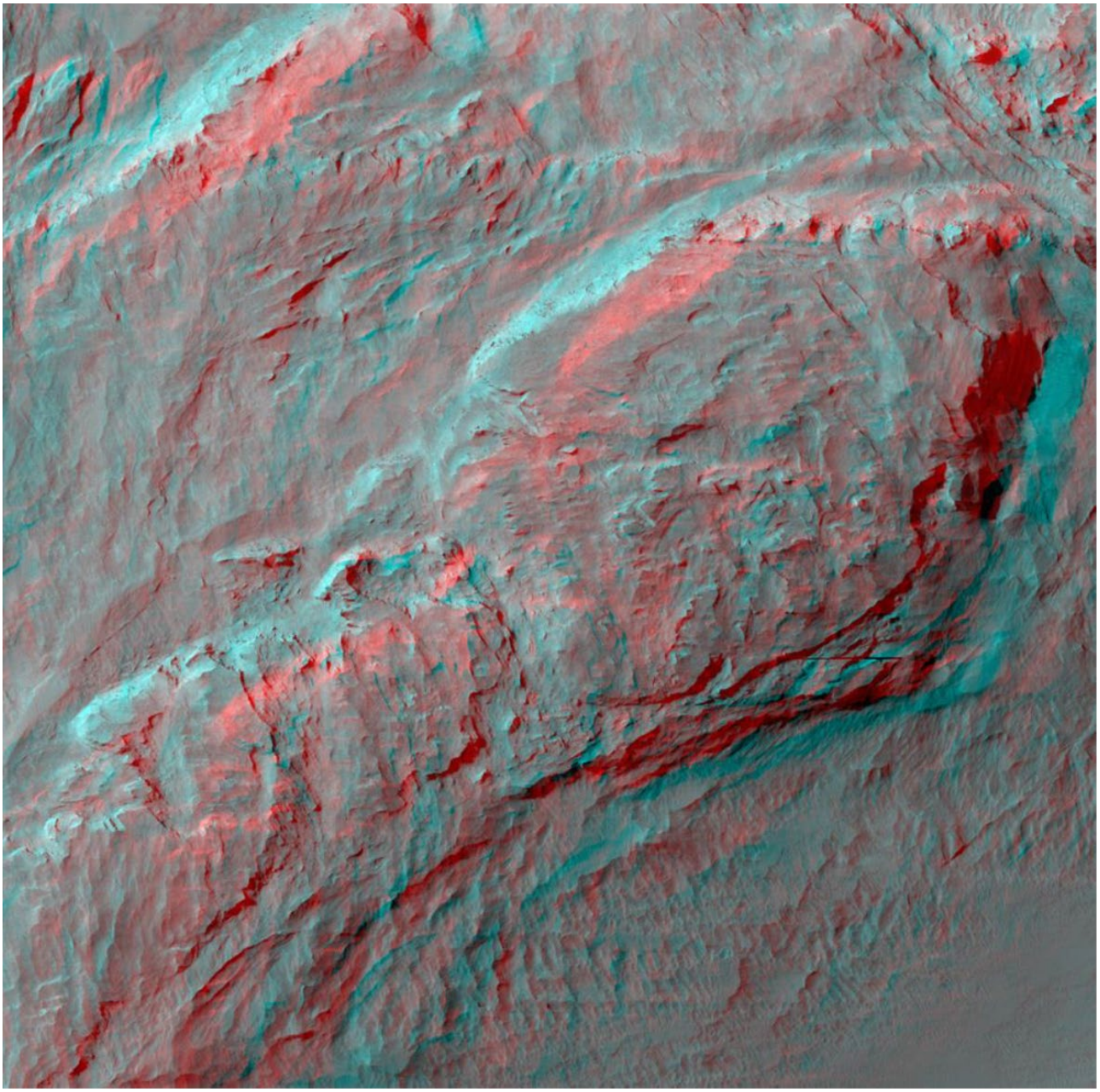

Figure 9. Anaglyph of lobate form shown in Figure 7. This feature has a convex cross profile with oversteepened distal and lateral sides. Image derived from HiRise Images ESP_018287_1755_ESP_018788_1755. Credit: NASA/JPL/University of Arizona.

Lobe degradation appears to increase towards the west of the complex, with higher preservation states typically associated with higher standing lobes towards the east that override older, more degraded lobes (Figures 6 and 12), suggesting multiple episodes of deposition. The ten lobes analyzed range in length from 1.74 km (dark red (9) lobe) to 8.5 km (red (1) lobe), with a mean length of 5.63 km (Figure 12a). The longest lobate form (red in Figure 12a) exhibits a decreasing slope, from head to terminus, with slope angles from 17 to 15 for points 1–5, 12 to 14 for points 6–8, and 9 to 12 points 9–11 (Table 1). Surface slopes for the remainder of lobes range from 10.63 (blue (3) lobe) to 23.04 (dark red (9) lobe), with a mean of ~19.35 (Figure 12b). The lobate feature complex heights ranging from ~19.55 m (pink (7) lobe) to 123.18 m (red (1) lobe), with an average of ~59.59 m. The red (1), black (2) and blue (3) lobes have the largest calculated heights and are the best preserved. The red lobe overlies portions of the blue lobe (Figure 12c).

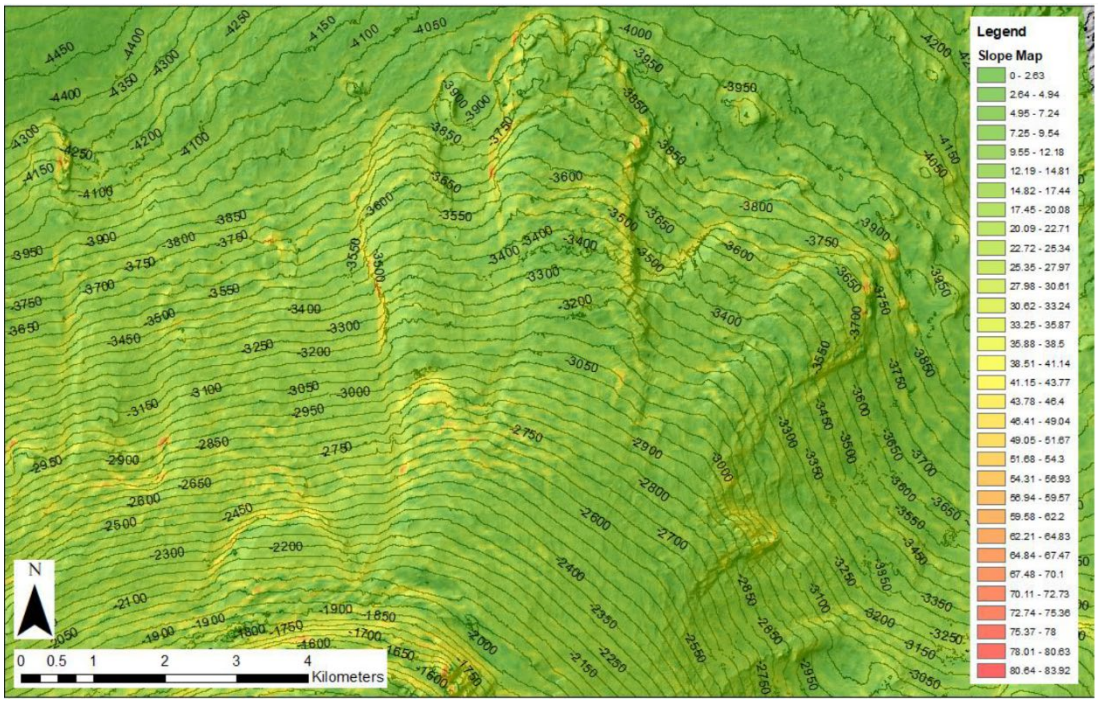

Figure 10. CTX DEM-derived Slope Map with contour 50 m interval. Slope map and contour created from CTX DEM. Image covers 6 of the 10 lobes reviewed in this study due to higher preservation states. Image derived from HiRISE images ESP_018788_1755, slope map created

in ArcGIS 10.8.1 using CTX DEM derived from CTX stereo pairs P01_001422_1747_XN_05S222W and P18_008002_1748_XN_05S222W. Image: NASA/JPL-Caltech/MSSS; DTM: NASA/JPL-Caltech/MSSS/NHM; the stereo DTM processing was carried out at the Natural History Museum, London; slope and contour overlay map: Williams J.M.

Calculated basal shear stress for the longest lobe, red (1), shows a decreasing trend from its head to its terminus; a trend is shared by all of the forms. For this lobate form, the calculated basal shear stress for a 35/65 rock/water ice mixture ranges from 93.85 kPa to 399.14 kPa, and is 122.00 kPa to 518.89 kPa for a 50/50 mix (Table 1). For the group of lobate features in the complex, the average surface flow rate calculations (Formula (4)) for the coldest modeled temperatures (-50 °C) indicate very slow mean rates of 4.85×10^{-4} m/yr for a 35/50 mix of rock and water ice and 1.02×10^{-3} m/yr for a 50/50 mix. Conversely, flow rates for warmer conditions (0 °C) were, on average, 0.91 m/yr for the 35/65 mix and 1.93 m/yr for the 50/50 mix (Tables 2 and 3).

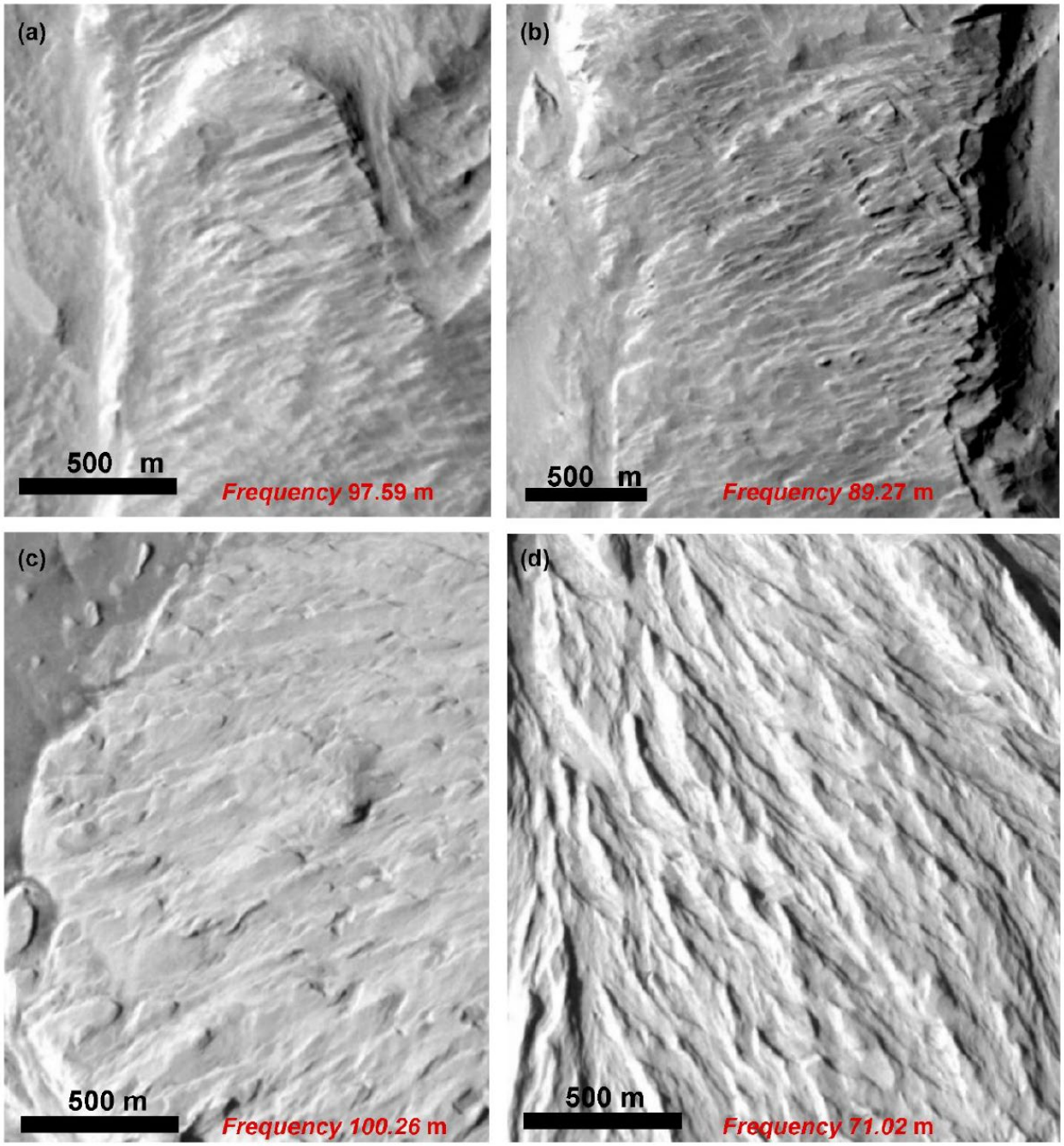

Figure 11. Lamented features examples on lobate feature complex and Mount Sharp light-toned unit. Frequency average of the two features is 93.43 m and for the Mount Sharp light-toned units frequency averages are 91.94 m. (a) Detailed image of finely lamented features of the medial portion of the blue (3) lobe. Frequency of lamented features ~97.59 m on average; (b) Detail image of finely lamented features of the medial/distal portion of the red (1). Frequency of

lamented features ~89.27 m on average; (c) detailed image of finely lamented features of the Light-Toned Yardang Unit (LTYu). Frequency of lamented features ~100.26 m on average; (d) detailed image of finely lamented features of Light-Toned Yardang Unit (LTYu). Frequency of lamented features ~71.02 m on average. Background image credit: NASA/JPL.

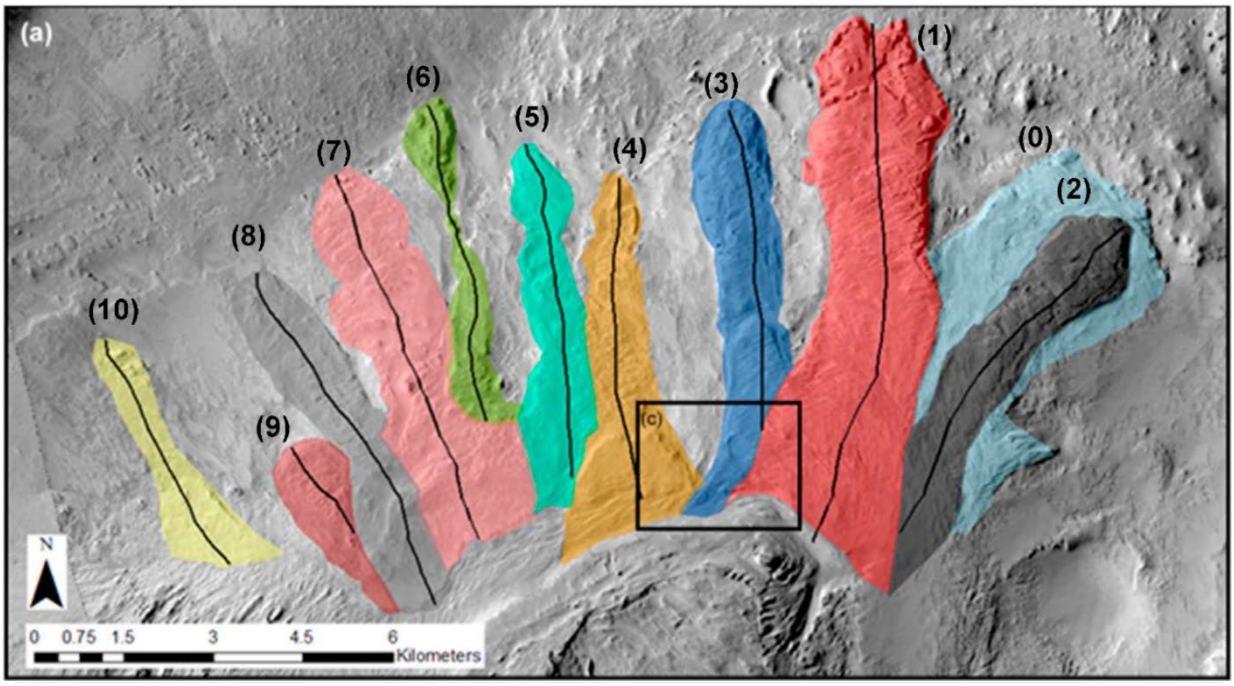
(a)
(0)
(1)
(2)
(3)
(4)
(5)
(6)
(7)
(8)
(9)
(10)
(c)
N
0 0.75 1.5 3 4.5 6
Kilometers

(b)

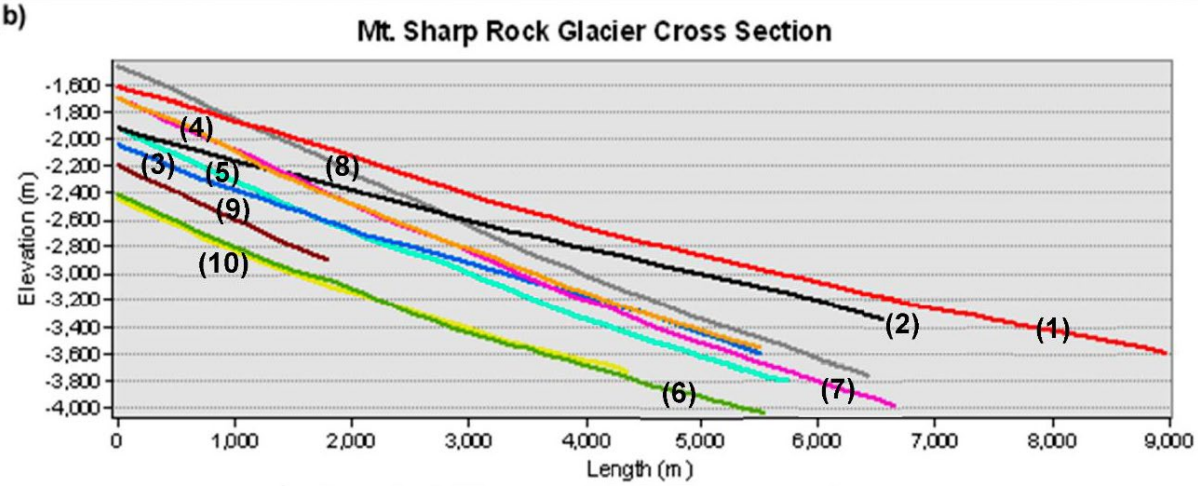
Mt. Sharp Rock Glacier Cross Section
Elevation (m)
-1,600
-1,800
-2,000
-2,200
-2,400
-2,600
-2,800
-3,000
-3,200
-3,400
-3,600
-3,800
-4,000
0
1,000
2,000
3,000
4,000
5,000
6,000
7,000
8,000
9,000
Length (m)
(1)
(2)
(3)
(4)
(5)
(6)
(7)
(8)
(9)
(10)

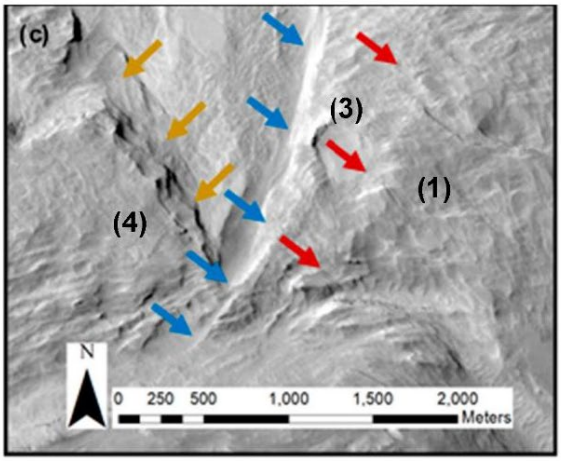
(c)
(1)
(3)
(4)
N
0 250 500 1,000 1,500 2,000
Meters

Figure 12. (a) Mount Sharp Rock Glacier complex with lobes and central traverse lines identified. Blue (3) lobe (right) is highly degraded and mantled and therefore not included in this analysis. Figure 12. (a) Mount Sharp Rock Glacier complex with lobes and central traverse lines identified. Blue (3) lobe (right) is highly degraded and mantled and therefore not included in this analysis. Scarp in the Bu unit of LeDeit et al. [37] occurs at the upper edge of the orange (4), blue (3) and red (1) lobate forms. Boxed area is context location for [c]; (b) profiles down the center transverse of the ten lobate features deposits located on the north face of Mount Sharp (Figure 1d). No vertical exaggeration: (c) overprinting lobes, red (1) lobe (Red Arrows) overlies the blue (3) lobe (Blue arrows) that overlies orange (4) lobe (orange arrows). CTX image: G01_018788_1754_XN_04S222W; background image credit: JPL/NASA.

The fastest calculated flow rates are associated with the best-preserved lobes at 0 °C and a 50/50 ice/rock mix (Red (1): 6.36 m/yr.; Black (2): 6.11 m/yr.) (Tables 1–3) and averages ~1.93 m/yr. for all 10 lobes. Flow rates are orders of magnitude slower for the same mixture at -50 °C (mean flow rate of ~0.001 m/yr.). A more likely 35/65 rock ice mix, based on the finer-grained composition of the aeolian capping units on Mount Sharp in a periglacial environment would suggest flow rates approximating 0.92 m/yr. at a temperature of 0 °C.

Table 1. Basal Shear Stress data for the Red (1) lobate feature shown in Figure 12a. Points 1–11 correspond to sites where flow rates were estimated (see Figure 6 for locations). Slope outliers may exist due to sampling issues, such as automated regular spacing to remove heads up vectorization sampling bias.

Red Lobe												
Basal Shear Stress $\tau_b = \rho g h(\tan \alpha)$												
Point	Slope (deg)	Elevation (m)	Basal Elevation Calculation (m)	Adjusted Lobe Height (m)	100% Rock Thickness (m) (Current)	35% Ice, 65% Rock Thickness (m) (Low)	50% Ice, 50% Rock Thickness (m) (High)	Tb (Basal Shear Stress) Pure Ice (kPa)	35% Ice, 65% Rock τ_b (Basal Shear Stress) Rock/Ice mix (kPa)	50% Ice, 50% Rock τ_b (Basal Shear Stress) Rock/Ice mix (kPa)		
1	17.41	−2252	−2331	−79	79	122	158.20	84.38	254.90	331.37	Density of Rock/Ice Mix (ρ)	1800 kg/m^3
2	14.31	−2434	−2494	−60	60	93	120.96	52.50	158.59	206.16	Density of Ice (ρ)	917 kg/m^3
3	14.50	−2624	−2659	−35	35	54	70.62	31.07	93.85	122.00	Gravity on Mars	3.71 m/s^2
4	16.65	−2836	−2887	−51	51	78	101.12	51.44	155.39	202.00	Middle lobe Length	8.5 km
5	14.61	−3020	−3069	−49	49	75	97.58	43.27	130.71	169.92	Average Height	83 m
6	12.99	−3169	−3213	−44	44	68	87.88	34.47	104.13	135.37	Average Slope	13°
7	13.99	−3312	−3404	−92	92	142	184.04	77.98	235.57	306.24	35% Ice, 65% Rock Average Basal Shear Stress	193 kPa
8	13.89	−3456	−3613	−157	157	242	314.06	132.13	399.14	518.89		
9	8.86	−3630	−3750	−120	120	185	240.04	63.66	192.30	249.99	50% Ice, 50% Rock Average Basal Shear Stress	8.5251 kPa
10	6.36	−3717	−3829	−112	112	172	224.14	42.48	128.34	166.84		
11	12.77	−3838	−3954	−116	116	179	232.10	89.46	270.25	351.32		

Table 2. Surface Flow Calculations for the Red (1) lobate feature located on the north slope of Mount Sharp. Upper table for temperature of -50 °C. Lower table for temperature of 0 °C. Points 1–11 correspond to the data sites located on the Red (1) lobate feature (see Figure 6 for locations). Surface Flow Rate (m/yr) from (Formula (4)). Values of the flow parameter k for shear stress n = 2, for 0 °C = 6.8 x 10^{-15}, and for -50 °C = 3.6 x 10^{-18}. Units as in Equations (1), (2) and (4).

	Temp (−50 °C) 35% Ice, 65% Rock					Temp (−50 °C) 50% Ice, 50% Rock						Temp (−50 °C) 35% Ice, 65% Rock	Temp (−50 °C) 50% Ice, 50% Rock
Point	m/s	=	k	τ	^n	m/s	=	k	τ	^n	Point	m/yr	m/yr
1	1.9×10^{-11}	=	3.6×10^{-18}	255	2	5.9×10^{-4}	=	3.6×10^{-18}	331	2	**1**	0.0005984	0.0007780
2	5.6×10^{-12}	=	3.6×10^{-18}	159	2	1.7×10^{-4}	=	3.6×10^{-18}	206	2	**2**	0.0001771	0.0002302
3	1.1×10^{-12}	=	3.6×10^{-18}	94	2	3.6×10^{-5}	=	3.6×10^{-18}	122	2	**3**	0.0000362	0.0000471
4	4.5×10^{-12}	=	3.6×10^{-18}	155	2	1.4×10^{-4}	=	3.6×10^{-18}	202	2	**4**	0.0001421	0.0001848
5	3.0×10^{-12}	=	3.6×10^{-18}	131	2	9.7×10^{-5}	=	3.6×10^{-18}	170	2	**5**	0.0000971	0.0001262
6	1.7×10^{-12}	=	3.6×10^{-18}	104	2	5.5×10^{-5}	=	3.6×10^{-18}	135	2	**6**	0.0000555	0.0000721
7	1.8×10^{-11}	=	3.6×10^{-18}	236	2	5.9×10^{-4}	=	3.6×10^{-18}	306	2	**7**	0.0005946	0.0007730
8	9.2×10^{-11}	=	3.6×10^{-18}	399	2	2.9×10^{-3}	=	3.6×10^{-18}	519	2	**8**	0.0029130	0.0037870
9	1.6×10^{-11}	=	3.6×10^{-18}	192	2	5.1×10^{-4}	=	3.6×10^{-18}	250	2	**9**	0.0005168	0.0006718
10	6.8×10^{-12}	=	3.6×10^{-18}	128	2	2.1×10^{-4}	=	3.6×10^{-18}	167	2	**10**	0.0002149	0.0002794
11	3.1×10^{-11}	=	3.6×10^{-18}	270	2	9.8×10^{-4}	=	3.6×10^{-18}	351	2	**11**	0.0009869	0.0012830
											Average	**0.0005757**	**0.0007484**

Table 2. *Cont.*

Temp (0 °C) 35% Ice, 65% Rock						Temp (0 °C) 50% Ice, 50% Rock						Temp (0 °C) 35% Ice, 65% Rock	Temp (0 °C) 50% Ice, 50% Rock
Point	**m/s**	**=**	**k**	**τ**	**ˆn**	**m/s**	**=**	**k**	**τ**	**ˆn**	**Point**	**m/yr**	**m/yr**
1	3.5×10^{-8}	=	6.8×10^{-15}	255	2	1.1×10^{0}	=	6.8×10^{-15}	331	2	**1**	1.13039	1.46951
2	1.0×10^{-8}	=	6.8×10^{-15}	159	2	3.3×10^{-1}	=	6.8×10^{-15}	206	2	**2**	0.33454	0.43490
3	2.1×10^{-9}	=	6.8×10^{-15}	94	2	6.8×10^{-2}	=	6.8×10^{-15}	122	2	**3**	0.06840	0.08892
4	8.5×10^{-9}	=	6.8×10^{-15}	155	2	2.6×10^{-1}	=	6.8×10^{-15}	202	2	**4**	0.26850	0.34905
5	5.8×10^{-9}	=	6.8×10^{-15}	131	2	1.8×10^{-1}	=	6.8×10^{-15}	170	2	**5**	0.18333	0.23834
6	3.3×10^{-9}	=	6.8×10^{-15}	104	2	1.0×10^{-1}	=	6.8×10^{-15}	135	2	**6**	0.10479	0.13622
7	3.5×10^{-8}	=	6.8×10^{-15}	236	2	1.1×10^{0}	=	6.8×10^{-15}	306	2	**7**	0.10479	1.46010
8	1.7×10^{-7}	=	6.8×10^{-15}	399	2	5.5×10^{0}	=	6.8×10^{-15}	519	2	**8**	1.12315	7.15315
9	3.1×10^{-8}	=	6.8×10^{-15}	192	2	9.7×10^{-1}	=	6.8×10^{-15}	250	2	**9**	5.50242	1.26897
10	1.2×10^{-8}	=	6.8×10^{-15}	128	2	4.0×10^{-1}	=	6.8×10^{-15}	167	2	**10**	0.97613	0.52778
11	5.9×10^{-8}	=	6.8×10^{-15}	270	2	1.8×10^{0}	=	6.8×10^{-15}	351	2	**11**	0.40598	2.42343
											Average	**1.08744**	**1.41367**

Table 3. Basal Shear Stress and Surface Flow data averages for all 10 lobate forms shown in Figure 12a.

Lobe Complex Study											
Density of Rock (ρ)	**1800 kg/m^3**	**Basal Shear Stress** $\tau_b = \rho g h (\tan \alpha)$						**Surface Flow Rate** $U_s = ((2A)/(n+1))\ \tau_b^n h$			
Density of Ice (ρ)	**916.7 kg/m^3**										
Gravity on Mars	**3.711 m/s^2**										
Lobe Color (#)	**Average Slope (deg)**	**Lobe Length (km)**	**Average Height (m)**	**35% Ice, 65% Rock Reconstructed Height (m)**	**50% Ice, 50% Rock Reconstructed Height (m)**	**35% Ice, 65% Rock Average Basal Shear Stress (kPa)**	**50% Ice, 50% Rock Average Basal Shear Stress (kPa)**	**Temp (−50 °C) 35% Ice, 65% Rock (m/yr)**	**Temp (−50 °C) 50% Ice, 50% Rock (m/yr)**	**Temp (0 °C) 35% Ice, 65% Rock (m/yr)**	**Temp (0 °C) 50% Ice, 50% Rock m/yr**
Red (1)	13.30	8.50	123.18	189.51	246.36	193.01	250.92	5.76×10^{-4}	7.48×10^{-4}	1.087	1.414
Black (2)	13.45	6.56	84.92	130.64	169.84	212.12	275.75	6.91×10^{-4}	8.99×10^{-4}	1.306	1.697
Blue (3)	10.63	4.98	100.94	155.30	201.89	299.82	389.76	1.49×10^{-3}	3.27×10^{-3}	2.810	6.173
Orange (4)	20.73	5.93	52.27	80.42	104.54	200.41	260.53	6.61×10^{-4}	1.45×10^{-3}	1.248	2.743
Light Blue (5)	23.04	5.33	47.56	73.17	95.12	206.10	267.92	4.18×10^{-4}	9.17×10^{-4}	0.789	1.733
Green (6)	22.39	5.68	35.92	55.26	71.83	181.19	235.54	3.44×10^{-4}	7.56×10^{-4}	0.650	1.427
Pink (7)	22.95	6.68	19.55	30.08	39.11	86.50	112.45	7.55×10^{-5}	1.66×10^{-4}	0.143	0.313
Grey (8)	21.40	6.35	33.84	52.06	67.68	156.46	203.40	1.54×10^{-4}	5.20×10^{-4}	0.291	0.982
Dark Red (9)	22.91	1.74	56.54	86.98	113.08	249.92	324.89	3.63×10^{-4}	1.23×10^{-3}	0.685	2.316
Yellow (10)	16.64	4.55	41.21	63.40	82.42	130.18	169.23	8.24×10^{-5}	2.78×10^{-4}	0.156	0.526

Close examination of HiRISE imagery of the 10 lobate features reveals a near absence of craters of almost all sizes. Again, barring burial or removal by subsequent erosion, this suggests a young age for these features. Le Deit et al. [37] noted that no scarp or surface rupture is visible at the uphill limit of the lobate forms and suggest that these features may have been buried below the

younger Bu and Cyu Hesperian units. The actual contact, as visible in HiRISE imagery (Figure 12a), is at best indeterminate, with the lobate forms appearing at the base of a cliff at the Bu unit contact with the lobate complex. This cliff form represents the over-steepened edge of the Bu unit, with an average slope ranging from 20 to 25° above the lobate features (Figure 12b).

1.7 Discussion/Synthesis

Rock glaciers are lobate-shaped landforms of unconsolidated sediment and rock debris, with interstitial ice and ice lenses that move downslope by creep [37,75]. Based on a cross sectional and long profile form, with higher slopes at their heads and lower slopes at their distal edge [52,64,73], and as previously suggested by Anderson and Bell [42] and Le Deit et al. [37], the well-defined and uniform width lobate forms found on the north side of Mount Sharp correspond to terrestrial rock glacier morphology [38,80,87,105–107]. However, they do not exhibit characteristics, such as sublimation pits or "brain-terrain" (Figure 2a) [71,108], that are typically associated with relict rock glaciers found elsewhere on Mars. Further, the observed concave up-cross-sections (Figure 7b) do not suggest a deflated surface due to ice loss.

Besides a few possible equatorial locations [4], it is currently thought that low/ equatorial latitudes cannot support stable water ice today. Therefore, it is highly unlikely that these lobate forms currently retain water ice. Based on likely sourcing from the aeolian units capping Mount Sharp [50,52], the unstratified lobate forms likely contained ice/rock mixtures with a higher percentage of fine-grained material than a typical rock glacier on Earth under the same thermal conditions. As such, movement of entrained rock and ice was likely less viscous than the typical ice/rock mixture range (35/65 to 50/50) that typifies terrestrial rock glaciers. The lack of both sublimation features and a concave depressed central region, such as that found in terrestrial rock

glaciers, also suggests that these forms may have had their genesis in original features that contained a much higher percentage of rock and aeolian-derived fine-grained sediment. This difference may also explain why these forms, with an average length of ~6 km, are significantly longer than terrestrial rock glaciers that range from 100 s of meters to several kilometers in length [75].

The lack of wrinkle ridges similar to those found on terrestrial rock glaciers are likely the result of aeolian reworking similar to that found on the yardang units found to the east of these lobate deposits [104]. The lobate forms also exhibit a small number of craters relative to the surrounding non-lobate surfaces that they overly. While possible, one scenario for the existence of young uncratered surfaces relative to the cratered surfaces that they overly is that they are indistinguishable in age from the relatively uncratered Bu and Cp units. However, like the absence of wrinkle ridges, this cratering difference may once again be due to aeolian reworking that removed traces of small craters on the lobate forms.

If water or water ice were present during the emplacement of the lobate features, then subsequent cementation during lithification would suggest that they are composed of erosion-resistant sediments. Lobate cementation is supported by an observed high thermal emissivity for these units that is similar to that found on debris-covered glaciers elsewhere on Mars [109]. Later burial by less resistant and poorly lithified aeolian deposits would have preserved the original forms. The sharp appearance of the lobate forms is, therefore, likely the result of subsequent differential weathering of a poorly consolidated/lithified overlying unit, as well as interlobate material, a process similar to erosion observed during aeolian-dominated scarp retreat [62]. Other possible, but low-probability, scenarios include that these forms were formed by mudflows

or other viscous flow processes. These were not evaluated in this study but remain a possible explanation for these features.

The lobate complex drapes the northern slopes of Mount Sharp [37], with surface slopes of individual lobate forms between 11 and 23◦. Anderson and Bell [42] and Le Deit et al. [37] suggest that these low-angled lobate forms emerge from beneath the aeolian-sourced benched (Bu) and caprock units (Cp) on Mount Sharp. However, due to the covered nature of the contact [37,38], interpretation of stratigraphic order is, at best, uncertain. As Le Deit et al. [37] note, " . . . it is not trivial to determine the absolute ages of the possible periglacial landforms. They appear to modify the landscape and could have formed much later than the surfaces that they modify". Detailed analysis of HiRISE imagery reveals a 300–400 m high angled scarp at the upper limit of the lobate forms, from which these features emanate, suggesting that mass wasting of the Bu and Cp units may have played a role in the formation of the lobate forms, possibly calling an interpretation of formation prior to the Bu and Cp units into question.

Flow rates coupled to lobate form lengths for the three most well-preserved lobes (1–3) provide a rough estimate of formation times. At the coldest temperature modeled (−50 ◦C), average formation times are in excess of 2.4 Ma and 1.4 Ma for the 35/65 and 50/50 rock/ice mixtures, respectively. This timing would require the addition of rock and/or fine-grained debris to the head of the rock glacier form during a persistent cold climate with extremely slow weathering. At the warmest modeled temperature (0 ◦C), mean formation times range from 700 years for a 50/50 rock/ice mixture to ~2.2 Ka years for the 35/65 mixture. These ages are similar to surface flow rates and formation times associated with large rock glaciers on Earth, which range between a few thousand to several tens of thousands of years [110–112]. However, warm

(0 ◦C) temperatures have only been observed on the surface of Mars during peak insolation conditions [39].

Le Deit et al. [37] postulated that melting snow, a possible source of water ice for rock glacier formation, might have been enhanced due to higher insolation on Mount Sharp's northern slopes relative to its southern ones. The high elevation of Mount Sharp may have also played a role in the formation of conditions amenable to perennial periglacial conditions on Mt Sharp's northern slopes through most of its history. These periglacial conditions may have been enhanced by variations in obliquity, which, at its extreme, would have transferred water from polar to equatorial regions [11,12,20,25,26,30–35,113].

Dickson et al. [9] and Fairén et al. [38] suggest that the last occurrence of ice near the equator could have occurred during the late Amazonian Epoch, though, Fairén et al. [38] suggested that the latest obliquity-driven ice migration might not have been responsible for the observed evidence of glacial and periglacial activity interpreted in Gale crater. Studies of obliquity/temperature relationships are inconclusive and often contradictory, with some [114] suggesting that during periods of high obliquity, Mars' low latitudes/equatorial regions would see a decrease in average annual temperatures (<−50 ◦C). Alternatively, some recent studies [41] suggest that this is not the case and that temperatures could increase during periods of high obliquity.

Ground water seepage during warmer periods may have injected water ice directly into the sediments, allowing them to flow, potentially at close to modern pressures. However, it is unlikely that modern (20 Ma to present) temperatures would be able to support the warmest temperatures used in our calculations. This suggests that these lobate forms were formed much earlier (>>20 Ma) in Martian history, when increased global atmospheric pressure and

temperatures [115], coupled with liquid water, would further support the periglacial processes discussed in this study.

1.8 Conclusions

The presence of periglacial features on Mount Sharp in the form of rock glaciers and a spatulate lobe emanating from the upper elevation of Mount Sharp indicates a past equatorial climate that had water available for the production of ice bodies. The presence of these features on Mount Sharp, in combination with other glacial features in highland drainage source areas of the Peace Vallis drainage, north of Gale crater and glacial forms within Gale crater, including possible roche moutonnée and eskers, marks a possible former extensive glacial modification of the equatorial region.

The presence of possible cold-based rock glaciers on the north face of Mount Sharp at equatorial latitudes has significant implications for understanding the past global redistribution of the water ice cryosphere, due to obliquity-driven insolation variability. Periglacial conditions may have been enhanced by variations in obliquity, which, at its extreme, would have transferred water from polar to equatorial regions.

As well, the possible presence of ice within Gale crater and its surrounding environment has profound implications for understanding Martian climate and landscape evolution. Further study is necessary to investigate these possible glacial forms, by obtaining higher resolution data sets, such as digital elevation models of Gale crater and its surrounding area. Further, by conducting extensive crater counting of the different glacial/periglacial forms, we can then better understand the relative timing of these processes and possibly the role of aeolian erosion in modifying these features. Finally, the various glacier/periglacial forms found in Gale crater and

surrounding areas are most likely not directly linked temporally; rather, they likely represent a spectrum of different obliquity-driven ice migrations.

1.9 Contributions

Conceptualization, J.M.W. and L.A.S.; methodology, J.M.W. and L.A.S.; software, J.M.W.; formal analysis, J.M.W., L.A.S., H.E.N.; investigation, J.M.W., L.A.S., H.E.N.; resources, L.A.S.; data curation, J.M.W.; writing—original draft preparation, J.M.W. and L.A.S.; writing—review and editing, J.M.W., L.A.S., H.E.N.; visualization, J.M.W., L.A.S.; supervision, L.A.S.; project administration, L.A.S.; funding acquisition, L.A.S. All authors have read and agreed to the published version of the manuscript.

REFERENCES

1. Clifford, S.M. A model for the hydrologic and climatic behavior of water on Mars. *J. Geophys. Res. Planets* **1993**, *98*, 10973–11016. [CrossRef]
2. Mège, D.; Bourgeois, O. Equatorial glaciations on Mars revealed by gravitational collapse of Valles Marineris wallslopes. *Earth Planet. Sci. Lett.* **2011**, *310*, 182–191. [CrossRef]
3. Wordsworth, R.D. The climate of early Mars. *Annu. Rev. Earth Planet. Sci.* **2016**, *44*, 381–408. [CrossRef]
4. Mitrofanov, I.; Malakhov, A.; Djachkova, M.; Golovin, D.; Litvak, M.; Mokrousov, M.; Sanin, A.; Svedhem, H.; Zelenyi, L. The evidence for unusually high hydrogen abundances in the central part of Valles Marineris on Mars. *Icarus* **2022**, *374*, 114805. [CrossRef]
5. Forget, F. Mars CO 2 Ice Polar Caps. In *Solar System Ices*; Springer: New York, NY, USA, 1998; pp. 477–507.
6. Parry Rubincam, D. Mars secular obliquity change due to water ice caps. *J. Geophys. Res. Planets* **1999**, *104*, 30765–30771. [CrossRef]
7. Baker, D.M.; Head, J.W.; Marchant, D.R. Flow patterns of lobate debris aprons and lineated valley fill north of Ismeniae Fossae, Mars: Evidence for extensive mid-latitude glaciation in the Late Amazonian. *Icarus* **2010**, *207*, 186–209. [CrossRef]
8. Brough, S.; Hubbard, B.; Hubbard, A. Area and volume of mid-latitude glacier-like forms on Mars. *Earth Planet. Sci. Lett.* **2019**, *507*, 10–20. [CrossRef]
9. Dickson, J.L.; Head, J.W.; Marchant, D.R. Late Amazonian glaciation at the dichotomy boundary on Mars: Evidence for glacial thickness maxima and multiple glacial phases. *Geology* **2008**, *36*, 411–414. [CrossRef]

10. Head, J.; Neukum, G.; Jaumann, R.; Hiesinger, H.; Hauber, E.; Carr, M.; Masson, P.; Foing, B.; Hoffmann, H.; Kreslavsky, M. Tropical to mid-latitude snow and ice accumulation, flow and glaciation on Mars. *Nature* **2005**, *434*, 346–351. [CrossRef]
11. Head, J.W.; Marchant, D.; Agnew, M.; Fassett, C.; Kreslavsky, M. Extensive valley glacier deposits in the northern mid-latitudes of Mars: Evidence for Late Amazonian obliquity-driven climate change. *Earth Planet. Sci. Lett.* **2006**, *241*, 663–671. [CrossRef]
12. Head, J.W.; Marchant, D.R.; Dickson, J.L.; Kress, A.M.; Baker, D.M. Northern mid-latitude glaciation in the Late Amazonian period of Mars: Criteria for the recognition of debris-covered glacier and valley glacier landsystem deposits. *Earth Planet. Sci. Lett.* **2010**, *294*, 306–320. [CrossRef]
13. Hubbard, B.; Milliken, R.E.; Kargel, J.S.; Limaye, A.; Souness, C. Geomorphological characterisation and interpretation of a mid-latitude glacier-like form: Hellas Planitia, Mars. *Icarus* **2011**, *211*, 330–346. [CrossRef]
14. Hubbard, B.; Souness, C.; Brough, S. Glacier-like forms on Mars. *Cryosphere* **2014**, *8*, 2047–2061. [CrossRef]
15. Levy, J.S.; Head, J.W.; Marchant, D.R. Lineated valley fill and lobate debris apron stratigraphy in Nilosyrtis Mensae, Mars: Evidence for phases of glacial modification of the dichotomy boundary. *J. Geophys. Res. Planets* **2007**, *112*. [CrossRef]
16. Scanlon, K.; Head, J.; Marchant, D. Remnant Buried Ice in the Arsia Mons Fan-Shaped Deposit, Mars. In Proceedings of the Lunar and Planetary Science Conference, The Woodlands, TX, USA, 16–20 March 2015.

17. Shean, D.E.; Head, J.W., III; Fastook, J.L.; Marchant, D.R. Recent glaciation at high elevations on Arsia Mons, Mars: Implications for the formation and evolution of large tropical mountain glaciers. *J. Geophys. Res. Planets* **2007**, *112*. [CrossRef]

18. Gourronc, M.; Bourgeois, O.; Mège, D.; Pochat, S.; Bultel, B.; Massé, M.; le Deit, L.; le Mouélic, S.; Mercier, D. One million cubic kilometers of fossil ice in Valles Marineris: Relicts of a 3.5 Gy old glacial landsystem along the Martian equator. *Geomorphology* **2014**, *204*, 235–255. [CrossRef]

19. Brough, S.; Hubbard, B.; Hubbard, A. Former extent of glacier-like forms on Mars. *Icarus* **2016**, *274*, 37–49. [CrossRef]

20. Forget, F.; Haberle, R.; Montmessin, F.; Levrard, B.; Head, J. Formation of glaciers on Mars by atmospheric precipitation at high obliquity. *Science* **2006**, *311*, 368–371. [CrossRef]

21. Mellon, M.T.; Feldman, W.C.; Prettyman, T.H. The presence and stability of ground ice in the southern hemisphere of Mars. *Icarus* **2004**, *169*, 324–340. [CrossRef]

22. Mellon, M.T.; Jakosky, B.M. The distribution and behavior of Martian ground ice during past and present epochs. *J. Geophys. Res. Planets* **1995**, *100*, 11781–11799. [CrossRef]

23. Ward, W.R. Large-scale variations in the obliquity of Mars. *Science* **1973**, *181*, 260–262. [CrossRef] [PubMed]

24. Brunetti, M.T.; Guzzetti, F.; Cardinali, M.; Fiorucci, F.; Santangelo, M.; Mancinelli, P.; Komatsu, G.; Borselli, L. Analysis of a new geomorphological inventory of landslides in Valles Marineris, Mars. *Earth Planet. Sci. Lett.* **2014**, *405*, 156–168. [CrossRef]

25. Abe, Y.; Numaguti, A.; Komatsu, G.; Kobayashi, Y. Four climate regimes on a land planet with wet surface: Effects of obliquity change and implications for ancient Mars. *Icarus* **2005**, *178*, 27–39. [CrossRef]

26. Bills, B.; Keane, J. Mars Obliquity Variations are Both Non-Chaotic and Probably Fully Damped. In Proceedings of the 50th Annual Lunar and Planetary Science Conference, The Woodlands, TX, USA, 18–22 March 2019.
27. Fastook, J.L.; Head, J.W.; Marchant, D.R.; Forget, F. Tropical mountain glaciers on Mars: Altitude-dependence of ice accumulation, accumulation conditions, formation times, glacier dynamics, and implications for planetary spin-axis/orbital history. *Icarus* **2008**, *198*, 305–317. [CrossRef]
28. Head, J.W.; Marchant, D.R. Cold-based mountain glaciers on Mars: Western Arsia Mons. *Geology* **2003**, *31*, 641–644. [CrossRef]
29. Head, J.W.; Nahm, A.L.; Marchant, D.R.; Neukum, G. Modification of the dichotomy boundary on Mars by Amazonian
mid-latitude regional glaciation. *Geophys. Res. Lett.* **2006**, *33*. [CrossRef]
30. Laskar, J.; Correia, A.; Gastineau, M.; Joutel, F.; Levrard, B.; Robutel, P. Long term evolution and chaotic diffusion of the insolation quantities of Mars. *Icarus* **2004**, *170*, 343–364. [CrossRef]
31. Toigo, A.D.; Waugh, D.W.; Guzewich, S.D. Atmospheric transport into polar regions on Mars in different orbital epochs. *Icarus* **2020**, *347*, 113816. [CrossRef]
32. Vos, E.; Aharonson, O.; Schorghofer, N. Dynamic and isotopic evolution of ice reservoirs on Mars. *Icarus* **2019**, *324*, 1–7. [CrossRef]
33. Vos, E.; Aharonson, O.; Schorghofer, N.; Forget, F.; Millour, E. Milankovitch-driven redistribution and fractionation of ice deposits on Mars. In Proceedings of the 50th EPSC-DPS Joint Meeting 2019, Geneva, Switzerland, 15–20 September 2019.

34. Weiss, D.K. Mars in ice ages for~25% of post-Noachian geologic history. *Earth Planet. Sci. Lett.* **2019**, *528*, 115847. [CrossRef]

35. Williams, J.P.; van der Bogert, C.H.; Pathare, A.V.; Michael, G.G.; Kirchoff, M.R.; Hiesinger, H. Dating very young planetary surfaces from crater statistics: A review of issues and challenges. *Meteorit. Planet. Sci.* **2018**, *53*, 554–582. [CrossRef]

36. Williams, J.; Scuderi, L.A.; Newsom, H.E. Constraining Possible Glacial Reworking of Ancient Fluvial Channels on the Dichotomy Boundary at Equatorial Regions, Mars. In Proceedings of the AGU Fall Meeting Abstracts, 2020; Available online: https://ui.adsabs.harvard.edu/abs/2020AGUFMP038...02W/abstract (accessed on 28 February 2022).

37. Deit, L.L.; Hauber, E.; Fueten, F.; Pondrelli, M.; Rossi, A.P.; Jaumann, R. Sequence of infilling events in Gale Crater, Mars: Results from morphology, stratigraphy, and mineralogy. *J. Geophys. Res. Planets* **2013**, *118*, 2439–2473. [CrossRef]

38. Fairén, A.G.; Stokes, C.R.; Davies, N.S.; Schulze-Makuch, D.; Rodríguez, J.A.P.; Davila, A.F.; Uceda, E.R.; Dohm, J.M.; Baker, V.R.; Clifford, S.M. A cold hydrological system in Gale crater, Mars. *Planet. Space Sci.* **2014**, *93*, 101–118. [CrossRef]

39. Schorghofer, N. Temperature response of Mars to Milankovitch cycles. *Geophys. Res. Lett.* **2008**, *35*. [CrossRef]

40. Ward, W.R. Climatic variations on Mars: 1. *Astronomical theory of insolation. J. Geophys. Res.* **1974**, *79*, 3375–3386. [CrossRef]

41. Madeleine, J.B.; Head, J.W.; Forget, F.; Navarro, T.; Millour, E.; Spiga, A.; Colaïtis, A.; Määttänen, A.; Montmessin, F.; Dickson, J.L. Recent ice ages on Mars: The role of radiatively active clouds and cloud microphysics. *Geophys. Res. Lett.* **2014**, *41*, 4873–4879. [CrossRef]

42. Anderson, R.B.; Bell, J.F., III. Geologic mapping and characterization of Gale Crater and implications for its potential as a Mars Science Laboratory landing site. *Mars J.* **2010**, *5*, 76–128. [CrossRef]

43. Le Deit, L.; Hauber, E.; Fueten, F.; Pondrelli, M.; Rossi, A.; Mangold, N.; Jaumann, R. Geological study of Gale Crater on Mars. In Proceedings of the AGU Fall Meeting Abstracts, San Francisco, CA, USA, 5–9 December 2011.

44. Gallegos, Z.; Newsom, H.; Scuderi, L.; Gasnault, O.; le Mouélic, S.; Wiens, R.; Maurice, S. New Insights into the Extensive Inverted Features Within Gale Crater, Mars. In Proceedings of the Lunar and Planetary Science Conference, Woodlands, TX, USA, 16–20 March 2020.

45. Newsom, H.; Scuderi, L.; Gallegos, Z.; Williams, J.; Dimitracopoulos, G.; Tornabene, L.; Wiens, R.; Gasnault, O. Evidence for Glacial and Fluvial Processes on Gale Crater Rim–Dulce Vallis. In Proceedings of the Lunar and Planetary Science Conference, Woodlands, TX, USA, 15–19 March 2021.

46. Oehler, D.Z.; Mangold, N.; Hallet, B.; Fairén, A.G.; le Deit, L.; Williams, A.J.; Sletten, R.S.; Martínez-Frías, J. Origin and significance of decameter-scale polygons in the lower Peace Vallis fan of Gale crater, Mars. *Icarus* **2016**, *277*, 56–72. [CrossRef]

47. Stack, K.M.; Grotzinger, J.P.; Lamb, M.P.; Gupta, S.; Rubin, D.M.; Kah, L.C.; Edgar, L.A.; Fey, D.M.; Hurowitz, J.A.; McBride, M. Evidence for plunging river plume deposits in the Pahrump Hills member of the Murray formation, Gale crater, Mars. *Sedimentology* **2019**, *66*, 1768–1802. [CrossRef]

48. Thomson, B.; Bridges, N.; Milliken, R.; Baldridge, A.; Hook, S.; Crowley, J.; Marion, G.; Filho, C.d.; Brown, A.; Weitz, C. Constraints on the origin and evolution of the layered mound in Gale Crater, Mars using Mars Reconnaissance Orbiter data. *Icarus* **2011**, *214*,

413–432. [CrossRef]

49. Day, M.; Anderson, W.; Kocurek, G.; Mohrig, D. Carving intracrater layered deposits with wind on Mars. *Geophys. Res. Lett.* **2016**, *43*, 2473–2479. [CrossRef]

50. Grotzinger, J.P.; Gupta, S.; Malin, M.C.; Rubin, D.M.; Schieber, J.; Siebach, K.; Sumner, D.Y.; Stack, K.M.; Vasavada, A.R.; Arvidson, R.E. Deposition, exhumation, and paleoclimate of an ancient lake deposit, Gale crater, Mars. *Science* **2015**, *350*, aac7575. [CrossRef] [PubMed]

51. Malin, M.C.; Edgett, K.S. Sedimentary rocks of early Mars. *Science* **2000**, *290*, 1927–1937. [CrossRef]

52. Anderson, R.B.; Edgar, L.A.; Rubin, D.M.; Lewis, K.W.; Newman, C. Complex bedding geometry in the upper portion of Aeolis Mons, Gale crater, Mars. *Icarus* **2018**, *314*, 246–264. [CrossRef]

53. Banham, S.G.; Gupta, S.; Rubin, D.M.; Watkins, J.A.; Sumner, D.Y.; Edgett, K.S.; Grotzinger, J.P.; Lewis, K.W.; Edgar, L.A.; Stack-Morgan, K.M. Ancient Martian aeolian processes and palaeomorphology reconstructed from the Stimson formation on the lower slope of Aeolis Mons, Gale crater, Mars. *Sedimentology* **2018**, *65*, 993–1042. [CrossRef]

54. Rapin, W.; Dromart, G.; Rubin, D.; Deit, L.L.; Mangold, N.; Edgar, L.A.; Gasnault, O.; Herkenhoff, K.; le Mouélic, S.; Anderson, R. Alternating wet and dry depositional environments recorded in the stratigraphy of Mount Sharp at Gale crater, Mars. *Geology* **2021**, *49*, 842–846. [CrossRef]

55. Bridges, N.; Calef, F.; Hallet, B.; Herkenhoff, K.E.; Lanza, N.; le Mouélic, S.; Newman, C.; Blaney, D.; de Pablo, M.; Kocurek, G. The rock abrasion record at Gale crater: Mars Science Laboratory results from Bradbury landing to Rocknest. *J. Geophys. Res. Planets* **2014**, *119*, 1374–1389. [CrossRef]

56. Bridges, N.; Greeley, R.; Haldemann, A.; Herkenhoff, K.E.; Kraft, M.; Parker, T.; Ward, A. Ventifacts at the Pathfinder landing site. *J. Geophys. Res. Planets* **1999**, *104*, 8595–8615. [CrossRef]

57. Hobbs, S.W.; Paull, D.J.; Bourke, M.C. Aeolian processes and dune morphology in Gale Crater. *Icarus* **2010**, *210*, 102–115. [CrossRef]

58. Knight, J. The environmental significance of ventifacts: A critical review. *Earth-Sci. Rev.* **2008**, *86*, 89–105. [CrossRef]

59. Laity, J.E.; Bridges, N.T. Ventifacts on Earth and Mars: Analytical, field, and laboratory studies supporting sand abrasion and windward feature development. *Geomorphology* **2009**, *105*, 202–217. [CrossRef]

60. Sharp, R.P. Mars: Fretted and chaotic terrains. *J. Geophys. Res.* **1973**, *78*, 4073–4083. [CrossRef]

61. Ward, A.W. Yardangs on Mars: Evidence of recent wind erosion. *J. Geophys. Res. Solid Earth* **1979**, *84*, 8147–8166. [CrossRef] 62. Williams, J.; Day, M.; Chojnacki, M.; Rice, M. Scarp orientation in regions of active aeolian erosion on Mars. *Icarus* **2020**, *335*, 113384. [CrossRef]

63. Piqueux, S.; Buz, J.; Edwards, C.S.; Bandfield, J.L.; Kleinböhl, A.; Kass, D.M.; Hayne, P.O.; S, M.C.; Teams, T. Widespread shallow water ice on Mars at high latitudesand midlatitudes. *Geophys. Res. Lett.* **2019**, *46*, 14290–14298. [CrossRef]

64. Jones, D.B.; Harrison, S.; Anderson, K.; Whalley, W.B. Rock glaciers and mountain hydrology: A review. *Earth-Sci. Rev.* **2019**, *193*, 66–90. [CrossRef]

65. Holt, J.W.; Safaeinili, A.; Plaut, J.J.; Head, J.W.; Phillips, R.J.; Seu, R.; Kempf, S.D.; Choudhary, P.; Young, D.A.; Putzig, N.E. Radar sounding evidence for buried glaciers in the southern mid-latitudes of Mars. *Science* **2008**, *322*, 1235–1238. [CrossRef]

66. Sinha, R.K.; Murty, S. Amazonian modification of Moreux crater: Record of recent and episodic glaciation in the Protonilus Mensae region of Mars. *Icarus* **2015**, *245*, 122–144. [CrossRef]

67. Fastook, J.L.; Head, J.W.; Marchant, D.R. Form. *Lobate Debris Aprons Mars: Assess. Reg. Ice Sheet Collapse Debris-Cover. Armoring.*

Icarus **2014**, *228*, 54–63.

68. Lucchitta, B.K. Ice Debris Frett. Terrain Mars. *J. Geophys. Res. Solid Earth* **1984**, *89*, B409–B418. [CrossRef]

69. Squyres, S.W. Martian Frett. Terrain: Flow Eros. *Debris. Icarus* **1978**, *34*, 600–613.

70. Van Gasselt, S.; Hauber, E.; Neukum, G. Lineated valley fill at the Martian dichotomy boundary: Nature and history of degradation. *J. Geophys. Res. Planets* **2010**, *115*. [CrossRef]

71. Irwin, R.P., III; Watters, T.R.; Howard, A.D.; Zimbelman, J.R. Sedimentary resurfacing and fretted terrain development along the crustal dichotomy boundary, Aeolis Mensae, Mars. *J. Geophys. Res. Planets* **2004**, *109*. [CrossRef]

72. Mangold, N. Geomorphic analysis of lobate debris aprons on Mars at Mars Orbiter Camera scale: Evidence for ice sublimation initiated by fractures. *J. Geophys. Res. Planets* **2003**, *108*. [CrossRef]

73. Pierce, T.L.; Crown, D.A. Morphologic and topographic analyses of debris aprons in the eastern Hellas region, Mars. *Icarus* **2003**, *163*, 46–65. [CrossRef]

74. Wahrhaftig, C.; Cox, A. Rock glaciers in the Alaska Range. *Geol. Soc. Am. Bull.* **1959**, *70*, 383–436. [CrossRef]

75. Elizabeth Martin, H.; Whalley, W.B. Rock glaciers: Part 1: Rock glacier morphology: Classification and distribution. *Prog. Phys. Geogr.* **1987**, *11*, 260–282. [CrossRef]

76. Giardino, J.R.; Shroder, J.F.; Vitek, J.D. *Rock Glaciers*; Allen & Unwin: Crow's Nest, Australia, 1987.

77. Mahaney, W.C.; Miyamoto, H.; Dohm, J.M.; Baker, V.R.; Cabrol, N.A.; Grin, E.A.; Berman, D.C. Rock glaciers on Mars: Earth-based clues to Mars' recent paleoclimatic history. *Planet. Space Sci.* **2007**, *55*, 181–192.

78. Easterbrook, D.J. *Surface Processes and Landforms*; Macmillan: New York, NY, USA, 1993.

79. Emmert, A.; Kneisel, C. Internal structure of two alpine rock glaciers investigated by quasi-3-D electrical resistivity imaging. *Cryosphere* **2017**, *11*, 841–855. [CrossRef]

80. Degenhardt, J.J., Jr.; Giardino, J.R. Subsurface investigation of a rock glacier using ground-penetrating radar: Implications for locating stored water on Mars. *J. Geophys. Res. Planets* **2003**, *108*. [CrossRef]

81. Whalley, W.B.; Azizi, F. Rock glaciers and protalus landforms: Analogous forms and ice sources on Earth and Mars. *J. Geophys. Res. Planets* **2003**, *108*. [CrossRef]

82. Humlum, O. Rock glaciers in northern Spitsbergen: A discussion. *J. Geol.* **1982**, *90*, 214–217. [CrossRef]

83. Azizi, F.; Whalley, W. Finite element analysis of the creep of debris containing thin ice bodies. In Proceedings of the Fifth International Offshore and Polar Engineering Conference, Hague, The Netherlands, 11–16 June 1995; OnePetro: Richardson, TX, USA, 1995.

84. Azizi, F.; Whalley, W. Numerical modelling of the creep behaviour of ice-debris mixtures under variable thermal regimes. In Proceedings of the Sixth International Offshore and Polar Engineering Conference, Los Angeles, CA, USA, 26–31 May 1996; OnePetro: Richardson, TX, USA, 1996.

85. Xue, K.; Wen, Z.; Zhu, Z.; Wang, D.; Luo, F.; Zhang, M. An experimental study of the relationship between the matric potential, unfrozen water, and segregated ice of saturated freezing soil. *Bull. Eng. Geol. Environ.* **2021**, *80*, 2535–2544. [CrossRef]

86. Whalley, W.B.; Krinsley, D.H. A scanning electron microscope study of surface textures of quartz grains from glacial environments. *Sedimentology* **1974**, *21*, 87–105. [CrossRef]

87. Whalley, W.B.; Martin, H.E. Rock glaciers: II models and mechanisms. *Prog. Phys. Geogr.* **1992**, *16*, 127–186. [CrossRef]

88. Kaab, A. Rock glaciers and protalus forms. *En-Cyclopedia Quat. Sci.* **2007**, 2236–2242. Available online: https://ci.nii.ac.jp/naid/ 20001586454/ (accessed on 28 February 2022).

89. Hamilton, S.J.; Whalley, W.B. Rock glacier nomenclature: A re-assessment. *Geomorphology* **1995**, *14*, 73–80. [CrossRef]

90. Halla, C.; Blöthe, J.H.; Baldis, C.T.; Liaudat, D.T.; Hilbich, C.; Hauck, C.; Schrott, L. Ice content and interannual water storage changes of an active rock glacier in the dry Andes of Argentina. *Cryosphere* **2021**, *15*, 1187–1213. [CrossRef]

91. Berthling, I. Beyond confusion: Rock glaciers as cryo-conditioned landforms. *Geomorphology* **2011**, *131*, 98–106. [CrossRef] 92. Francou, B.; Fabre, D.; Pouyaud, B.; Jomelli, V.; Arnaud, Y. Symptoms of degradation in a tropical rock glacier, Bolivian Andes. *Permafr. Periglac. Process.* **1999**, *10*, 91–100. [CrossRef]

93. Johnson, G.; Chang, H.; Fountain, A. Active rock glaciers of the contiguous United States: Geographic information system inventory and spatial distribution patterns. *Earth Syst. Sci. Data* **2021**, *13*, 3979–3994. [CrossRef]

94. Koutnik, M.R.; Pathare, A.V. Contextualizing lobate debris aprons and glacier-like forms on Mars with debris-covered glaciers on Earth. *Prog. Phys. Geogr. Earth Environ.* **2021**, *45*, 130–186. [CrossRef]

95. Konrad, S.; Humphrey, N.; Steig, E.; Clark, D.; Potter, N., Jr.; Pfeffer, W. Rock glacier dynamics and paleoclimatic implications. *Geology* **1999**, *27*, 1131–1134. [CrossRef]

96. Whalley, W.B.; Azizi, F. Rheological models of active rock glaciers: Evaluation, critique and a possible test. *Permafr. Periglac. Process.* **1994**, *5*, 37–51. [CrossRef]

97. Sergienko, O.; Creyts, T.T.; Hindmarsh, R. Similarity of organized patterns in driving and basal stresses of Antarctic and Greenland ice sheets beneath extensive areas of basal sliding. *Geophys. Res. Lett.* **2014**, *41*, 3925–3932. [CrossRef]

98. Azuma, N. A flow law for anisotropic ice and its application to ice sheets. *Earth Planet. Sci. Lett.* **1994**, *128*, 601–614. [CrossRef]

99. Cuffey, K.M.; Paterson, W.S.B. *The Physics of Glaciers*; Academic Press: Cambridge, MS, USA, 2010.

100. Goldsby, D.; Kohlstedt, D.L. Superplastic deformation of ice: Experimental observations. *J. Geophys. Res. Solid Earth* **2001**, *106*, 11017–11030. [CrossRef]

101. Colaprete, A.; Jakosky, B.M. Ice flow and rock glaciers on Mars. *J. Geophys. Res. Planets* **1998**, *103*, 5897–5909. [CrossRef] 102. Durham, W.; Stern, L. Rheological properties of water ice—Applications to satellites of the outer planets. *Annu. Rev. Earth Planet. Sci.* **2001**, *29*, 295–330. [CrossRef]

103. McEwen, A.S.; Eliason, E.M.; Bergstrom, J.W.; Bridges, N.T.; Hansen, C.J.; Delamere, W.A.; Grant, J.A.; Gulick, V.C.; Herkenhoff, K.E.; Keszthelyi, L. Mars reconnaissance orbiter's high

resolution imaging science experiment (HiRISE). *J. Geophys. Res. Planets* **2007**, *112*. [CrossRef]

104. Malin, M.C.; Bell, J.F., III; Cantor, B.A.; Caplinger, M.A.; Calvin, W.M.; Clancy, R.T.; Edgett, K.S.; Edwards, L.; Haberle, R.M.; James, P.B. Context camera investigation on board the Mars Reconnaissance Orbiter. *J. Geophys. Res. Planets* **2007**, *112*. [CrossRef] 105. Dromart, G.; Le Deit, L.; Rapin, W.; Gasnault, O.; le Mouélic, S.; Quantin-Nataf, C.; Mangold, N.; Rubin, D.; Lasue, J.; Maurice, S. Deposition and erosion of a Light-Toned Yardang-forming unit of Mt Sharp, Gale crater, Mars. *Earth Planet. Sci. Lett.* **2021**, *554*, 116681. [CrossRef]

106. Kenner, R.; Phillips, M.; Beutel, J.; Hiller, M.; Limpach, P.; Pointner, E.; Volken, M. Factors controlling velocity variations at short-term, seasonal and multiyear time scales, Ritigraben rock glacier, Western Swiss Alps. *Permafr. Periglac. Process.* **2017**, *28*, 675–684. [CrossRef]

107. Whalley, W.B.; Hamilton, S.J.; Palmer, C.F.; Gordon, J.E.; Martin, H.E. The dynamics of rock glaciers: Data from Tröllaskagi, north Iceland. In *Steepland Geomorphology*; ResearchGate: Berlin, Germany, 1995; pp. 129–145.

108. Levy, J.S.; Head, J.W.; Marchant, D.R. Concentric crater fill in Utopia Planitia: History and interaction between glacial "brain terrain" and periglacial mantle processes. *Icarus* **2009**, *202*, 462–476. [CrossRef]

109. Fraeman, A.; Ehlmann, B.; Arvidson, R.; Edwards, C.; Grotzinger, J.; Milliken, R.; Quinn, D.; Rice, M. The stratigraphy and evolution of lower Mount Sharp from spectral, morphological, and thermophysical orbital data sets. *J. Geophys. Res. Planets* **2016**, *121*, 1713–1736. [CrossRef]

110. Frauenfelder, R.; Laustela, M.; Kääb, A. Relative age dating of Alpine rockglacier surfaces. *Z. Geomorphol.* **2005**, *49*, 145–166.

111. Haeberli, W.; Brandova, D.; Burga, C.; Egli, M.; Frauenfelder, R.; Kääb, A.; Maisch, M.; Mauz, B.; Dikau, R. Methods for absolute and relative age dating of rock-glacier surfaces in alpine permafrost. In Proceedings of the 8th International Conference on Permafrostm, Zurich, Switzerland, 21–25 July 2003.

112. Krainer, K.; Bressan, D.; Dietre, B.; Haas, J.N.; Hajdas, I.; Lang, K.; Mair, V.; Nickus, U.; Reidl, D.; Thies, H. A 10,300-year-old permafrost core from the active rock glacier Lazaun, southern Ötztal Alps (South Tyrol, northern Italy). *Quat. Res.* **2015**, *83*, 324–335. [CrossRef]

113. Fassett, C.I.; Levy, J.S.; Dickson, J.L.; Head, J.W. An extended period of episodic northern mid-latitude glaciation on Mars during the Middle to Late Amazonian: Implications for long-term obliquity history. *Geology* **2014**, *42*, 763–766. [CrossRef]

114. Hauber, E.; Ulrich, M.; Preusker, F.; Trauthan, F.; Reiss, D.; Hiesinger, H.; Zanetti, M.; Team, S. Svalbard (Norway) as a terrestrial analogue for Martian landforms: Results on alluvial fans. *EPSC Abstr.* **2009**, *4*, EPSC2009-772.

115. Carr, M.H. Retention of an atmosphere on early Mars. *J. Geophys. Res. Planets* **1999**, *104*, 21897–21909. [CrossRef]

CHAPTER TWO

Comparative planetology – Comparing cirques on Mars and Earth using a CNN

Citation:

Williams, J. M., Scuderi, L. A., McClanahan, T. P., Banks, M. E., & Baker, D. M. (2023). Comparative planetology–Comparing cirques on Mars and Earth using a CNN. *Geomorphology*, 440, 108881. doi.org/10.1016/j.geomorph.2023.108881

Abstract

New approaches for comparative planetology are vital to recognize and assess possible shared formative processes that shape landforms on different planetary bodies, and in the case of this study to identify possible cirques preserved from past martian climates that may have been more favorable to equatorial ice. We used "RetinaNet", an augmented Convolutional Neural Network (CNN) initially trained with digital elevation data from over 1950 terrestrial cirques, to identify similar forms along a 50x50km area of the equatorial martian Dichotomy Boundary east of Gale Crater. A significant number of false positive detections associated with CTX stereo pair derived DEM artifacts and tile edges as well as craters were automatically removed. High confidence levels assigned by the machine learning algorithm suggest that the 16-remaining cirque-like forms may have formed and evolved under similar conditions to their terrestrial analogs. Morphometric data extracted for each of these cirque-like forms was statistically compared to terrestrial analog morphometric measures. While cirque length and width were significantly larger than their terrestrial counterparts and the area of these forms was ~150 % larger, on average headwall heights were ~25 % shorter. Allometric relationships suggest that the shape of these martian features changes proportionally as they grow in contrast to terrestrial forms where length increases faster than width and height. This could be due to the weaker gravitational force on Mars (3.721 m/s2) and other effects related to martian climate and

environmental conditions, such as cold based glaciation. The identification of cirques in an equatorial region has implications for cryosphere distribution/redistribution and martian geologic and climatic history.

2.1 Introduction

Comparative planetology addresses fundamental driving and con- trolling forces that both create and modify landforms on different planetary bodies. Since in situ examination of surface processes has principally been conducted on Earth, surface processes on other planetary bodies are typically compared to terrestrial analogs (Glassmeier, 2020). However, terrestrial geomorphic systems may represent only one possible expression of planetary surface processes. Evaluating surface formative expressions in a terrestrial context can lead to observational bias, and possibly incorrect conclusions about the underlying processes. Therefore, it is important to analyze landform expressions on other planetary bodies by first comparing them to well understood forms from observable terrestrial processes.

Glacial and periglacial processes resulting from the presence of water ice are major geomorphic agents capable of significant modification of planetary surfaces (Palacios et al., 2021). Of the four terrestrial planets, Earth and Mars are the most similar in that they have substantial water ice quantities on surfaces and near sub surfaces. Melosh (2011) suggested that Mars, and possibly some outer solar system moons, are the only other planetary bodies in our solar system that support water ice glacial processes.

Mars currently has a hyper-arid cold surface with a thin atmosphere. This has been the case for most of the Amazonian period (3.0 Ga to present) with aeolian processes currently the dominant geomorphic agent. Evidence of contemporary water ice on Mars and past expressions

of glacial and periglacial landforms are typically found at mid- to high- latitudes (Banks et al., 2008; Conway et al., 2018; Hepburn et al., 2019; Morgan et al., 2021) with most of the mid- to high-latitude glacial forms thought to be dormant or relic (Head et al., 2006; Dickson et al., 2008; Scanlon et al., 2015). Studies have documented relic cirque-like alcoves at higher elevations on Arsia Mons and Olympus Mons, and others suggest that extant water ice can be seen in the southern Elysium region near the martian equator (Murray et al., 2005; Shean et al., 2007; Scanlon et al., 2015). Furthermore, there is growing evidence supporting relic glacial forms at lower latitudes closer to the equator on Mars (Head et al., 2006; Davila et al., 2013; Williams et al., 2022). Some of these studies suggest a formation age for relic equatorial glaciers at the Hesperian/Amazonian boundary (2.9–3.0 Ga) (Davila et al., 2013). However, the timing of these glacial/periglacial processes at lower latitudes is poorly understood.

To evaluate the possibility of a glacial past in the martian equatorial region, it is important to compare possible martian glacial forms to terrestrial analogs. Specifically, this study aims to analyze possible cirque forms in the equatorial region of Mars to test the hypothesis that they are analogous to terrestrial cirques and therefore could have formed under similar conditions. Due to their characteristic morpho- metric expression (semi-circular, steep head and sidewalls, over deepened basin, and threshold or central basin mound) (Evans and Cox, 1974), cirque glaciers are an excellent marker of glacial processes on Earth. However, for understanding candidate martian cirque forms, it is important to rule out other possible formative processes and to test if they share similar morphometric expressions to those associated with terrestrial cirque glaciers. Other potential formative processes for the martian semicircular depressions could be mass wasting resulting in erosional slumps, rotational landslides and groundwater sapping channel heads (Carr, 1995; Davila et al., 2013). It is therefore vital to prove with a high degree of

confidence that these martian cirque-like alcoves are glacial cirque relic forms and not formed by non-glacial processes.

Previous studies have used a well-studied range of terrestrial analogs to validate evidence of glacial surficial processes at mid to high latitudes on Mars (Head and Marchant, 2003; Head et al., 2004; Shean et al., 2007; Dickson et al., 2008; Head et al., 2010; Scanlon et al., 2015). Typically, these studies have used traditional manual identification and mapping of glacial forms using satellite imagery. However, without the ground truth provided by “boots on the ground”, these studies could not verify a glacial origin. Hence, high-level comparisons of martian cirque-like forms to terrestrial analogs are limited to remote sensing techniques.

Due to the often-ambiguous nature of cirque geomorphic expressions (i.e., fuzzy edge boundaries, etc.) it is difficult to consistently define the cirque morphometric expressions necessary for automated identification. However, a recent study of terrestrial cirques successfully used an automated detection method called a Convolutional Neural Network (CNN) (Scuderi and Nagle-McNaughton, 2022) to identify cirques in California's Sierra Nevada Mountains. CNNs are hierarchical neural networks whose convolutional layers are reminiscent of neurons in the primary visual cortex of mammalian brains. A CNN is an artificial neural network that is primarily used to classify images, extract features and localize objects from images. While it is difficult for the human eye to extract useful patterns from digital elevation models (DEMs), CNN type algorithms can easily identify morphometric information for object detection. Other studies have used machine learning to detect and identify surface landforms on planetary bodies (Palafox et al., 2015; Wagstaff et al., 2018; DeLatte et al., 2019; Lee, 2019; Li et al., 2020; Nagle-McNaughton et al., 2020; Hsu et al., 2021) with great success. While limited studies have used computer automation to identify cirque forms on Earth (Li and Zhao, 2022; Scuderi and

Nagle-McNaughton, 2022), similar techniques have not been applied to cirque-like land- forms on Mars.

Here, we aim to identify candidate cirques on Mars using a CNN, and compare their characteristics with terrestrial cirque glaciers to address the following questions: 1) If martian cirque forms were created under similar conditions to terrestrial cirques, what are the implications for the martian environment during their formation? 2) Could the cirque forms have been created through different processes on Mars including modification of craters? 3) Is there evidence that could suggest relative timing for the cirque glacier forms and/or do they represent multiple episodes of glacial processes?

We conducted our analysis on a 50x50km region on the near-equatorial dichotomy boundary east of Gale crater to assess if martian semicircular depressions in this study area share similar morphometric traits to terrestrial cirques. Here we used an augmented off-the-shelf neural network "RetinaNet", a CNN initially trained to identify cirques on Earth (Scuderi and Nagle-McNaughton, 2022) to determine whether it could recognize cirque-like forms on Mars. We conducted morpho- metric measurements of candidate cirques identified using our method to further test whether they are glacial in origin. Based on our analysis we discuss the implications of the presence of cirque-like forms in the equatorial zone for the evolution of the martian cryosphere and past climate.

2.2 Scientific Background

Terrestrial cirques have a distinct morphologic expression, typically exhibiting a semicircular hollow with a concave profile. They are bounded by steep head and sidewalls but open down valley (Evans and Cox, 1974). Cirques typically have a flattish to bowl-shaped

depression derived from the glacial rotational flow above a lower threshold (Clark and Lewis, 1951; Evans and Cox, 1974, 1995; Evans, 2010; Dromart et al., 2021; Scuderi and Nagle-McNaughton, 2022) (Fig. 1).

While modern interpretations of terrestrial cirques are conclusive in finding glacial origins, a wide range of possible formative processes could have created cirque-like features on Mars (Davila et al., 2013; Souness and Hubbard, 2013; Ramy El-Maarry and Harrington, 2022; Soare et al., 2022). It is therefore important to note that these geomorphic forms could have been developed from entirely different processes, such as groundwater sapping channel heads or mass wasting processes. However, it is not the purpose of this study to examine all potential formative processes, but rather to test if they align with cirque glacier morphology/morphometry. Further, our methods were designed to discriminate between these possibilities rather than assume they are cirques due to their similar morphology.

Studies have documented cirque-like alcoves within the fretted terrain typically associated with the dichotomy boundary (Head et al., 2006; Davila et al., 2013). The dichotomy boundary is a global escarpment with several kilometers of relief. It separates the ancient, heavily cratered southern highlands and the northern lowlands. The dichotomy boundary is thought to originate during the pre-Noachian period (~4.5–4.1 Ga). The southern highlands date to the Noachian period (~3.7–4.5 Ga) and have highly degraded impact craters. The northern lowlands are younger (<3.7 Ga) and are generally lightly cratered plains of sedimentary and volcanic origin (Zuber et al., 2000). The dichotomy boundary's origin is largely enigmatic with models suggesting endo- genic, and multiple and single impact hypotheses (Marinova et al., 2008).

Fretted terrain is typically defined by massifs with highly irregular planimetric configurations dissected by U-shaped valleys (Sharp, 1973). Fretted terrain has been associated with in situ deformation due to subsurface ground ice and ice rich flow/creep typically associated with glacier processes (Sharp, 1973; Squyres, 1978, 1979; Lucchitta, 1984; Squyres et al., 1992). The majority of studies suggest that this terrain was formed by glacial scouring (Lucchitta, 1984; Head et al., 2006; Davila et al., 2013). However, some studies suggest it was formed by fluvial valleys that were subsequently modified by mass-wasting pro- cesses (Carr, 2001).

In addition to identifications in fretted terrain associated with the dichotomy boundary, martian cirques have been documented globally (Evans, 2007; Banks et al., 2008; Davila et al., 2013). For example, cirque-like alcoves have been documented previously near our study site and were noted as being reminiscent of small-scale hanging valleys on Earth (Brardinoni and Hassan, 2006). These features exhibit the classic profiles of glacial cirques, with a steep backwall, over-deepened to a smooth and often concave basin floor, and a pronounced lip defining the steep drop to the trough floor (Evans, 2007; Davila et al., 2013). Further, investigations at mid to high latitudes have shown evidence of flowing ice on Mars often forming integrated patterns, representing mass transportation that appears to begin in discrete cirque-like alcoves (Neukum et al., 2004; Dickson et al., 2008; Head and Marchant, 2009; Souness and Hubbard, 2013; Hubbard et al., 2014).

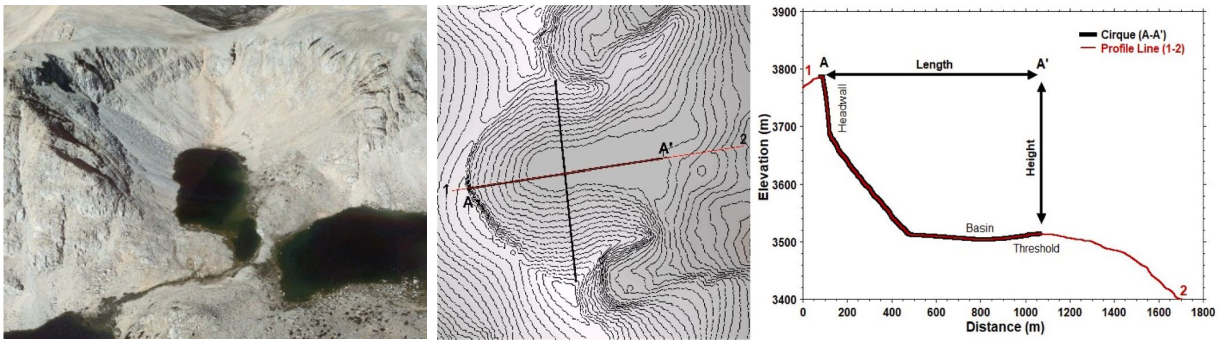

Figure. 1. Terrestrial example of a cirque alcove. Cirques are bowl-shaped depressions on the side of or near mountains that are bounded by steep head and sidewalls but open down valley and typically have a flattish to bowl shaped depression derived from the glacial rotational flow above a lower threshold. Left): Cirque alcove located in the Sierra Nevada mountains. Center): Cirque alcove on the left shown with a Digital Elevation Model (DEM) with 10 m contours. A-A' (length: 1075 m) notes cirque central axis. The perpendicular line denotes the cirque width. Up is north. Right): Cross section of the cirque alcove shown on the left and center images. Feature profile noted in red, cirque extent noted in black. Threshold lip marked where height is noted. Image credit: Left: Google Earth; Center and Right: Scuderi and Nagle-McNaughton, 2022.

2.2.1 Initial Data Generation

Scuderi and Nagle-McNaughton et al. (2022) developed a large terrestrial dataset of ~20,000 cirques and cirque-like forms using global Shuttle Radar Mission (SRTM) 30 m (1 Arc Second) DEM data (Farr et al., 2007; USGS, 2020). Out of this sample, 1951 well-defined closed-cirques were identified from 19 globally distributed mountainous areas (Scuderi and Nagle-McNaughton, 2022). Using the "Label objects for deep learning" tool in ArcGIS Pro 2.7 (https://pro.arcgis.com/en/pro-pp/latest/help/analysis/imageanalyst/label-objects-for-deep-learning.htm) (ESRI Inc. ArcMap 10.8.1. Redlands, 2021) they manually annotated cirques with

bounding boxes, the bounding boxes were positioned to capture the entire feature extent including a small neighboring area (Scuderi and Nagle-McNaughton, 2022). Terrestrial cirques were defined as exhibiting headwalls, sidewalls and some evidence of a threshold and a flat basin. Only cirques with well-defined presentations of these morphometries were included in the subset terrestrial training set. The trained model was applied to independent DEM data from the Sierra Nevada (California, USA) and was found to identify cirque forms with high confidence and consistency.

2.3 Study Area

The analysis was conducted on the dichotomy boundary near the martian equator approximately 850 km east of Gale Crater (Fig. 2). The 2500 km2 study area was selected since it both captures the range of features observed over the larger (~3200 km) equatorial zone dichotomy boundary and has excellent context camera (CTX) stereo coverage for producing digital elevation models for analysis.

2.4 Methods

We used the terrestrial cirque data set, identification methodology, and metrics from Scuderi and Nagle-McNaughton et al. (2022) which was designed to address issues with inconsistency in the recognition and definition of ambiguous landforms like cirques. Since there is no exact measurement of cirque “edges”, interpretations of cirque morphometry often differ from one study to the next, leading to inconsistent and ultimately differing opinions of the formative processes that create terrestrial cirque-like features. In addition to the difficulty attributed to ambiguous cirque morphometric expression, terrestrial cirque features also resemble a multitude of other surface features such as nivation hollows, depressions,

landslides, karstic depressions, and impact and volcanic craters (Scuderi and Nagle-McNaughton, 2022).

We used RetinaNet, an off-the-shelf neural network (Lin et al., 2017) for analysis. We trained the network using the 1951 closed cirques delineated from a global SRTM (1 arc sec) DEM data (USGS, 2020) (Fig. 3). We matched the terrestrial training parameters (form identification accuracy and mean average precision) and then used this terrestrially trained RetinaNet on DEMs of martian surfaces. Our objective was to use a terrestrially trained and validated CNN for cirque detection on Mars to help identify candidate cirque-like features and then to discriminate between other formative possibilities, supporting the hypothesis that cirque-like alcoves on Mars could be cirque remnants due to their similarity of form (Fig. 3).

Input data for training are DEMs and not traditional RGB images. Rather, the linear greyscale values of a DEM raster represent the spatial distribution of elevation across a scene. Use of DEM's allowed RetinaNet to analyze raw elevational data, typically difficult to extract manually (Bickel et al., 2018). Normally, DEMs are processed (i.e., slope and curvature analysis, edge detection, etc.) to extract and map morpho- metric information. However, and unlike the human eye, RetinaNet through its use of convolutional filtering can use DEM datasets to readily quantify elevational rates of change, object edges, boundary changes, curvature and the spatial distribution of these parameters that are fundamental to object detection (Nagle-McNaughton et al., 2022; Scuderi and Nagle-McNaughton, 2022). Further, the use of DEM's avoids the false negative feature identification associated with conventional image analysis, namely shadows, and albedo differences.

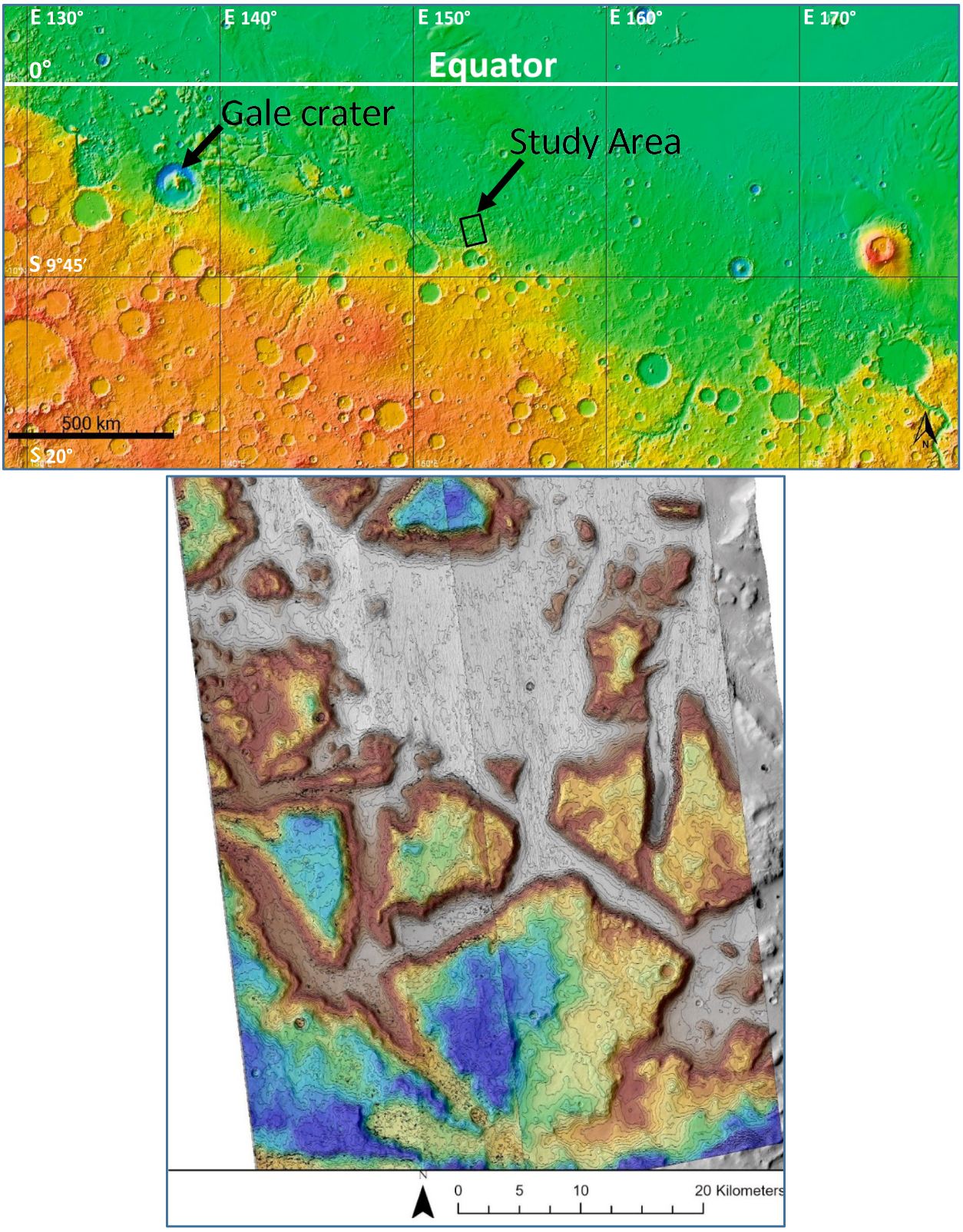

Figure 2. Study area. Top): Context area, tropical extent of the dichotomy boundary. Gale crater is approximately 850 km west of the study site. Black box indicates the position of the study area

located in the north portion of the Aeolis quadrangle, Mars. Bottom): Study site (center of image 8.020◦ S, 152.864◦ E). 25 m contour lines are overlain on 20 m/pixel resolution CTX DEMs. CTX DEMs were derived from two CTX stereo pairs (J03_046031_1725_XI_07S207W.tiff and F01_036167_1725_XI_07S207W, P05_002925_1730_XN_07S207W.tiff and F04_037512_1723_XI_07S207W) Background CTX images: J03_046031_1725_XI_07S207W and P05_002925_1730_XN_07S207W. Bottom and Top Image credit: NASA/JPL-Caltech/ESA/DLR/FU Berlin; Google Mars; Williams, J.M.

2.4.1 Data sources and processing

Images acquired by the Context Camera (CTX) and High Resolution Imaging Science Experiment (HiRISE) camera on the NASA Mars Reconnaissance Orbiter (MRO) spacecraft were identified and accessed via the Arizona State University (ASU) planet view website (https ://viewer.mars.asu.edu/viewer/ctx) (Malin et al., 2007). All images were sourced from NASA's Planetary Data System (PDS) archive and are freely available on that site.

In order to produce high quality DEMs, we identified CTX and HiRISE stereo pairs using the Java Mission-planning and Analysis for Remote Sensing tool (JMARS) (Christensen et al., 2009) and when necessary, augmented the stereo coverage with data from Google Mars 7.3.4 (https://www.google.com/mars/). Using these programs, we identified and downloaded CTX stereo pairs from the ASU School of Earth and Space Exploration Image Explorer using the planetary database source Experiment Data Record (EDR).

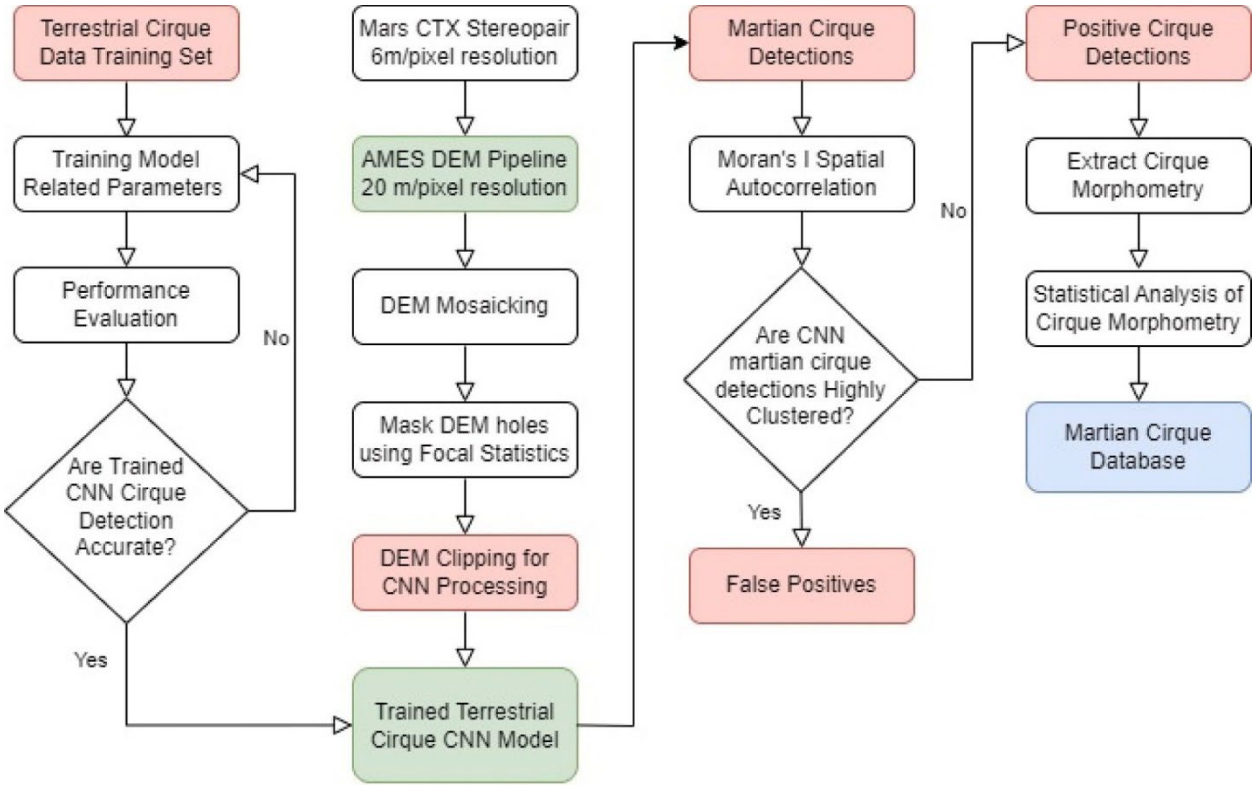

Figure 3. Methodology process flow chart.

2.4.2 DEM production and Mosaicking

The USGS ISIS3 and NASA Ames Stereo Pipeline (ASP) (Beyer et al., 2018) were used to create DEMs derived from CTX and, where available, HiRISE stereo observations. Using the ASP pipeline, we produced overlapping DEMs derived from two CTX stereo pairs (J03_046031_1725_XI_07S207W.tiff and F01_036167_1725_XI_07S20 7W, P05_002925_1730_XN_07S207W.tiff and F04_037512_1723_XI_07 S207W) with a spatial resolution of 20 m/pixel. We mosaicked the two DEM's to preserve coverage of possible cirque forms that otherwise were only partially covered by a single DEM (Fig. 3). The mosaicking procedure is covered in Appendix 1.

2.4.3 Limitations of Data Source

Depending on the capture angle and quality of the stereo derived the DEM's contained artifacts in the form of holes (null data). A workflow using the ArcGIS Pro 2.9.0 Focal Statistics Tool and a rectangular median 21 × 21 filter was created to mask the holes (ESRI, 2021). While this approach successfully filled large DEM holes where neighboring elevations were similar, DEM locations displaying substantial elevation differences with the elevations of neighboring features created less than desirable fill elevations. Therefore, any predictions associated with locations having fill errors were not included in the final results. The procedure is covered in more detail in Appendix 1.

2.4.4 DEM Clipping

DEM clipping consisted of two stages: 1) primary 50 × 50 km DEM manual clipping using ArcGIS Pro 2.9.0 and, 2) secondary smaller 1280 × 1280 pixel tile clipping using a python custom script necessary for CNN analysis. To optimize computer processing time, the secondary DEM clip was converted was then resampled to return 256 × 256 pixel tiles for analysis. Normalization necessary to match the terrestrial training tile (Scuderi and Nagle-McNaughton, 2022) to a 0 to 255 Gy scale was achieved using the uint8 data type. The procedure is covered in more detail in Appendix 1.

2.4.5 RetinaNet Training

Our model was trained using Keras RetinaNet (https://github.com/fizer/kerasretinanet) (Gaiser and de Vries, 2022), with a 50-layer CNN (ResNet50 backbone) and using transfer

learning (Pan and Yang, 2009; Torrey and Shavlik, 2010). Similar to Scuderi and Nagle-McNaughton et al.

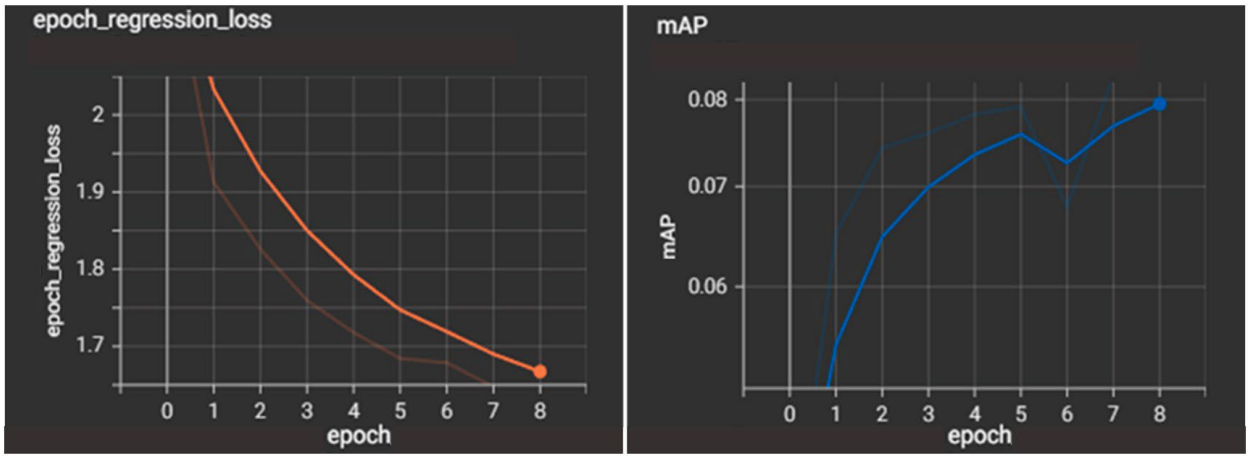

Figure 4. Epoch regression loss (left); Mean Average Precision (mAP) (right). This log detailed the training regression loss and mAP over eight epochs. The three epochs beyond epoch eight were not included as they indicated validation regression (decrease in model precision).

(2022), initial weights were the default 500-object classes from the Common Objects in Context (COCO) dataset (Lin et al., 2014). These weights control the signal or the strength of the connection between two neurons and are used to decide how much influence an input will have on the output. The backbone of a CNN refers to the feature extraction network which processes the input data and creates a specific feature representation. See Appendix 1 for details of the CNN training approach. Similar to the Scuderi and Nagle-McNaughton et al. (2022) study 1658 training samples were randomly augmented automatically for each epoch (Fig. 4) via various affine transformations (rotations, translations, shears, scaling, and flips), to enable better generalization in the model, increase spatial variance, and to avoid object recognition dependent on orientation, size or elevation range alone. Without this variance, the network will be useless

with features that do not exactly match the size and orientation of the training data. Including these transforms, the model was in effect trained on over 115,000 cirque forms.

We used a Confidence Level (CL) score threshold to assess identification accuracy. CL is the model's quantification of the detection prob- ability and ranges from 0 to 1. A lower CL score implies that the algorithm has assigned more uncertainty to a given detection than a higher CL score. A CL score of 0 would indicate a flat surface with no features to match with the trained form while a score of 1 would indicate a perfect match to the trained form which would be highly unlikely given the noise of natural forms (Scuderi and Nagle-McNaughton, 2022).

2.4.6 RetinaNet Evaluation

Martian DEMs that were created from CTX stereo pairs were analyzed via a RetinaNet trained to identify terrestrial cirques to test if it could identify cirques on Mars. Due to the investigative nature of this study, further training to remove possible false positive and negative identifications was not completed. Rather, we visually assessed the quantity and character of possible false positives and negatives here to evaluate the success criteria with the initial training set and to identify areas of future work.

2.4.7 Training Hardware

The RetinaNet model was trained on relatively low-end hardware: an NVIDIA GeForce RTX 3060 GPU CPU, and 32 GB of 2667 MHz RAM. With this hardware, each epoch of the model took approximately twenty minutes. Thus, the final model was trained in ~6.5 h. This training time could be reduced with more powerful hardware.

2.4.8 Morphometric Measures

Morphometric measurements were extracted from the detected forms (Fig. 3). These included threshold elevation, length, width, headwall height, length/width ratios, length/headwall height ratios, area, perimeter, circularity, and amplitude. The threshold elevation is defined as elevation of the toe or lip if present. As defined by Evans and Cox (1995), the cirque length is the length of the median axis, from the focus (middle of the threshold) to the crest, dividing the feature into two equal halves, left and right. The width of the cirque is the maximum dimension measured at right angles to the median axis. Headwall height is the greatest range in altitude on headwall along the axial slope line.

2.5 Results

2.5.1 Martian Cirque Identification

Within the study area, the RetinaNet model initially detected 3244 objects with CL scores ranging from 0.20 to 0.97 (Fig. 5). Of the total detections (Figs. 6, 7), 99.18 % were identified as false positives attributed to crater forms, DEM artifacts, or tile edge effects. While edge effects and DEM artifacts were expected due to previous experience with the terrestrial dataset, the large number of detections attributed to craters was a new result. This is primarily due to the lack of viable training data (lack of craters) in the terrestrial training dataset. False positives associated with DEMs were also highly clustered. The ‘Spatial Autocorrelation’ (Morans I), ArcGIS ‘Buffer’ and ‘Select by Location’ tools were used to automatically remove highly clustered false detections associated with tile edge effects artifacts and craters. After eliminating these analysis artifacts and misidentified cirque forms, the remaining 27 (0.82 %) identified candidate cirques

had CL scores ranging from 0.21 to 0.75 (Figs. 6, 7, 8); 16 of which were visually confirmed as exhibiting marginal to excellent cirque-like forms.

2.5.2 Cirque Statistics

The mean Confidence Level score for all Mars cirque detections (27) was 0.491. Morphometric data from these forms were extracted and recorded. The morphometric comparison between terrestrial and martian forms showed significant differences ($P \ll 0.05$) in length, width and height (Table 1). Martian cirque-like forms were generally larger in area (~150 %) than their terrestrial analogs. However, martian head- wall heights were smaller (~26 %) than terrestrial cirque forms. Like terrestrial cirques, martian cirque dimensions increased with higher CL scores, suggesting larger cirques on Mars might have had time to fully develop. The mean L/W ratios for the 27 martian cirque forms were significantly different ($P \ll 0.05$) than terrestrial cirque forms (1.249 and 1.313 respectively). L/H scores for martian and terrestrial cirque forms were significantly different ($P < 0.05$), most likely due to the difference in headwall heights with significantly shorter heights on Mars relative to the other dimensions of the cirque forms. The mean circularity difference was statistically insignificant ($P = 0.220$).

Allometric relationships capture the degree to which an objects' shape changes proportionately as it grows. For terrestrial cirques map- ped in Scuderi and Nagle-McNaughton et al. (2022) length increased faster than width and height with an increase in cirque size (Fig. 9 Right). Unlike terrestrial cirques, we found that the martian features (Fig. 9 Left) show a proportional relationship between the increase in length and width with size. However, height increased with size at a faster rate. Thus, we do not see the maintenance of constant shape

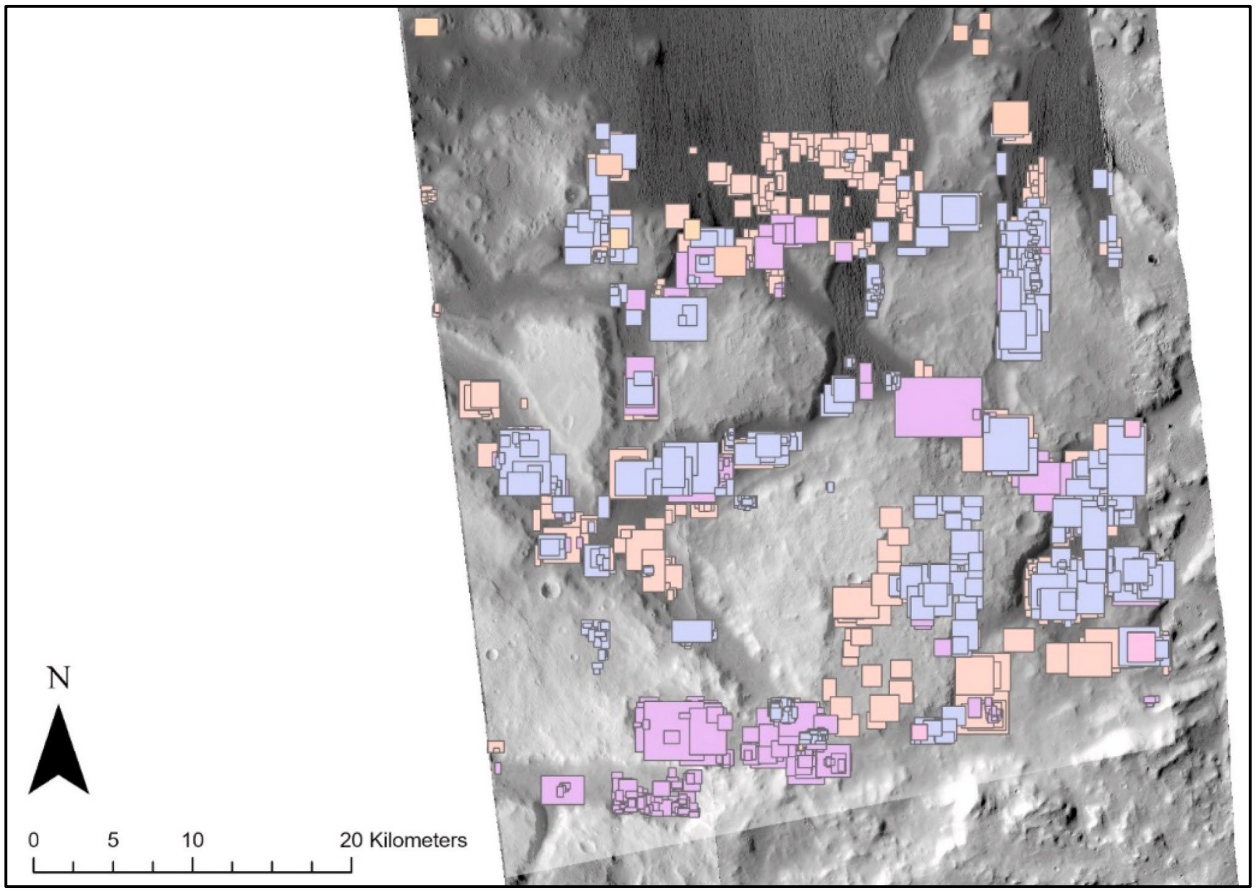

Figure 5. All 3248 cirque detections within the study area. Cirque box color indicates different RetinaNet passes. Multiple passes were required to cover the full extent of the DEM within the study area. Background CTX images: J03_046031_1725_XI_07S207W and P05_002925_1730_XN_07S207W. Image credit: NASA/JPL-Caltech/ ESA/DLR/FU Berlin; Google Earth; Williams, J.M.

(Evans, 2007). This is opposite to observed allometric relationships in terrestrial analogs and could be due to a number of reasons such as, but not limited to; 1) our candidate martian cirques are not cirque glacier remnants, but rather created through another formative process, 2) the martian sample group (n = 27) is far too small to exhibit the relationship commonly documented in terrestrial analogs, 3) cirque glaciers evolve differently on Mars due to lower

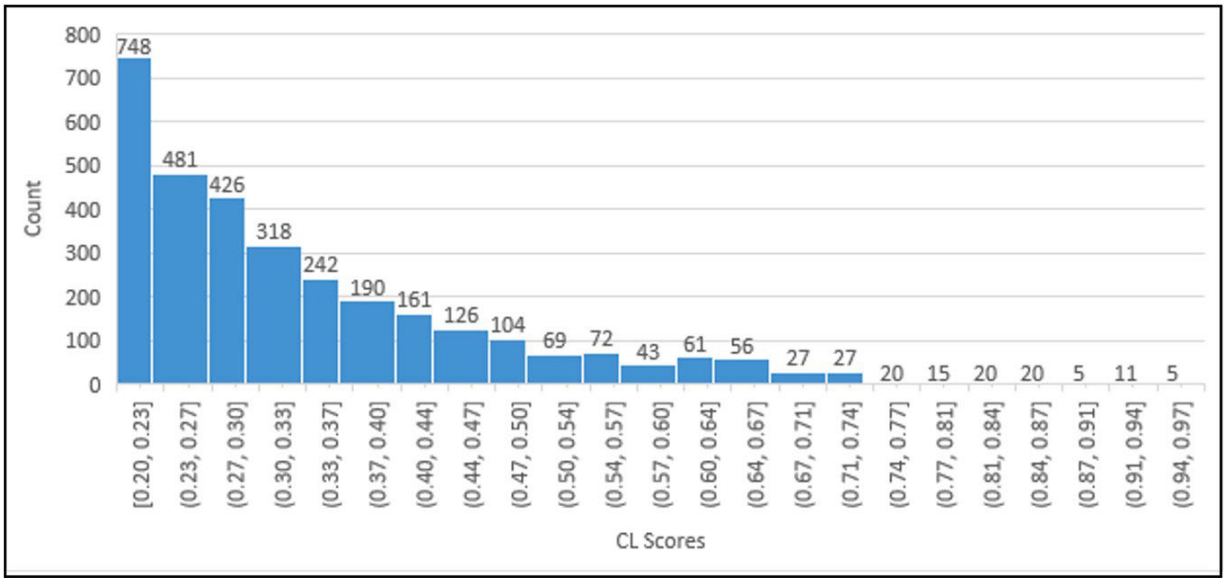

Figure 6. Confidence Level (CL) scores for all 3244 cirques identified above the cutoff (0.20 CL). The CL score is a measure of model confidence in the prediction. The majority of the CL scores (70 % of the total population) populate at the lower end of CL scores from 0.20 to 0.40. gravity influencing glacial flow dynamics, or 4) martian cirque morphometric expressions are the result of cold based rather than wet based glacial processes. While a larger sample size will be necessary to further investigate this relationship difference, it is important to note that some small terrestrial cirque samples exhibit similar relationships (Olyphant, 1981).

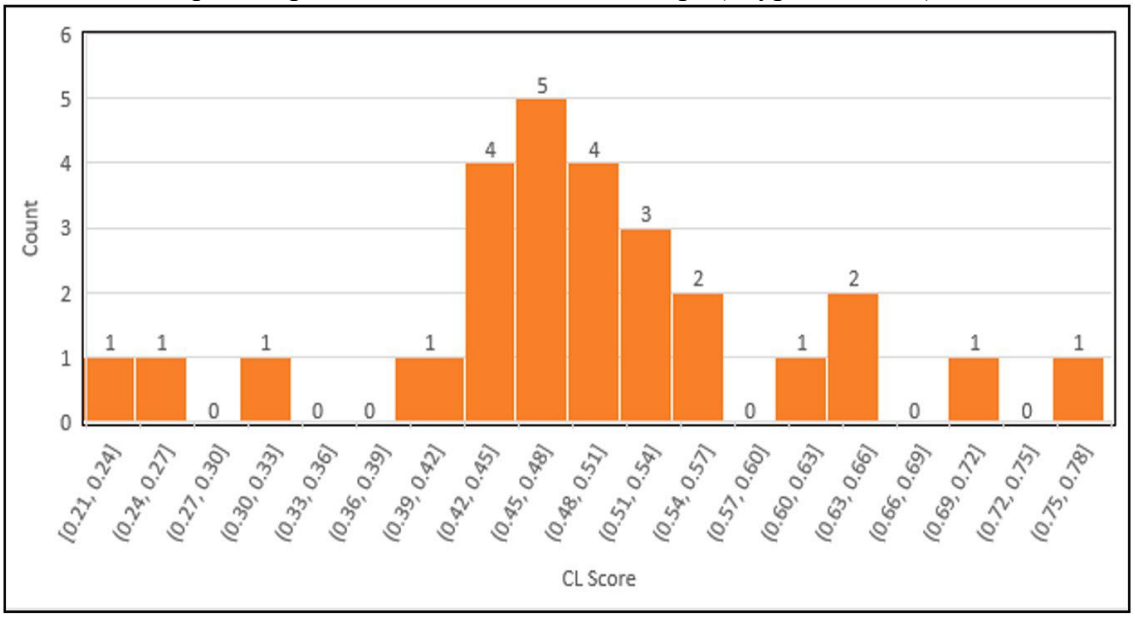

Figure 7. Confidence Level (CL) scores for cirques (n = 27) identified above the cutoff (0.20 CL) after eliminating misidentified cirque forms. The CL score is a measure of model confidence in the prediction. The majority of the CL scores (70 % of the total population) are close to mean value (0.49) with CL scores ranging from 0.40 to 0.60.

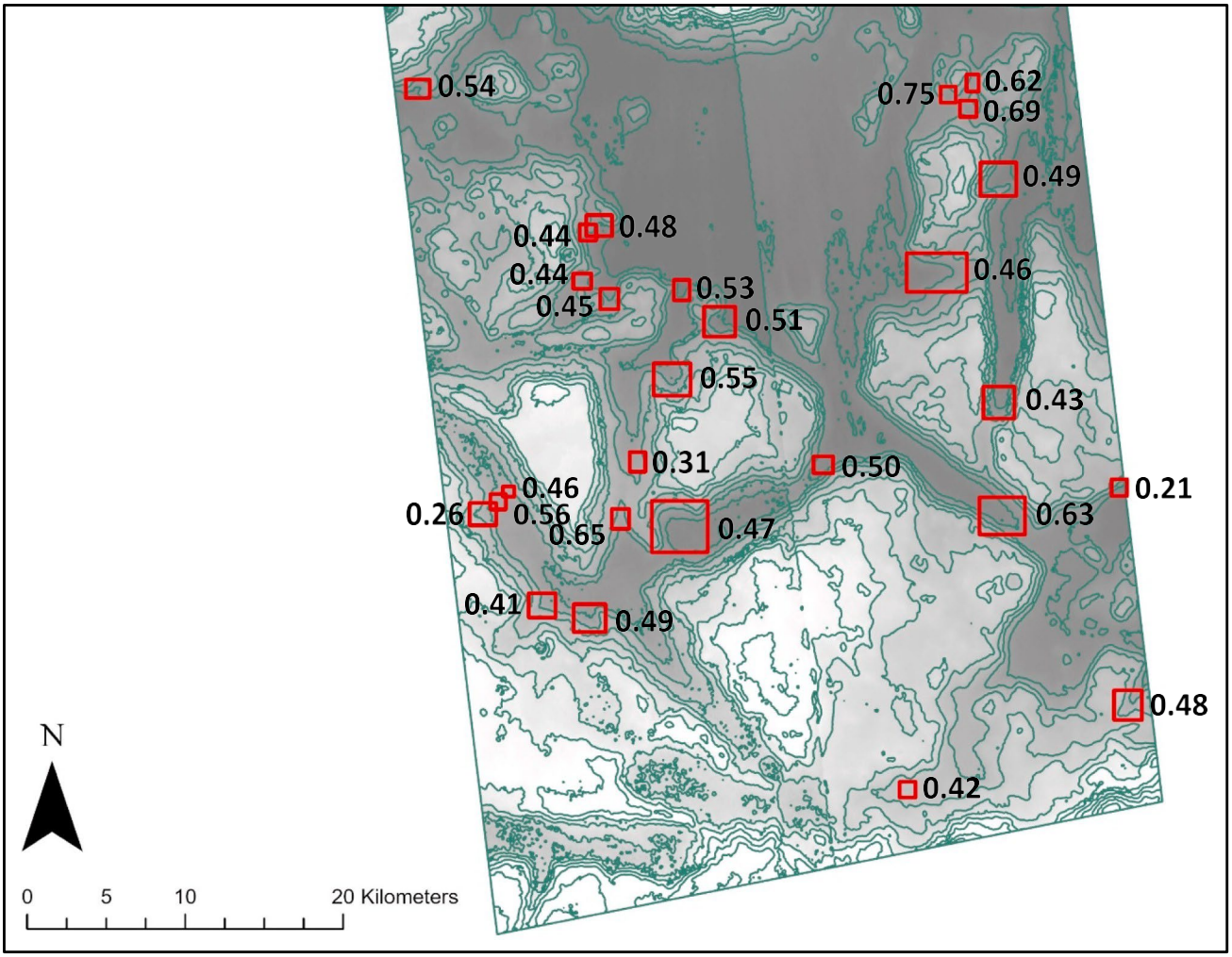

Figure 8. CNN (RetinaNet) model applied to the martian dichotomy boundary study site located in the equatorial region (center of image 8◦ 1′11.74″S, 152◦51′49.44″E). Red boxes (27) indicate positive RetinaNet cirque detections with CL scores remaining after removal of false positive detections associated with craters, edge effects and DEM artifact detections. Positive cirque form detections appear to concentrate on the edge of massifs typically associated with fretted terrain. 100 m contour lines are overlain on 20 m/pixel resolution CTX DEMs. CTX DEMs are derived

from two CTX stereo pairs (J03_046031_1725_XI_07S207W.tiff and F01_036167_1725_XI_07S207W, P05_002925_1730_XN_07S207W.tiff and F04_037512_1723_XI_07S207W).

Table 1
Identified cirque statistics.

Variable	All						High CL scores						Low CL scores					
	Mean (m)	St. Dev. (m)	Min. (m)	Max. (m)	Terrestrial Data t-statistic	Terrestrial Data *P*-value	Mean (m)	St. Dev. (m)	Min. (m)	Max. (m)	Terrestrial Data t-statistic	Terrestrial Data P-value	Mean (m)	St. Dev. (m)	Min. (m)	Max. (m)	Terrestrial Data t-statistic	Terrestrial Data P-value
Threshold elevation (m)	−1663	112	−1840	−1325	102.197	$P < 0.0001$	102.197	86	−1840	−1550	72.472	$P < 0.0001$	−1604	148	−1750	−1325	104.308	$P < 0.0001$
Length (m)	1553	763	603	3593	−5.754	$P < 0.0001$	1485	863	881	3519	−5.051	$P < 0.0001$	1233	207	1021	1578	−3.543	$P = 0.0005$
Width (m)	1316	706	567	3672	−6.817	$P < 0.0001$	1196	646	706	2341	−2.964	$P < 0.0001$	1057	363	567	1744	−2.217	$P = 0.0279$
Wall height (m)	86	65	25	275	11.864	$P < 0.0001$	68	61	25	175	13.88	$P < 0.0001$	84	53	25	175	10.044	$P < 0.0001$
L/W ratio	1.232	0.284	0.781	2.004	11.298	$P < 0.0001$	1.249	0.199	0.944	1.533	−1.883	$P = 0.0613$	1.221	0.301	0.905	1.845	−2.906	$P = 0.0041$
L/H ratio	27.535	20.612	5.977	90.400	−15.159	$P < 0.0001$	31.045	18.982	8.480	70.380	−18.683	$P < 0.0001$	21.987	15.472	5.977	47.720	−15.459	$P < 0.0001$
Area (m2 X103)	1803	1871	261	7106	−5.877	$P < 0.0001$	1564	1768	473	5555	−3.834	$P = 0.0002$	995	534	447	2257	−1.203	$P = 0.2307$
Perimeter (m)	4588	2209	1825	10,095	−5.727	$P < 0.0001$	4213	2227	2551	8991	−2.697	$P = 0.0076$	3676	886	2627	5533	−2.232	$P = 0.0268$
Circularity	0.886	0.053	0.703	0.983	1.23	$P = 0.2203$	0.897	0.026	0.854	0.934	−2.755	$P = 0.0064$	0.881	0.050	0.792	0.926	0	$P = 1.0000$
Amplitude (m)	119	86	10	280	n/a	n/a	86	88	10	270	n/a	n/a	114	74	25	280	n/a	n/a

All Confidence Level scores (All: $N = 26$, 0.75 to 0.21). Cirques with highest model Confidence Level score (high: $N = 9$, CL from 0.75 to 0.53). Cirques with lowest model Confidence Level score (low: N = 9, CL from 0.44 to 0.21).

2.6 Discussion/Interpretation

In this study, we use a terrestrially trained and validated CNN that detected cirque features on the Earth with high accuracy and applied it to a DEM representation of martian surfaces within our equatorial dichotomy boundary study area (Fig. 2). The purpose of using this automated procedure was to identify with high confidence whether these landforms were cirques. Therefore, no further training of the CNN algorithm incorporating previously hypothesized martian cirque forms from prior studies were used to assess whether a CNN trained on terrestrial cirques could be used to identify potential cirques on Mars.

The RetinaNet CNN trained with terrestrial cirque forms detected over 3248 forms with an average CL score of 0.35. However, a large portion (99 %) of the initial RetinaNet detections were false positives. This was largely due to false positives associated with crater forms, DEM defects, and tile edge effects (Fig. 10). Inspection of misdetections on crater forms revealed that the algorithm selected ID boxes on only a portion of any given crater. These false detections were expected due to the similarity of a crater half form to that of a cirque and because our terrestrially trained RetinaNet had no crater forms in the training or validation dataset. These false detections were removed though filtering of the CNN results.

Like false-positives associated with crater forms, false-positives associated with DEM defects, tile boundaries and ‘filled holes’ appeared to have similar issues and were removed using the ArcGIS Pro “Select by Location” tool. We then assessed the RetinaNet's CL scores of the remaining 27 features, extracted their morphometric parameters, and compared them to terrestrial analogs.

2.6.1 False Negatives

Investigation of the study area revealed that the algorithm is not capturing "nested" cirque forms where one cirque is inset within another larger cirque (Fig. 11). The algorithm does not detect the larger cirque possibly due to disruption of the morphometric signature by the smaller interior cirque form. In this case the algorithm often produced identifications that did not cover the entire extent of the form, often missing the entirety of the headwall or sidewalls. It is unclear why RetinaNet does this, as the identification boxes for terrestrial cirque forms typically cover the entirety of the cirque. One possible explanation for this is that the algorithm misidentifies the larger feature boundaries due to shallow headwall and sidewall heights. Morphometric examination of the larger outer nested cirque yielded similar morphometric measurements as the interior smaller cirque with no significant statistical difference.

Visual evaluation of the remaining 27 cirque forms showed that 12 were poor examples of traditional cirque forms, nine represented moderate well-expressed examples and seven represented excellent examples of cirques relative to our terrestrial training set data. Within the study area the distribution of cirque forms appears to be concentrated on the edge of the massifs associated with fretted terrain on the dichotomy boundary (Fig. 8) with the orientation of the general topography providing locations for cirque development. Cirque form directionality is concentrated towards the NW, and SE (Fig. 12) with a secondary component facing NE. The development of morphologies for the cirque forms in the study is likely directly tied to solar insolation variables, such as latitude, time of year, topographic slope, aspect, and shadowing. This in turn controls the spatial distribution, directionality, and the potential mass balance within these features.

Morphometric analysis also provides clues to the past insolation regimes that may have produced these features. Terrestrial cirques face slightly east of poleward on average, therefore, cirque aspect distribution can provide a constraint on paleoclimatic reconstructions (Evans, 1977). On Earth the reduced ablation, as seen in poleward shadier cirque aspects, leads to increased local mass balance (Evans and Cox, 2005). However, this may not be the case on Mars if these equatorial cirques formed during periods of high obliquity. This would create a scenario where seasonal solar insolation would dramatically change from one pole to the other. It is logical to assume that during high obliquity periods martian seasons would vacillate from much warmer "summers" and much colder "winters". This variable effect on cirque forms could in part explain the general NW, NE and SE directionality shown within the study site (Fig. 12).

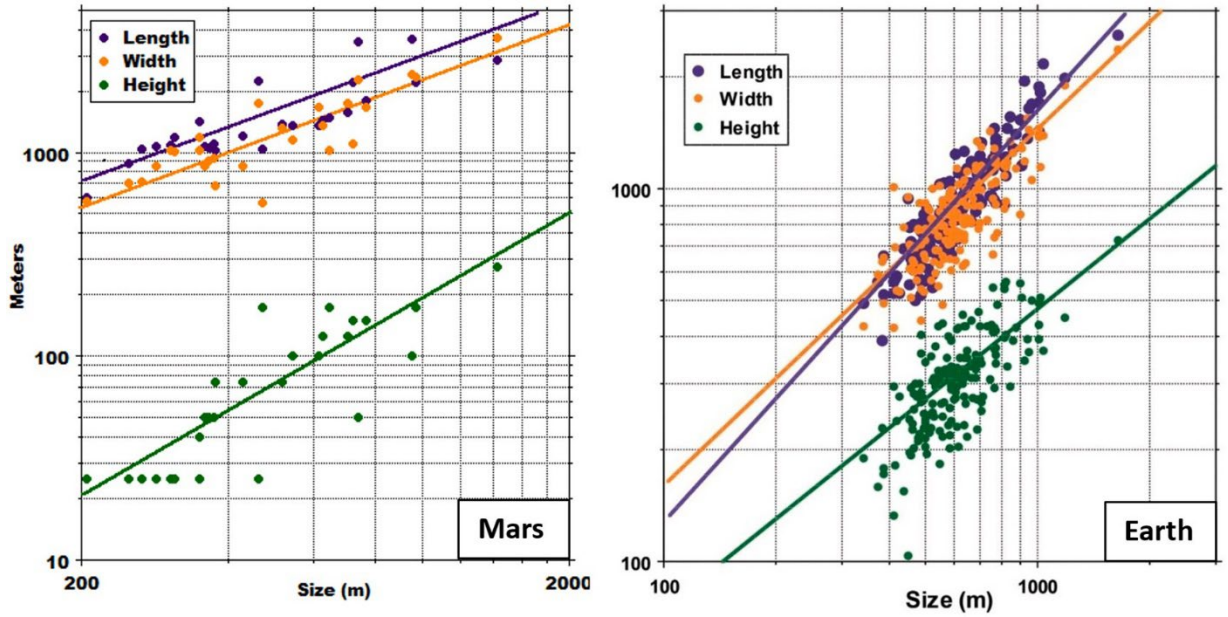

Figure 9. Left: Allometric plot of features in the martian study area (n = 27). Purple, orange and green lines represent the regression lines for length, width and height, respectively. For these martian features, length and width appear to increase proportionally to each other. Y-axis scale is dimension in meters for all variables. Right: Allometric plot of terrestrial cirques in the Sierra Nevada (n = 161). Purple, orange and green lines represent the regression lines for length, width

and height, respectively. For these Sierra Nevada cirques, the slight lengthening bias observed may be in part due to mutual interference between highly clustered cirques, which may restrict cirque widening. Y-axis scale is dimension in meters for all variables. (right figure after Scuderi and Nagle-McNaughton, 2022).

2.6.2 Evaluation

It is possible that preexisting structural constraints or strong structural lineation tied to the fretted terrain may partially control modal cirque aspect. Our RetinaNet analysis provides one line of empirical evidence that these semi-circular depressions could be relict cirque forms. However, they appear to differ from the terrestrial cirques in that they are larger (~150 % of terrestrial) on average and have lower (25 % of terrestrial) headwalls. Morphometric analysis

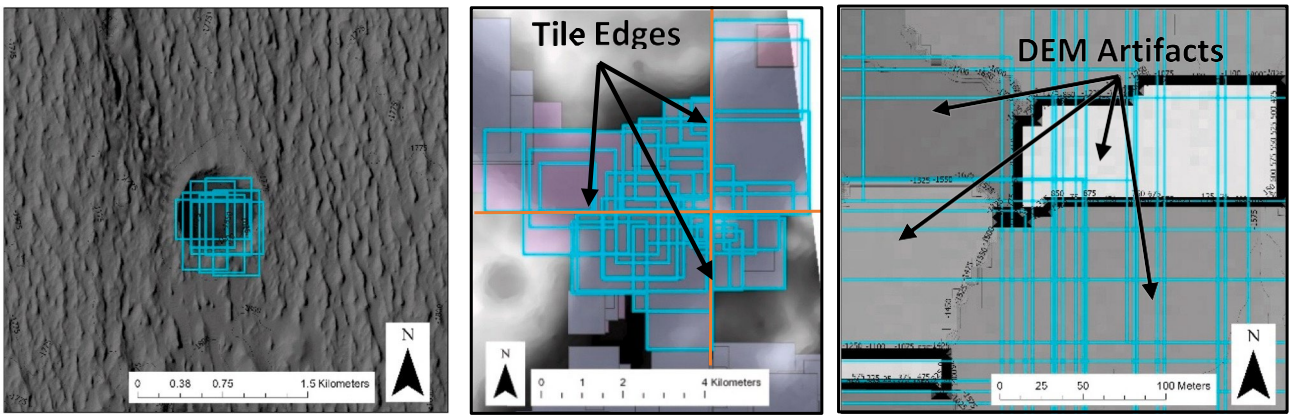

Figure 10. Left: False positive CNN detection cluster (red boxes) due to crater form surrounded by dune field. Middle: False positive CNN detection due to tile edge effect. Highlighted (blue) detection boxes overlaid on four DEM tiles (Orange Lines indicate tile border). Right: False positive CNN detection due to tile edge effect. Image credit: NASA/JPL-Caltech/ESA/DLR/FU Berlin; Google Earth; Williams, J.M.

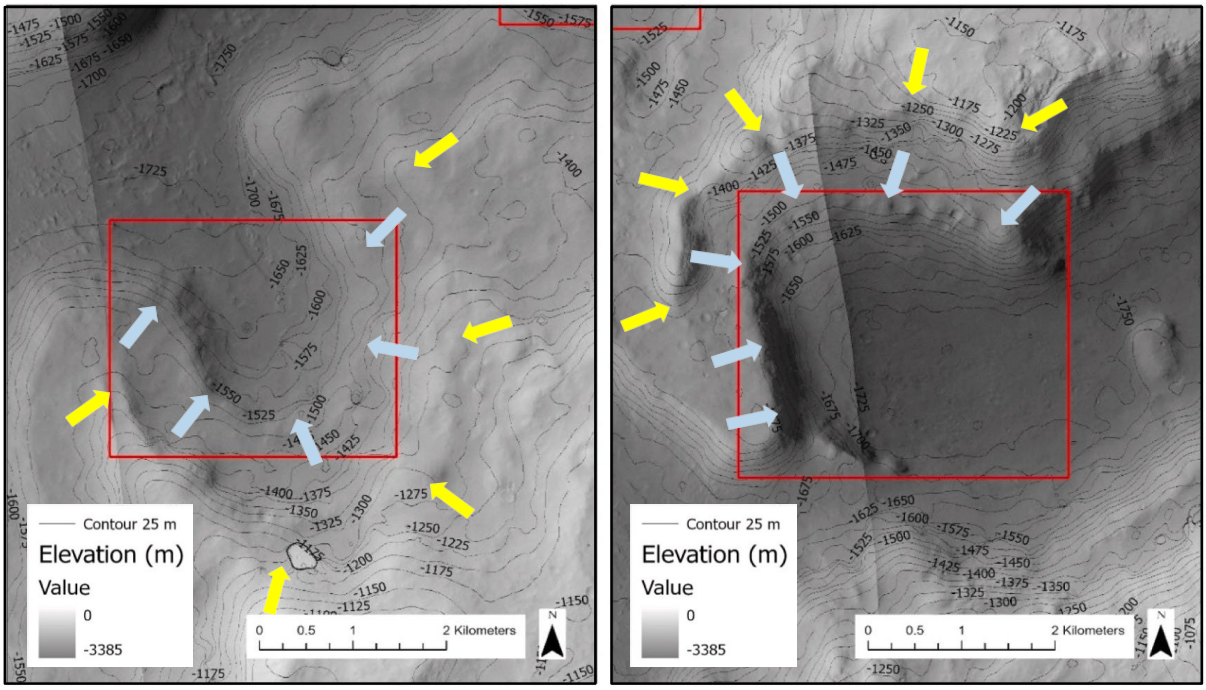

Figure 11. Nested cirque examples within the study area. Blue arrows indicate the edge of a detected cirque form. Yellow arrows indicate the edge of an outer cirque form missed by the algorithm. Left: (center of image 7◦57′56.83″S, 152◦40′17.27″E). Right: (center of image 8◦7′2.53″S, 152◦40′21.86″E).

suggests that these martian cirque-like forms, while like terrestrial cirques, differ in ways not observed in terrestrial forms. However, this does not rule out the possibility that the fundamental formative driving forces for both forms are essentially the same. One possible explanation for the difference in cirque form/size relationships could be the fact that they were eroded under a lower gravitational force compared to terrestrial gravity. A higher mass threshold could be necessary for glacier ice to flow and thus a larger accumulation of ice would be necessary for the glacial body to flow under its own weight (Patterson, 1984). In this case, larger accu- mulated ice mass

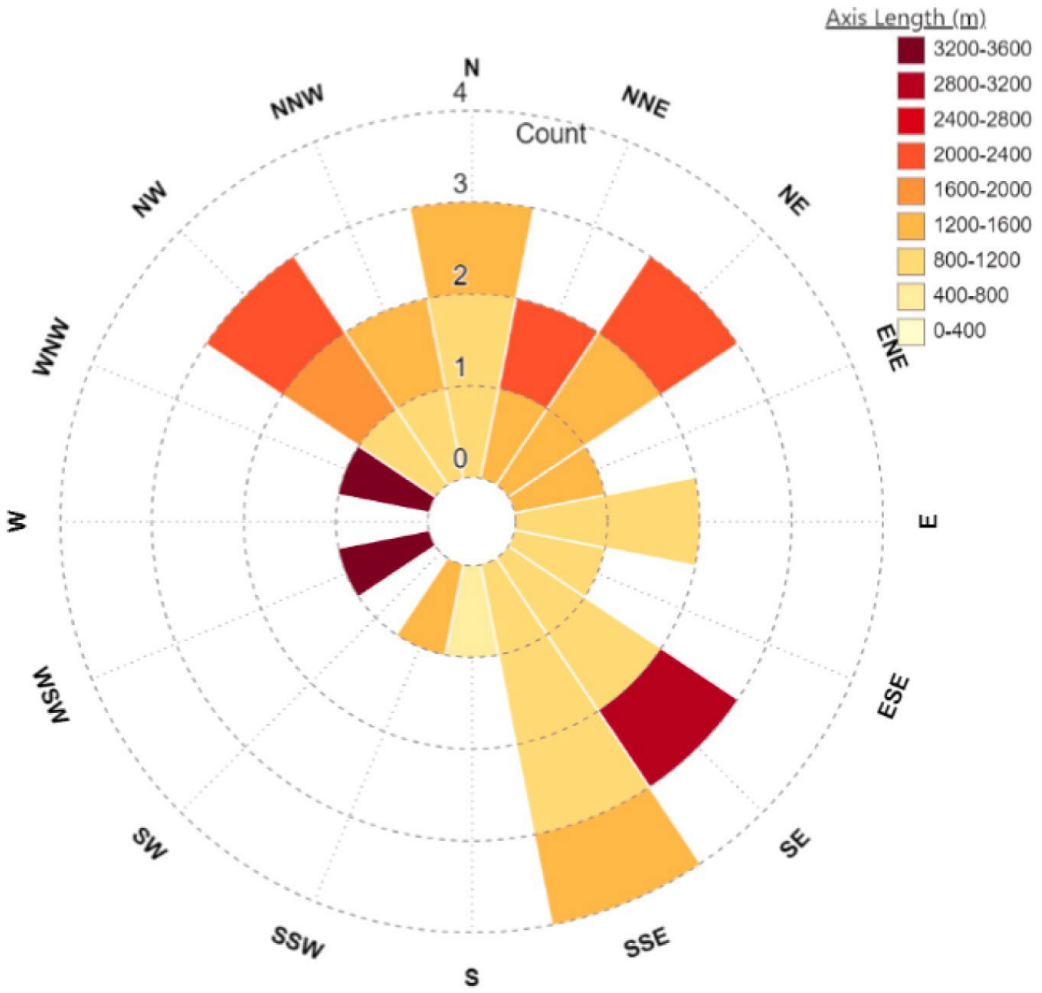

Figure 12. Rose diagram depicting the 27-cirque form center axis line direction, count and axis length. Image made with www.WindRose.xyz.

would lead to larger and potentially flatter depressions created by altered or shallower rotational flow of the cirque glacier (Patterson, 1984; Colaprete and Jakosky, 1998; Pelletier et al., 2010).

Pelletier et al. (2010) suggested that the lower slopes and higher temperature-controlled ice viscosities are responsible for the overall larger cirque sizes compared to terrestrial analogs. Another possible explanation for why these forms differ from terrestrial analogs could be that they are not traditional cirque forms and that they are formed through different processes. This is

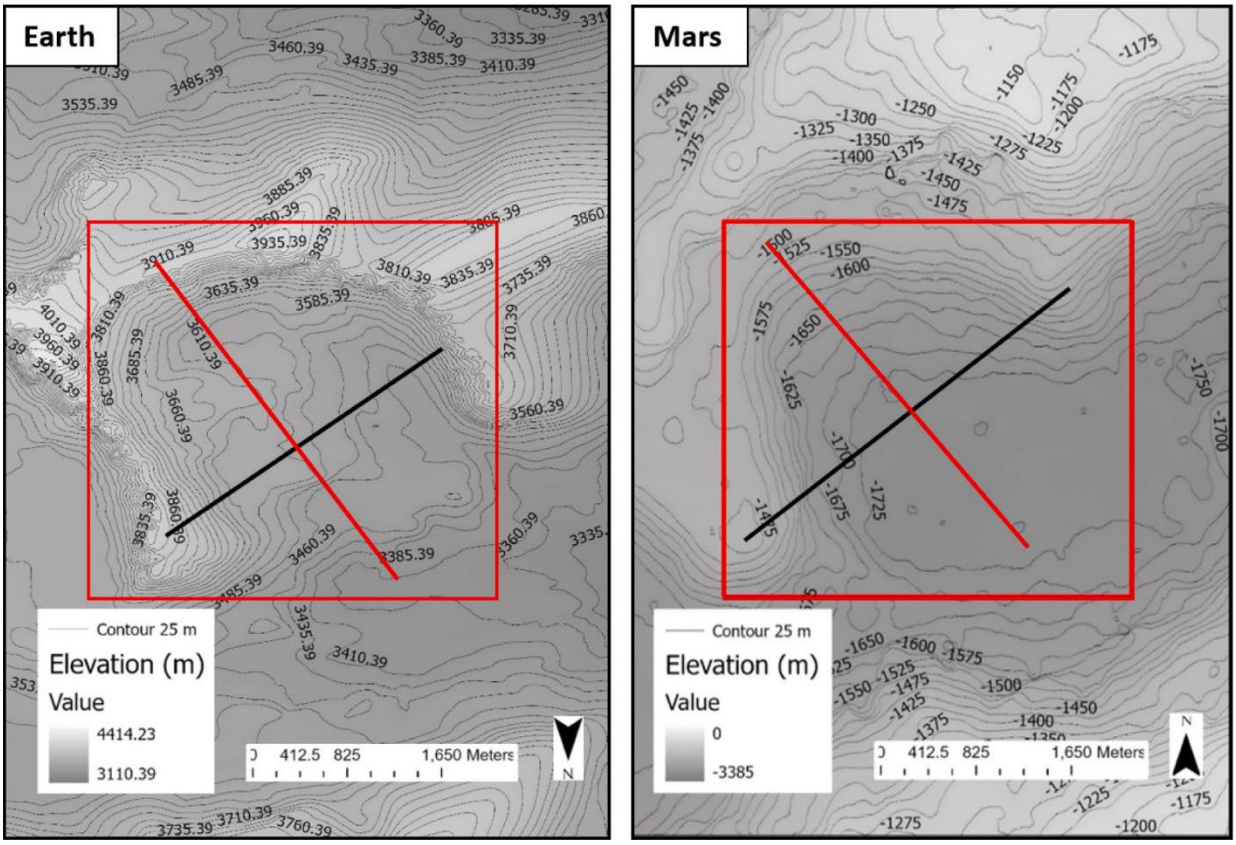

Figure 13. Comparison of terrestrial and martian cirque forms Left: Large terrestrial cirque example within the terrestrial cirque training set (center of image 36◦35′35.76″N, 118◦19′48.00″W). Cirque axis (red line) length 2200 m, width (black line) 2024, L/W ratio is 1.087. Note: North is down on this image to facilitate comparison with the Martian feature in the right panel. Right: Large martian cirque detection (red box), CL score 0.47 within study area (center of image 8◦ 7′2.53″S, 152◦40′21.86″E). Cirque axis (red line) length 2200 m, width (black line) 2024, L/W ratio is 0.781. Image credit: J. Williams.

not to say they are not glacial, but rather formed through a different evolutionary path. It is important to note that the martian cirque-like forms have a statistically significantly similar L/W ratio for cirque forms identified with a high CL score. For the martian cirque detections, the higher CL scores typically correlate to excellent examples of cirque forms. This supports a

hypothesis that they could be derived from cirque glaciers like terrestrial cirques but differing only in overall size.

2.6.3 Aeolian Reworking

Aeolian processes are the dominant formative agent on modern Mars and have been cited as a likely driving mechanism for redistribution of many tens of thousands of cubic kilometers of sediment across Mars' surface (Malin and Edgett, 2000; Schon et al., 2012; Day et al., 2016; Williams et al., 2020). There is clear evidence of aeolian reworking of many of the cirque forms (Fig. 11 left). However, most high scoring CL cirque forms do not show evidence of aeolian deposition such as dune fields or mantling Transverse Aeolian Ridges (TARs). Rather, the floor of most cirque forms appear to have craters scarring the surface. These cratered surfaces could be used in a future study to ascertain the relative ages of the cirque forms via crater statistics. Some of these cirque forms also show evidence of dust covering; however, it is difficult to ascertain exactly how much dust infilling has occurred as the CTX resolution is limited to 6 m/pixel. Aeolian erosion or deflation of the surface could be another possible reason for the shallowing and smoothing of the head- walls found on the martian cirques. Further, parallel retreat of the head and sidewall wall scarps under aeolian dominated post-glacial conditions could aid in the lengthening and widening relict cirque forms on Mars.

2.6.4 Formative Scenarios

If martian cirques develop like their terrestrial counterparts this could indicate similar formative environments on both planets. Typically, terrestrial cirque glaciers form under warm-based scenarios with glacial meltwater at the basal glacier/rock interface. This facilitates glacial rotational flow that produces the basal scouring and over deepening traditionally seen in cirques. If this was the case for the martian cirque forms we identified, this would imply an environment that was more like terrestrial analogs (Fig. 13). However, some terrestrial cirques in very cold environments form by a combination of cold and warm- based processes with vacillation between the two due to environ- mental change (Richardson and Holmlund, 1996; Head and Marchant, 2003; Crest et al., 2017). This alternation between warm and cold-based processes provides another scenario in which these martian cirque forms could have evolved during past obliquity variations. Alternatively, they may have originated similar to terrestrial cirques but with the process of initiation and expansion process possibly aided by preexisting craters. Other possible formative processes postulated for these forms include erosional slumps, rotational landslides, groundwater sapping channel heads or other forms of mass wasting.

As previously noted, cirque-like depressions in this study are located on an equatorial extent of the dichotomy boundary fretted terrain. Carr (2001) suggests that the formation of the fretted terrain and cirque-like depressions could be associated with mass wasting, however, mass wasting cannot explain all characteristics of the fretted terrain. Further erosional slumping, rotational landslides, groundwater sapping channel heads or other forms of mass wasting does not explain transport and removal of subsurface materials followed by undermining and collapse of the U-shaped valleys and cirque-like alcoves associated with the fretted terrain. Carr et al. (2001) proposes that the fretted terrain could have been formed early in the planet's history,

mostly because of mass wasting along scarps, accompanied by water-lubricated creep of the resulting debris, and subsurface erosion and solution. Headward extension of the stubby tributaries may have been altered by mass wasting aided by the presence of groundwater, as with most terrestrial valleys that form by sapping. Therefore, the resulting debris moved down valley by mass wasting and not by fluvial transport, as is the case with most terrestrial valleys. However, this does not fully explain the wide shallow U-shaped valleys, or the well-defined cirque-like amphitheaters often located at the head of these valleys.

Sapping has been invoked to explain U-shaped cross-sectional pro- files of fretted valleys on Mars (Carr, 1995). However, as Carr et al. (2001) notes in their study of concentric lobate ridges and cirque valleys, sapping cannot account for the totality of geomorphologic features in our equatorial study area. Carr et al. (2001) also describe, and we concur, that a glacial hypothesis explains the diversity of geo- morphologic features exhibited in our study area without excluding sapping, which is commonly observed in association with glacial processes because warm based glaciers represent sources of subglacial meltwater that can contribute to the erosion of valley walls by groundwater discharge (Davila et al., 2013). Alternatively, these cirque forms may have been created through entirely different processes on Mars due to environmental processes and changes not typically seen on the Earth.

2.7 Conclusion

Growing evidence suggests that the martian cryosphere expanded equatorward during periods of high obliquity in the recent past (10s–100s ka) (Head et al., 2005; Forget et al., 2006; Hepburn et al., 2019; Williams et al., 2022). However, the timing and extent of these periods remain poorly constrained (Williams et al., 2018). If the cirque-

like forms we analyzed were created through glacial processes these equatorial cirques could be ancient, and the relative timing of their creation could be as old as the Hesperian to Amazonian transition (~3 Ga). However, they could have formed due to the equatorward redistribution of the martian cryosphere during more recent periods of high obliquity oscillations. If this is the case then cirque glacier formation could be episodic, ebbing and waning along with climatic change associated with these oscillations. Further, cirque glaciers typically mark the beginning and end of glacial periods, and such are typically more climate change resistant (Lopez-Moreno et al., 2006). This could be the case for the martian cirque glacier forms and lends itself to the hypothesis that they could be chronologically tied to obliquity oscillations (>35◦).

Barring scale differences, headwall height differences and false positive CNN identifications, results from this study suggest that these martian forms are like the terrestrial cirque analogs in several ways, namely; 1) appearance, 2) L/W ratios, and 3) circularity. Their consistently high confidence scores when evaluated with a terrestrial cirque CNN training set suggests that they are cirques.

2.7.1 Future Work

To support the theory that equatorial ice was not only stable at the surface of Mars at the equator, but long lasting enough to support glacial processes, further investigations are needed to study and map the furthest expression of this possibly equatorward migration. Future work includes expanding this analysis to a larger portion of the dichotomy boundary with automated extraction of morphometric characteristics of these features (Li and Zhao, 2022). This larger sample size would allow evaluation of whether lithological and structural control of both cirque

form and location is responsible for differences between martian cirque forms and terrestrial equivalents. Future work should involve further training the CNN on martian cirque alcoves to help reduce false positive detections and include nested cirque forms.

Further, future work will also include enhanced automated detection/deletion of craters, and further automation of DEM production using the ASP and ISIS3 pipelines. Global coverage of CTX stereo pair derived DEMs could then be analyzed by the RetinaNet CNN to detect and catalog cirques and other geomorphic features on Mars.

2.8 Contributions

Conceptualization, J.M.W. and L.A.S.; methodology, J.M.W. and L.A.S.; software, J.M.W.; formal analysis, J.M.W., L.A.S.; investigation, J.M.W., L.A.S.; resources, L.A.S.; data curation, J.M.W.; writing—original draft preparation, J.M.W. and L.A.S.; writing—review and editing, J.M.W., L.A.S.; visualization, J.M.W., L.A.S.; supervision, L.A.S.; project administration, L.A.S.; funding acquisition, L.A.S. All authors have read and agreed to the published version of the manuscript.

2.9 Appendix

2.9.1 Mosaicking CTX DEMs

Mosaicking DEMs are important in order to preserve DEM coverage of possible cirque forms that otherwise are only partially covered by a given DEM. To create a mosaic in ArcGIS Pro 2.9.0 we first created an empty raster with Data Management Tools > Raster> Create Raster Dataset (file extension (.tif) cell size (32), Pixel type (32_BIT_Unsigned) and Spatial Reference Properties (Sinusoidal_Mars)). Then under ArcGIS Pro 2.9.0 tools Data Management Tools > Raster> Mosaic tools the two or more DEMs are selected in the Input Rasters dialog box. The target raster was set to the previously created empty raster set. Ignore back- ground value and NoData value dialog boxes were selected as zero (0). The result is a DEM mosaic ready to be used for CNN cirque detection.

2.9.2 RetinaNet Training

The user can choose to freeze or unfreeze the backbone in these large-scale prebuilt object detection, key-point detection, segmentation, and captioning datasets. Freezing the backbone allows the user to keep these initial weights stable throughout training or, as in our case, allow the model to alter these initial weights as it optimizes (unfreezing). In our work this was applicable due to the existing robust training data set which allowed the model to fully optimize (increase trainable parame- ters) for image classification. Since the model's backbone was left unfrozen in this project, the number of trainable parameters increased from 1.2 × 107 to 3.6 × 107.

The Mean Average Precision (mAP) is a popular metric used in object detection classification and localization. ‘Classification’ is the object you are trying to identify, such as if a

user was interested in finding an image of a cat, the classification in the identified image would be a cat. ‘Localization’ is the spatial location in the image where the classification is, such as the bounding box around an object, or in our work the bounding box around a potential cirque. The measure of how accurate the model's predictions are, or the percentage of correct predictions is known as the precision. This is calculated by using the overlap area for the predicted localization (identification box) divided by the union (ground-truthed box plus localization box). Intersection over union (IoU) is used to determine Precision and Recall. Therefore, the user can select an IoU threshold and thus determine if the predictions are false positives (less than IoU threshold) or true positives (greater than IoU threshold). ‘Recall’ measures how well the algorithm identifies positive detections. Traditionally the average precision (AP) is defined as the area under the precision-recall curve (Fig. 4). It is important to note that the mAP is not the average of precision, rather mAP is the mean of AP values calculated over recall values - typically from 0 to 1 (Li et al., 2014; Yan et al., 2019; Zhang et al., 2019).

In terms of artificial neural networks, an ‘epoch’ refers to the algorithm operating in one cycle through the full training dataset. Usually training a neural network takes more than a few epochs. During training if model validation precision decreases for three epochs, the model then rolls back to a state prior to the precision decrease. In our model that occurred in the eighth epoch as epochs nine through twelve showed a decrease in precision (Fig. 4). ‘Regression loss’ is a scalar value that we attempt to minimize during our training of the model. The lower the regression loss, the closer our predictions are to the true labels (Fig. 4). Scuderi and Nagle-McNaughton et al. (2022) state: As the model learns from the training data, its performance on the validation data should increase as the model becomes better at identifying the target.

CNN learning rates represent the magnitude of updates to the net- work's weights after each optimization step (Tang et al., 2021; Scuderi and Nagle-McNaughton, 2022). Optimization is a method of augmenting the learning rate to reduce regression losses and obtain an optimal mAP. Like the RetinaNet model trained in the Scuderi and Nagle-McNaughton et al. (2022) study we settled on a learning rate of 1 × 10–5 after testing a range of different learning rates (1 × 10–3 to 1 × 10–8). All but the learning rate of 1 × 10–5 (Fig. 4) led to models that either rapidly overfit (i.e., after a single epoch) or that had lower performance metrics such as lower mean average precision (mAP). Training took 20 epochs with a batch size of four images held in memory for parallel training.

The user can change the CL score threshold during optimization in order to cull out initial false positives found during the training validation and find where there is room for further training (Scuderi and Nagle-McNaughton, 2022). Typically, the CL score is manually set to 0.20 to 0.80, however, it is important to note that this is highly dependent on the parameter that you are trying to identify. Since our study involved assigning the CL score during training and validation for terrestrial cirque forms, we did not change the CL score for the martian analysis to make a direct planetary comparison. Therefore, we have analyzed the martian study area with 1) No changes to the terrestrially assigned CL score to better compare the performance of the algorithm and to highlight differences between the two datasets, and 2) identifi- cation of false positives and false negatives along with analysis of what appears to be identifications that align well with terrestrial results (Fig. 3).

RetinaNet Training Script: https://github.com/ploppers505/Ma rsCirqueNet/blob/main/Retinanet-checkpoint.ipynb.

2.9.3 DEM Clipping

DEM clipping consisted of two stages: 1) primary 50 × 50 km DEM clipping and 2) secondary 1280 × 1280 pixel tile clipping necessary for CNN analysis. Primary clipping was done manually using the clipping tool in ArcGIS Pro 2.9.0 in the study area. To preserve optimal computer processing time, the primary DEM clip was limited to a maximum of 50 × 50 km, otherwise computer processing lag and errors occurred. The secondary tile clipping processing was performed by a custom python script using the Geospatial Data Abstraction Library (GDAL) in ArcGIS Pro (ESRI, 2021). This was followed by a custom script that loaded and ran the necessary modules used to convert the 50 × 50 km DEM clip raster data into 1280 × 1280 pixels tiles. The modules are the GDAL translate utility, glob (short for global) that is used to return all file paths and from osgeo we import gdal and from PIL we imported Image. The custom script then resamples the 1280 × 1280 pixel tiles and returns 256 × 256 pixel tiles and saves as a .tif file and a .png file. It normalized the DEM clip data using the uint8 data type so that the array was defined as a linear spread from 0 to 255. The 256 × 256 pixel tiles resolution and normalization were necessary to match the terrestrial training tile set as defined in the Scuderi and Nagle-McNaughton et al. (2022) study. This was required in order to allow the use of RetinaNet training set tile clips for martian cirque identification.

2.9.4 RetinaNet Evaluation

An augmented off-the-shelf RetinaNet algorithm script loads the necessary modules. The first module block imports Keras then keras- retinanet and keras-retinanet.utls, keras_retinanet.utils.visualization, keras_retinanet.utils.colors keras_retinanet.utils.gpu, import

‘setup_gpu’. This establishes the computer graphics processing unit (GPU) as the main processor. The next module block loads the previously trained RetinaNet inference model (1e -5) and resnet50 backbone and assigns the label to name as ‘Cirque’. Finally, the script runs the RetinaNet detection on the tiles in the designated local folder on a tile and runs through the tiles iteratively. It creates cirque identification bounding boxes and associated scores, labels, and boxes and is saved as a .csv file. Another custom script then loads the .csv file with all the aggregated tile data (boxes, scores, labels). This custom python script imports the following modules: rasterio from rasterio.features import ‘shapes’, numpy as ‘np’, geopandas as ‘gp’, pandas as ‘pd’, matplotlib. pyplot as ‘plt’. The custom script creates a shapefile of the cirque bounding boxes with scores, labels and files in the shapefile attributes.

This shapefile is then loaded into ArcGIS Pro 2.9.0 for further analysis (ESRI, 2021).

Evaluation Script: https://github.com/ploppers505/MarsCirqueNet/blob/main/evaluation.ipynb.

REFERENCES

Banks, M.E., McEwen, A.S., Kargel, J.S., Baker, V.R., Strom, R.G., Mellon, M.T., Gulick, V.C., Keszthelyi, L., Herkenhoff, K.E., Pelletier, J.D., 2008. High Resolution Imaging Science Experiment (HiRISE) observations of glacial and periglacial morphologies in the circum-Argyre Planitia highlands. Mars. *Journal of Geophysical Research: Planets* 113 (E12).

Malin, M.C., Bell III, J.F., Cantor, B.A., Caplinger, M.A., Calvin, W.M., Clancy, R.T., Edgett, K.S., Edwards, L., Haberle, R.M., James, P.B., 2007. Context camera investigation on board the Mars Reconnaissance Orbiter. *Journal of Geophysical Research: Planets* 112 (E5).

Beyer, R.A., Alexandrov, O., McMichael, S., 2018. The Ames Stereo Pipeline: NASA's open source software for deriving and processing terrain data. *Earth and Space Science* 5 (9), 537–548.

Bickel, V.T., Lanaras, C., Manconi, A., Loew, S., Mall, U., 2018. Automated detection of lunar rockfalls using a convolutional neural network. IEEE Trans. *Geosci. Remote Sens.* 57 (6), 3501–3511.

Brardinoni, F., Hassan, M.A., 2006. Glacial erosion, evolution of river long profiles, and the organization of process domains in mountain drainage basins of coastal British Columbia. *Journal of Geophysical Research: Earth Surface* 111 (F1).

Carr, M.H., 1995. The Martian drainage system and the origin of valley networks and fretted channels. *Journal of Geophysical Research: Planets* 100 (E4), 7479–7507.

Carr, M.H., 2001. Mars Global Surveyor observations of Martian fretted terrain. *Journal of Geophysical Research: Planets* 106 (E10), 23571–23593.

Christensen, P., Engle, E., Anwar, S., Dickenshied, S., Noss, D., Gorelick, N., Weiss- Malik, M., 2009. JMARS-a Planetary GIS. AGU Fall Meeting Abstracts.

Clark, J.M., Lewis, W., 1951. Rotational movement in cirque and valley glaciers. *The Journal of Geology* 59 (6), 546–566.

Colaprete, A., Jakosky, B.M., 1998. Ice flow and rock glaciers on Mars. *Journal of Geophysical Research: Planets* 103 (E3), 5897–5909. https://doi.org/10.1029/ 97je03371.

Conway, S.J., Butcher, F.E., de Haas, T., Deijns, A.A., Grindrod, P.M., Davis, J.M., 2018. Glacial and gully erosion on Mars: a terrestrial perspective. *Geomorphology* 318, 26–57.

Crest, Y., Delmas, M., Braucher, R., Gunnell, Y., Calvet, M., Team, A., 2017. Cirques have growth spurts during deglacial and interglacial periods: evidence from 10Be and 26Al nuclide inventories in the central and eastern Pyrenees. *Geomorphology* 278, 60–77.

Davila, A.F., Fair´en, A.G., Stokes, C.R., Platz, T., Rodriguez, A.P., Lacelle, D., Dohm, J., Pollard, W., 2013. Evidence for Hesperian glaciation along the martian dichotomy boundary. *Geology* 41 (7), 755–758. https://doi.org/10.1130/g34201.1.

Day, M., Anderson, W., Kocurek, G., Mohrig, D., 2016. Carving intracrater layered deposits with wind on Mars. *Geophys. Res. Lett*. 43 (6), 2473–2479.

DeLatte, D.M., Crites, S.T., Guttenberg, N., Tasker, E.J., Yairi, T., 2019. Segmentation convolutional neural networks for automatic crater detection on mars. *IEEE Journal of Selected Topics in Applied Earth Observations and Remote Sensing* 12 (8), 2944–2957.

Dickson, J.L., Head, J.W., Marchant, D.R., 2008. Late Amazonian glaciation at the dichotomy boundary on Mars: evidence for glacial thickness maxima and multiple glacial phases. *Geology* 36 (5). https://doi.org/10.1130/g24382a.1.

Dromart, G., Le Deit, L., Rapin, W., Gasnault, O., Le Mou´elic, S., Quantin-Nataf, C., Mangold, N., Rubin, D., Lasue, J., Maurice, S., Newsom, H.E., Pinet, P., Scuderi, L., Wiens, R.C., 2021. Deposition and erosion of a Light-Toned Yardang-forming unit of Mt Sharp, Gale crater. Mars. *Earth and Planetary Science Letters* 554. https://doi.org/10.1016/j.epsl.2020.116681.

ESRI, 2021. ArcMap Release 10.8.1. and, ArcGIS Pro Release 2.9.0. Environmental Systems Research Institute, Redlands, CA.

Evans, I.S., 1977. World-wide variations in the direction and concentration of cirque and glacier aspects. Geografiska Annaler: *Series A, Physical Geography* 59 (3–4),

151–175.

Evans, I., 2007. Glacial landforms, erosional features: major scale forms. *Encyclopedia of Quaternary Science* 1, 838–852.

Evans, I.S., 2010. Allometory, scaling and scale-specificity of cirques, landslides and other landforms (特集 日本地形学連合創立 30 周年記念). 地形= *Transactions, Japanese Geomorphological Union* 31 (2), 133–153.

Evans, I.S., Cox, N., 1974. Geomorphometry and the operational definition of cirques. *Area* 150–153.

Evans, I.S., Cox, N.J., 1995. The form of glacial cirques in the English Lake District. Cumbria. *Zeitschrift für Geomorphologie* 175–202.

Evans, I.S., Cox, N.J., 2005. Global variations of local asymmetry in glacier altitude: separation of north–south and east–west components. J. *Glaciol.* 51 (174), 469–482.

Farr, T.G., Rosen, P.A., Caro, E., Crippen, R., Duren, R., Hensley, S., Kobrick, M., Paller, M., Rodriguez, E., Roth, L., 2007. The shuttle radar topography mission. Rev. *Geophys*. 45 (2).

Forget, F., Haberle, R., Montmessin, F., Levrard, B., Head, J., 2006. Formation of glaciers on Mars by atmospheric precipitation at high obliquity. *Science* 311 (5759),

368–371.

Gaiser, H. and M. de Vries, 2022, Accessed. Keras-Retinanet.

Glassmeier, K.-H., 2020. Solar system exploration via comparative planetology. *Nat. Commun.* 11 (1), 1–4.

Google Earth 7.3.6. (07/16/2016), 2016. Google Earth image of a Sierra Nevada, CA Cirque alcove. In: Coordinates: 36◦ 29′55.19″N, 118◦ 13′51.78″W, Eye altitude: 18,092 ft.

Head, J.W., Marchant, D.R., 2003. Cold-based mountain glaciers on Mars: western Arsia Mons. *Geology* 31 (7), 641–644.

Head, J., Marchant, D., 2009. Inventory of ice-related deposits on Mars: evidence for burial and long-term sequestration of ice in non-polar regions and implications for the water budget and climate evolution. In: *40th Annual Lunar and Planetary Science Conference.*

Head, J.W., Marchant, D.R., Ghatan, G.J., 2004. Glacial deposits on the rim of a Hesperian-Amazonian outflow channel source trough: Mangala Valles. Mars. *Geophysical Research Letters* 31 (10).

Head, J., Neukum, G., Jaumann, R., Hiesinger, H., Hauber, E., Carr, M., Masson, P., Foing, B., Hoffmann, H., Kreslavsky, M., 2005. Tropical to mid-latitude snow and ice accumulation, flow and glaciation on Mars. *Nature* 434 (7031), 346–351.

Head, J.W., Marchant, D.R., Agnew, M.C., Fassett, C.I., Kreslavsky, M.A., 2006. Extensive valley glacier deposits in the northern mid-latitudes of Mars: evidence for late Amazonian obliquity-driven climate change. *Earth Planet. Sci. Lett.* 241 (3–4), 663–671.

Head, J.W., Marchant, D.R., Dickson, J.L., Kress, A.M., Baker, D.M., 2010. Northern mid-latitude glaciation in the Late Amazonian period of Mars: criteria for the recognition of debris-covered glacier and valley glacier landsystem deposits. *Earth Planet. Sci.* Lett. 294 (3–4), 306–320. https://doi.org/10.1016/j.epsl.2009.06.041.

Hepburn, A.J., Holt, T., Hubbard, B., Ng, F., 2019. Creating HiRISE digital elevation models for Mars using the open-source Ames Stereo Pipeline. *Geoscientific Instrumentation, Methods and Data Systems* 8 (2), 293–313.

Hsu, C.-Y., Li, W., Wang, S., 2021. Knowledge-driven GeoAI: integrating spatial knowledge into multi-scale deep learning for Mars Crater detection. Remote Sens. 13 (11), 2116.

Hubbard, B., Souness, C., Brough, S., 2014. Glacier-like forms on Mars. *The Cryosphere* 8 (6), 2047–2061. https://doi.org/10.5194/tc-8-2047-2014.

Lee, C., 2019. Automated crater detection on Mars using deep learning. *Planetary and Space Science* 170, 16–28.

Li, Y., Zhao, Z., 2022. AutoCirque: an automated method to delineate glacial cirque outlines from digital elevation models. *Geomorphology* 398, 108059.

Li, K., Huang, Z., Cheng, Y.-C., Lee, C.-H., 2014. A maximal figure-of-merit learning approach to maximizing mean average precision with deep neural network based classifiers. In: 2014 *IEEE International Conference on Acoustics. Signal Processing (ICASSP), Speech and.*

Li, J., Zhang, L., Wu, Z., Ling, Z., Cao, X., Guo, K., Yan, F., 2020. Autonomous Martian rock image classification based on transfer deep learning methods. *Earth Sci. Inf.* 13 (3), 951–963.

Lin, T.-Y., Maire, M., Belongie, S., Hays, J., Perona, P., Ramanan, D., Dolla´r, P., Zitnick, C.L., 2014. Microsoft Coco: Common Objects in Context*. European conference on computer vision.*

Lin, T.-Y., Dolla´r, P., Girshick, R., He, K., Hariharan, B., Belongie, S., 2017. Feature pyramid networks for object detection. In: *Proceedings of the IEEE Conference on Computer Vision and Pattern Recognition.*

Lo´pez-Moreno, J., Nogu´es-Bravo, D., Chueca-Cía, J., Juli´an-Andr´es, A., 2006. Change of topographic control on the extent of cirque glaciers since the Little Ice Age. *Geophys. Res. Lett.* 33 (24).

Lucchitta, B.K., 1984. Ice and debris in the fretted terrain, Mars. Journal of Geophysical Research: *Solid Earth* 89 (S02), B409–B418.

Malin, M.C., Edgett, K.S., 2000. Sedimentary rocks of early Mars. *Science* 290 (5498), 1927–1937.

Marinova, M.M., Aharonson, O., Asphaug, E., 2008. Mega-impact formation of the Mars hemispheric dichotomy. *Nature* 453 (7199), 1216–1219.

Melosh, H.J., 2011. Planetary surface processes, Vol. 13. Cambridge University Press. Morgan, G.A., Putzig, N.E., Perry, M.R., Sizemore, H.G., Bramson, A.M., Petersen, E.I., Bain, Z.M., Baker, D.M., Mastrogiuseppe, M., Hoover, R.H., 2021. Availability of subsurface water-ice resources in the northern mid-latitudes of Mars. *Nature Astronomy* 5 (3), 230–236.

Murray, J.B., Muller, J.-P., Neukum, G., Werner, S.C., van Gasselt, S., Hauber, E., Markiewicz, W.J., Head, J.W., Foing, B.H., Page, D., 2005. Evidence from the Mars Express High Resolution Stereo Camera for a frozen sea close to Mars' equator. *Nature* 434 (7031), 352–356.

Nagle-McNaughton, T., McClanahan, T., Scuderi, L., 2020. Planet: a neural network for detecting transverse aeolian ridges on mars. *Remote Sens*. 12 (21), 3607.

Nagle-McNaughton, T.P., Scuderi, L.A., Erickson, N., 2022. Squeezing data from a rock: machine learning for martian science. *Geosciences* 12 (6), 248.

Neukum, G., Jaumann, R., Hoffmann, H., Hauber, E., Head, J., Basilevsky, A., Ivanov, B., Werner, S., Van Gasselt, S., Murray, J., 2004. Recent and episodic volcanic and glacial activity on Mars revealed by the high resolution stereo camera. *Nature* 432 (7020), 971–979.

Olyphant, G.A., 1981. Allometry and cirque evolution. Geol. Soc. Am. Bull. 92 (9), 679–685.

Osserman, R., 1978. The isoperimetric inequality. Bull. Am. *Math. Soc*. 84 (6), 1182–1238.

Palacios, D., Rodríguez-Mena, M., Ferna´ndez-Ferna´ndez, J.M., Schimmelpfennig, I., Tanarro, L.M., Zamorano, J.J., Andr´es, N., Úbeda, J., Sæmundsson, Þ., Brynjo´lfsson, S., 2021. Reversible glacial-periglacial transition in response to climate changes and paraglacial dynamics: a case study from H´eðinsdalsjo¨kull (northern Iceland). *Geomorphology* 388, 107787.

Palafox, L., Alvarez, A., Hamilton, C., 2015. Automated detection of impact craters and volcanic rootless cones in mars satellite imagery using convolutional neural networks and support vector machines. In: *46th Lunar and Planetary Science Conference.*

Pan, S.J., Yang, Q., 2009. A survey on transfer learning. IEEE Trans. Knowl. *Data Eng*. 22 (10), 1345–1359.

Patterson, E., 1984. A mathematical model for perched block formation. *J. Glaciol*. 30 (106), 296–301.

Pelletier, J.D., Comeau, D., Kargel, J., 2010. Controls of glacial valley spacing on Earth and Mars. *Geomorphology* 116 (1–2), 189–201.

Ramy El-Maarry, M., Harrington, E., 2022. The Glacial Landscape in Moreux Crater Versus a Mountain Glacier in Argyre. A comparative analysis. *European Planetary Science Congress, Mars.*

Richardson, C., Holmlund, P., 1996. Glacial cirque formation in northern Scandinavia. *Ann. Glaciol.* 22, 102–106.

Scanlon, K., Head, J., Marchant, D., 2015. Remnant Buried Ice in the Arsia Mons fan- Shaped Deposit. Mars, *Lunar and Planetary Science Conference*.

Schon, S.C., Head, J.W., Fassett, C.I., 2012. An overfilled lacustrine system and progradational delta in Jezero crater, Mars: implications for Noachian climate. *Planetary and Space Science 67* (1), 28–45.

Scuderi, L.A., Nagle-McNaughton, T., 2022. Automated neural network identification of cirques. Phys. *Geogr. 43* (1), 24–51.

Sharp, R.P., 1973. Mars: Fretted and chaotic terrains. *J. Geophys. Res.* 78 (20), 4073–4083.

Shean, D.E., Head III, J.W., Fastook, J.L., Marchant, D.R., 2007. Recent glaciation at high elevations on Arsia Mons, Mars: implications for the formation and evolution of large tropical mountain glaciers. Journal of Geophysical Research: *Planets 112 (*E3).

Soare, R., Williams, J.-P., Hepburn, A., Butcher, F., 2022. A billion or more years of possible periglacial/glacial cycling in Protonilus Mensae, Mars. *Icarus* 115115.

Souness, C.J., Hubbard, B., 2013. An alternative interpretation of late Amazonian ice flow: Protonilus Mensae. Mars. *Icarus 225* (1), 495–505.

Squyres, S.W., 1978. Martian fretted terrain: Flow of erosional debris. *Icarus 34* (3), 600–613.

Squyres, S.W., 1979. The distribution of lobate debris aprons and similar flows on Mars. Journal of Geophysical Research: *Solid Earth 84* (B14), 8087–8096.

Squyres, S.W., Clifford, S., Kuzmin, R., Zimbelman, J.R., Costard, F., 1992. Ice in the Martian Megaregolith. Mars.

Tang, S., Zhu, Y., Yuan, S., 2021. An improved convolutional neural network with an adaptable learning rate towards multi-signal fault diagnosis of hydraulic piston pump. Adv. *Eng. Inform.* 50, 101406.

Torrey, L., Shavlik, J., 2010. Transfer learning. In: Handbook of research on machine learning applications and trends: algorithms, methods, and techniques. *IGI global,* pp. 242–264.

USGS, 2020. Shuttle Radar Topography Mission 1 Arc-Second Global U.S. *Geological Survey SRTM Data Release.*

Wagstaff, K., Lu, Y., Stanboli, A., Grimes, K., Gowda, T., Padams, J., 2018. Deep Mars: CNN Classification of Mars Imagery for the PDS Imaging Atlas. *Proceedings of the AAAI Conference on Artificial Intelligence.*

Williams, J.P., van der Bogert, C.H., Pathare, A.V., Michael, G.G., Kirchoff, M.R., Hiesinger, H., 2018. Dating very young planetary surfaces from crater statistics: a review of issues and challenges. Meteorit. *Planet. Sci. 53* (4), 554–582.

Williams, J., Day, M., Chojnacki, M., Rice, M., 2020. Scarp orientation in regions of active aeolian erosion on Mars. *Icarus* 335, 113384.

Williams, J.M., Scuderi, L.A., Newsom, H.E., 2022. Numerical analysis of putative rock glaciers on Mount Sharp, Gale Crater. Mars. *Remote Sensing 14* (8), 1887.

Yan, J., Wang, H., Yan, M., Diao, W., Sun, X., Li, H., 2019. IoU-adaptive deformable R- CNN: make full use of IoU for multi-class object detection in remote sensing imagery. *Remote Sens*. *11* (3), 286.

Zhang, H., Chang, H., Ma, B., Shan, S., Chen, X., 2019. Cascade retinanet: maintaining consistency for single-stage object detection. *arXiv Preprint* 1–10. arXiv:1907.06881.

Zuber, M.T., Solomon, S.C., Phillips, R.J., Smith, D.E., Tyler, G.L., Aharonson, O., Balmino, G., Banerdt, W.B., Head, J.W., Johnson, C.L., 2000. Internal structure and early thermal evolution of Mars from Mars Global Surveyor topography and gravity.
Science 287 (5459), 1788–1793.

CHAPTER THREE

Evaluating possible glacial valley modification by using a new U-shaped valley analysis in the Martian tropics near Gale crater

Citation:

Williams, J. M., Scuderi, L. A., Zimmer, P. D., Newsom, H.E. (2024). Evaluating possible glacial valley modification by using a new U-shaped valley analysis in the Martian tropics near Gale crater. *Geomorphology*. (In publication).

Abstract

Growing evidence supports the case for glacial processes within the equatorial regions of Mars. However, few examples of modeling or numerical analysis exist to support this hypothesis. Here we use an automated method on valleys near Gale crater to extract morphometric data and analyze the formative processes responsible for their current expression. The V-index we utilize is a new robust method and is an alternative to traditional parabolic curve fits because it can more easily interpret irregular valley cross sections and thus aid in distinguishing between glacial and nonglacial forms. We use this method along with the power law and quadratic curve fit on extracted valley cross sections along a 2,300 km extent of the Martian tropics near Gale crater. Both the V-index and power b fit values suggest that the majority of the valleys are U-shaped and possibly created through glacial erosive processes. Further, V-index and power law b values plotted against elevation show a positive trend with higher V-index (glaciated) values associated with higher elevation. This suggests that an equilibrium ELA existed at the time of valley formation. The timing of the formation of these U-shaped valleys is poorly defined. Equatorial glaciers that produced these and other related forms could be ancient with a relative timing of their creation as old as the Hesperian to Amazonian transition (~3 Ga) or they could be tied to more near term equatorward migration of the Martian cryosphere during more recent periods of high obliquity oscillations.

3.1 Introduction

Modern Mars is characterized by a cold hyperarid environment and a tenuous atmosphere. Currently surface water ice in the equatorial region is unstable and hence there is little evidence indicating current glaciation in this region (Baker, 2001; Bibring et al., 2006; Morgan et al., 2011; Head & Marchant, 2014) However, in the past, Martian obliquity variations may have produced conditions that allowed significant water ice to form in the equatorial zone (Head et al., 2006b; Madeleine et al., 2009; Scanlon et al., 2015).

Past glaciation on Earth is evidenced in the geomorphic forms associated with glacial erosion and deposition, such as cirques, aretes, roches moutonées, moraines, eskers, plucked terrain and U-shaped valleys. The presence of these forms has been used to reconstruct the terrestrial climatic history of many previously glaciated regions (Montgomery, 2002; James, 2003; Glasser & Bennett, 2004). While similar forms have been documented on Mars (Gulick, 2001; Williams & Phillips, 2001; Kereszturi, 2005; Banks et al., 2008; Pelletier et al., 2010; Bouquety et al., 2019; Cassanelli & Head, 2019; Buffo et al., 2022) most of these studies have focused on non-equatorial regions. Identification and quantification of glacial forms in the Martian equatorial region is the first step in understanding the links between obliquity oscillation driven Martian climate change (Holo et al., 2018; Williams et al., 2018; Emmett et al., 2020) and potential landscape modification produced by glaciation.

Here, using a semi-automated approach (Zimmer & Gabet, 2018), we analyzed 919 valley form cross section profiles in 28 valleys along the equatorial portion of the fretted terrain along a 2,300 km section of the dichotomy boundary east of Gale crater (Fig 1). We conducted this research to evaluate the hypothesis that extensive glacial processes may have been responsible for the modern morphometric expression with the equatorial zone of Mars.

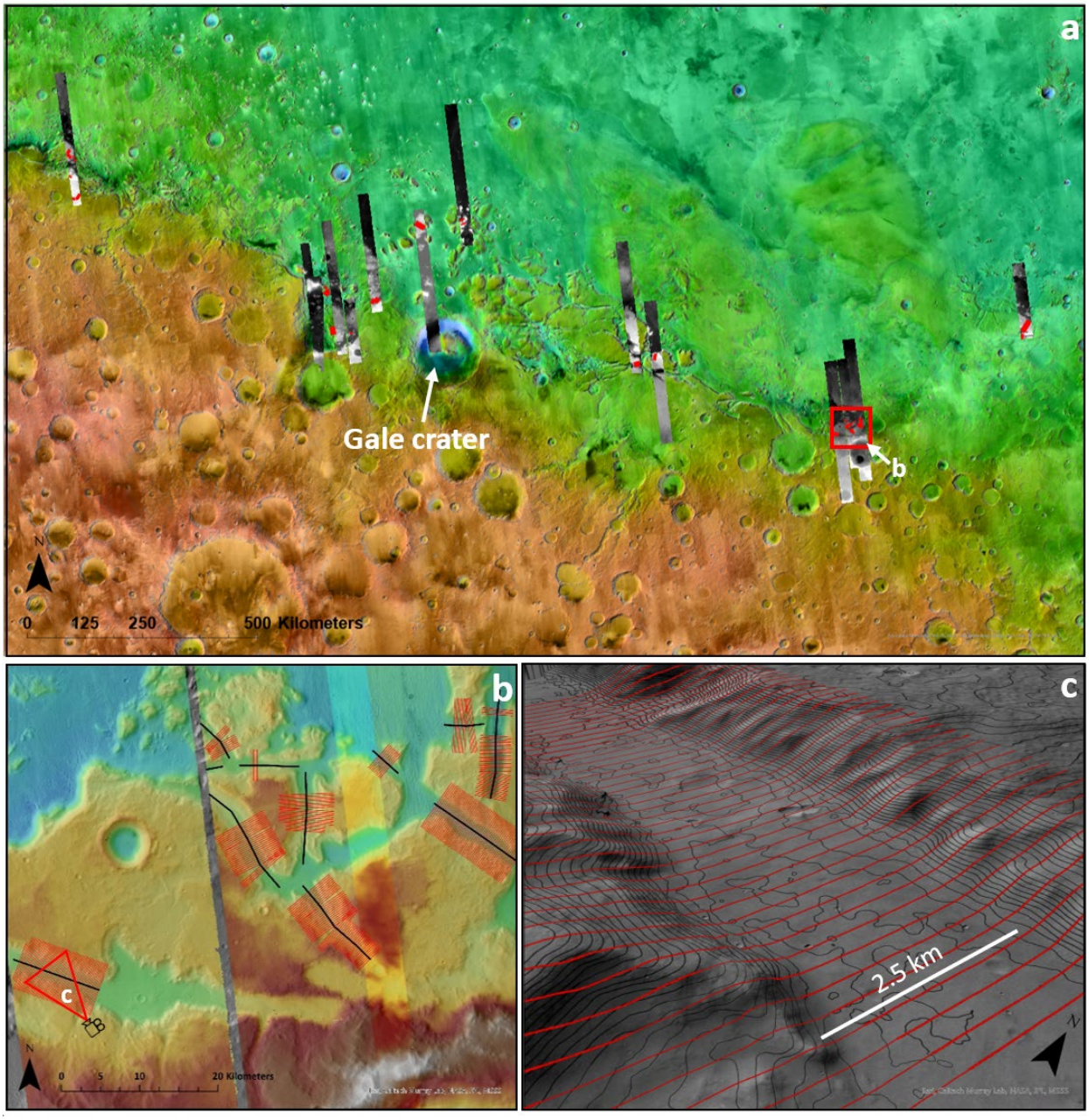

Figure 1. Study area context image. a) DEM footprints with valley cross-sections (red) along a 2,300 km section of the Martian dichotomy boundary. Gale crater is located in the center. Red box marks the location of (b). b) Example of valley axis (black lines) locations created in ArcGIS Pro. Valley cross sections (red) are (best fit) 5, 7 and 10 km-long lines generated perpendicular to the axis every 250 m. Camera icon marks the location of the scene image in c. c) ArcGIS Pro Scene generated image depicting mapped valley with cross sections (red).

Contour lines 20 m intervals. Image credit: NASA/JPL-Caltech/ESA/DLR/FU Berlin; Google Mars

3.1.1 Scientific Background

Cryospheric ice eroding the landscape through glacial and periglacial processes is a major geomorphic agent capable of significant modification of planetary surfaces (Hobbs et al., 2016; Palacios et al., 2021). A wide range of evidence from the Martian high to mid-latitudes supports the hypothesis of significant glacial surficial processes early in Mars history (Head & Marchant, 2003; Head et al., 2005; Shean, 2005; Dickson et al., 2008; Head et al., 2010; Scanlon et al., 2015) as well as the presence of substantial past surface and subsurface water ice (Head et al., 2008; Melosh, 2011; Schorghofer & Forget, 2012; Carr & Head, 2015). Investigations at mid- to high latitudes on Mars have also shown evidence of flowing ice often forming integrated patterns, representing mass transportation within U-shaped valleys that appears to be initiated in discrete cirque-like alcoves (Neukum et al., 2004; Dickson et al., 2008; Head & Marchant, 2009; Hubbard et al., 2011; Souness & Hubbard, 2013; Hubbard et al., 2014; Williams et al., 2023a).

It has long been thought that Mars has maintained a hyperarid cold surface with a tenuous atmosphere for most of the Amazonian period (3.0 Ga to present) with aeolian processes currently the dominant geomorphic agent. The modern cryosphere on Mars is believed to be dormant or relic at most non-polar latitudes (Head et al., 2006a; Banks et al., 2008; Dickson et al., 2008; Scanlon et al., 2015; Conway et al., 2018; Hepburn et al., 2019; Morgan et al., 2021). However, there is growing evidence supporting prior glaciation in the equatorial region (Head et al., 2006b; Davila et al., 2013; Williams et al., 2023a). These studies tentatively suggest a formation age for equatorial glaciers at the Hesperian/Amazonian boundary (2.9-3.0 Ga) (Davila

et al., 2013; Rivera-Hernández & Palucis, 2019; Putnam & Palucis, 2021). However, the timing of these glacial/periglacial processes as well as the areal distribution of relict forms that delimit ice extent at lower latitudes remains poorly understood.

Recent studies suggest that stable subsurface ice may currently exist in subtropical zones from 20 to 35 degrees latitude in each hemisphere (Bandfield, 2007; Dundas et al., 2023; Lange et al., 2023; Putzig et al., 2023). As well, current subsurface ice at lower latitudes closer to the Martian equator has recently been documented (Lange et al., 2023; Ma et al., 2023; Qin et al., 2023). Ground observations of features potentially linked to past glaciation are unfeasible now and in the near future. Instead, studies assessing the timing of glaciation use morphometric analysis from remote sensed imagery, Digital Elevation Models and manual extraction of morphometric information and form indices from these sources.

3.1.2 Valley Cross-sectional Form

U-shaped valleys with symmetrical parabolic cross-sections and stepped longitudinal profiles are characteristic of terrestrial glacial valley forms (Hirano & Aniya, 1988; Harbor, 1992; Montgomery, 2002).To assess and contrast markers of prior glaciation and/or fluvial activity, valley cross-sections traditionally have been fit to a parabolic curve using the profile power form law (Svensson, 1959; Graf, 1970; Coles, 2014; Faillettaz et al., 2016);

$$y = a\,x^{b} \tag{1}$$

where, x and y represent horizontal and vertical distance from the valley low point respectively, and a and b are constants determined by a least-squares fit to a logarithmic transformation of section coordinates (Graf, 1970; Harbor, 1995). Valleys that have undergone glacial modification

have **b** values between 1.5-2.5, while valleys with little to no glacial modification have **b** values close to 1.0 (Graf, 1970; Banks et al., 2008; Zimmer & Gabet, 2018).

Alternatively, the fit is estimated using a quadratic equation of the form (Wheeler, 1984; James, 1996; Carr et al., 2014; Fowler & Chapwanya, 2014);

$$y = a + bx + cx^2 \quad (2)$$

where, a, b, and c are coefficients; with c directly controlling valley shape. Here larger values of c reflect a narrower valley floor and therefore a more V-shaped fluvial cross section and smaller c values indicate the broader valley floor typical of a glacial U-shaped cross section.

3.1.3 The V-index

The V-index (Zimmer & Gabet, 2018) compares valley cross-sectional area to that of an ideal V-shaped cross section. The V-index (v) is calculated by comparing valley cross-sectional area between the valley bottom and a specified height above the valley floor to that of an ideal V-shaped cross section with the same height and width as the subject cross section using;

$$v = (A_x/A_v)\text{-}1) \quad (3)$$

where, A_x is the valley cross-sectional area between the valley bottom and a specified height above the valley floor, and A_v is the area of an ideal V-shaped cross section with the same height and width as the subject cross section. A perfect V-shaped valley has a $v = 0$, while U-shaped valleys are defined by $v > 0$ and convex valleys are defined by v-index < 0 (Zimmer & Gabet, 2018). This approach is preferable in terrains that do not exhibit smooth functions due to irregularities in valley wall side slopes.

The V-index differs from traditional power form law and quadratic fit approaches and represents a modification of earlier form measures such as the valley depth to width form ratio (Graf, 1970);

$$F_R = D/W_T \quad (4)$$

where, F_R is the ratio of valley depth (D) to valley top width (W_T)

Similar percentile comparisons of width at various valley depths have been used to discriminate between V-shaped and U-shaped flat-floored valleys. One such measures is the Valley floor width-to-height ratio (V_f) (Bull & McFadden, 2020);

$$V_f = (4)\ 2\ V_{fw}/(E_{ld} + E_{rd} - 2E_{sc}) \quad (5)$$

where, V_{fw} is the width of the valley floor, E_{ld} and E_{rd} are elevations of the left and right valley divides, respectively, and E_{sc} is the elevation of the valley floor.

The V-index is superior to these methods since it avoids producing similar form ratio values for different shaped valleys (Zimmer & Gabet, 2018). As well, it can be used for non-smooth profiles that are more representative of the "real" terrain encountered on both Earth and Mars.

3.1.4 The Study Area

3.1.4.1 The Fretted Terrain and Dichotomy Boundary

Much of the dichotomy boundary is associated with fretted terrain - typically defined by massifs with highly planimetric irregular configurations dissected by valleys (Sharp, 1973). Fretted terrain has been hypothesized to be in situ deformation due to subsurface ground ice and ice rich flow/creep typically associated with glacier processes such as cirque and alpine-like valley glacier erosion (Sharp, 1973; Squyres, 1978, 1979; Lucchitta, 1984; Squyres et al., 1992; Carr, 2001; Irwin III et al., 2004; Davila et al., 2013). Studies have suggested that this terrain

was formed by glacial modification such as basal glacier scouring (Lucchitta, 1984; Head et al., 2006b; Davila et al., 2013) which would be only possible through wet based glaciation. However, some studies suggest the fretted terrain was formed by fluvial erosion that was subsequently modified by mass-wasting processes (Carr, 2001), by the flow of erosional debris (Squyres, 1978), or as the result of structural fracturing and subsequent erosion (Morgan et al., 2022).

Our study was conducted along the dichotomy boundary near the Martian equator from approximately 1,000 km west to ~1,300 km east of Gale Crater (Fig. 1). The 2,300 km^2 study area was selected since it captures valley features that visually range from V to U-shaped. Additionally, excellent context camera (CTX) stereo coverage across the study area allowed production of DEMs critical for the valley morphometric extraction.

3.2 Methods

We utilized custom Python and ESRI ArcMap scripts based on methods developed by Zimmer and Gabet (2018) to analyze Martian valley cross-sectional forms from Digital Elevation Models (DEM's). This approach is applicable across a wide range of scales ranging from individual drainage reaches to entire drainage networks. This approach can rapidly produce statistically significant numbers of cross-section profiles for valley form analysis (Zimmer & Gabet, 2018).

3.2.1 Digital Elevation Model (DEM) production and analysis

All images used in this study were sourced from NASA's Planetary Data System (PDS) archive and are freely available on that site. We used 6 m/pixel spatial resolution Context

Camera (CTX) images acquired by the CTX camera onboard the NASA Mars Reconnaissance Orbiter (MRO) spacecraft. The identified CTX images were accessed and downloaded via the Arizona State University (ASU) planet view website (https://viewer.mars.asu.edu/viewer/ctx) (Malin et al., 2007).

In order to produce high quality DEMs, we identified CTX stereo pairs using the Java Mission-planning and Analysis for Remote Sensing tool (JMARS) (Christensen et al., 2009) and when necessary, augmented the stereo coverage with data when available from Google Mars 7.3.4 (https://www.google.com/mars/). Using these programs, we identified and downloaded CTX stereo pairs from the ASU School of Earth and Space Exploration Image Explorer using the planetary database source Experiment Data Record (EDR).

We then applied the open-source NASA Aims Stereo Pipeline (ASP) to create ~18m/pixel resolution DEMs (Besse & Grotheer, 2021; Muller et al., 2021). DEMs were created using the USGS ISIS3 and NASA Ames Stereo Pipeline (ASP) (Beyer et al., 2018) derived from CTX stereo observations. Using the ASP pipeline, we produced overlapping DEMs derived from fifteen CTX stereo pairs) (See Supp. Table 1) with a resulting spatial resolution of ~18 m/pixel. Using the ArcGIS Pro 'Mosaic to New Raster' tool we then created a mosaic of the 25 DEMs for further processing.

The CTX stereo pair derived DEM production quality depends largely on the image capture angle. Suboptimal image capture angles sometimes create gaps in the original CTX image and therefore resulted in holes (null data) in the DEM and reduced overall quality. A workflow was defined to help mask or fill holes using the ArcGIS Pro 2.9.0 Focal Statistics Tool and a rectangular median 21x21 filter (ESRI, 2021). This approach successfully filled large DEM holes where neighboring elevations were similar. However, DEM locations displaying

substantial elevation differences relative to the elevations of neighboring features created less than desirable fill elevations. Initially we created over thirty DEMs within the study area using ASP, however several were rejected for further analysis due to artifacts and DEM holes or spikes that were not removed.

3.2.2 Extraction of center lines

Unlike the Zimmer and Gabet (2018) study, we were unable to use the ArcGIS Pro Spatial Analyst 'flow accumulation' tool approach to generate valley axis lines along the length of the valley trunk. Since the Martian surface is heavily cratered at our DEM production scale the creation of accurate flow networks is very difficult. This is a common issue with flow dynamic analysis on Mars and these DEM's typically exhibit artifacts and holes. Instead, polylines for each of the 28 valley axes were mapped in ArcGIS Pro (ESRI, 2023) with using heads-up vectorization. As well, CTX DEM coverage is discontinuous across the 2,300 km study area.

We used the 'Generate Transects Along Lines' tool in ArcGIS Pro 3.2.1 (ESRI, 2023) to create cross-section transects 5-10 km long and spaced every 250 m along the valley axis (Fig.1b&c). We then removed cross sections that extended over the DEM edge or featured null elevation values using the 'Select by Attributes' tool in ArcGIS Pro (ESRI, 2023). Ill-fitted cross sections that overlapped due to bends in the valley floor were also removed. The 'Stack Profile' tool in ArcGIS Pro 3D Analyst Tools was then used to generate equidistant points along the individual transects and CTX stereopair derived elevation values were attached to the valley cross-section points using the 'Extract Values to Points' tool in ArcGIS Pro (ESRI, 2023). Extracted elevation data was then exported in .CSV format for calculating morphometric values

for each cross-sectional profile (ESRI, 2023). The extracted morphometric data is then saved as a .CSV for v-index analysis.

3.2.3 Extraction of the V-index, Morphometric Measures and Statistical Analysis

We conducted our analysis using a partially automated method validated on over 27,000 cross sections extracted from glacial and non-glacial valleys in California's Sierra Nevada Mountains. This approach uses a custom script to isolate the central valley from each cross section and calculates various shape metrics (Zimmer & Gabet, 2018). This study adapted the original MATLAB script to a Python environment (Zimmer & Gabet, 2018) and used it to calculate quadratic curve fits, power form curve fits, and the V-index for each cross section at specified height above the valley bottom approximating the trim line associated with the highest elevation likely subjected to glacial processes. In this study, we analyzed 919 cross sections located within 28 valleys to statistically quantify the distribution of V-index values and along with additional morphometric measurements of candidate valleys to assess the likelihood that the profiles were indicative of glacially formed valleys.

3.3 Results

3.3.1 Metric Statistical Analysis

The Zimmer and Gabet (2018) study conducted a logistic regression analysis (LRA) within their Sierra Nevada valley study to determine the effectiveness of the metrics (V-index, Power Form Law, Quadratic Equation). The LRA is a multivariate statistical technique used to describe the relationship between independent predictor variables and concluded that the V-index and power-fitting had a high predictive accuracy of 68.1% and 67.6% respectively for the terrestrial

analogs. However, the quadratic fits were the lowest predictive accuracy of 58.4% (Zimmer & Gabet, 2018). We report the quadratic fits, however, due to the poor fit calculations we could not assign quadradic predictions of valley shape.

3.3.2 Valley Morphology

In this study, we analyzed 919 valley cross sections in 28 valleys. Truncated valley height was assessed for all valleys to be approximately 56% of that of the total valley relief. This appeared to be consistent throughout the Martian study area with some outliers. Based on this initial analysis, shape metrics were then calculated for the portion of the cross section below ~56% of total valley height, which corresponds to the average trim line elevation; this ensures that the analysis captures the portion of the valley most likely to be modified by glacial processes (see Zimmer and Gabet, 2018).

The average V-index for the entire study area was 0.30 with a 1σ of 0.16 (Table 1). The cross-sectional profile and other cross-sections associated with this valley indicate a symmetrical U-shaped parabola, suggesting modification by glacial processes. For this analysis, we used a V-index of 0.10 to be the cutoff point between V-shaped (fluvial) and U-shaped (glacial). However, it is important to note that there is variability with this assessment, with some U-shaped valleys V-index number are above this value. Of the 919 valleys, 591 (64%) exhibited a V-index above 0.10 and are interpreted to be previously glaciated while 328 exhibited values below 0.10 and are considered to be non-glacial V-shaped valleys.

The power form law equation fitted to the cross-sectional profiles yielded a b value on average of 2.47 with a 1σ of 1.24. These values were equally proportional to the v-index with some outliers (Table 1). It is important to note that the b value is an average of both sides of the valley

as power law fitting can only describe half of a parabolic curve. The average power from law b values for the left and right side of the valleys were 2.54 with a 1σ of 1.88 and 2.41 with a 1σ of 1.54 respectively. The majority (665) of valley cross-sections have power form law b values approaching 1.80, indicative of glacial U-shaped valleys. The 254 remaining valleys have b values < 1.80 and therefore are considered V-shaped valleys likely produced and/or modified by fluvial processes (Table 1).

The quadratic equation best fit calculations for all valleys average is $7.57x10^{-05}$ with a 1σ $6.59x10^{-05}$ within the study area. U-shaped valleys average quadratic best fit equal to $8.09x10^{-5}$ with a 1σ of $6.64x10^{-5}$. V-shaped valleys have a quadratic fit value of $2.71x10^{-5}$ and a 1σ of $3.18x10^{-5}$ (Table 1).

3.3.3 Valley Morphometry Distribution

Plotting the V-index to elevation (Fig. 2a) shows a positive correlation between increasing V-index values and elevation. The trend line plotted for all cross sections is $y = 4x10^{-05}x + 0.3651$ with an $R^2 = 0.058$. Furthermore, the relationship between power b averages to elevation (Fig. 2b) shows a slight positive correlation of increasing b values and elevation. The trend line for power b averages to elevation is $y = 0.0001x + 2.6499$ with an R^2 value of 0.0068.

Table 1. Cross Section V-Index Geomorphic Statistics

Region	Total Valley #	Glaciated	Total V-index (Average)	1σ	Total Power Fit (Average)	1σ	Total Quadradic Fit (Average)	1σ	Average Valley relief (m)	Average Valley Width (m)	Average Ratio (Relief / Width)	Average Valley Bottom Elevation (m)
		Glaciated	0.34	0.11	2.93	1.17	8.09E-05	6.635E-05				
Mars Equator	919	Nonglaciated	-0.01	0.12	1.36	0.39	2.712E-05	3.181E-05				
Study Area		Total	0.30	0.16	2.47	1.24	7.570E-05	6.588E-05	1,876	4,831	39%	-2,321
		Glaciated	0.19	0.16	1.56	0.59	1.45E-03	1.59E-03				
Earth	6858	Nonglaciated	0.06	0.37	1.19	0.37	1.93E-03	1.74E-03				
Sierra Nevada		Total	0.13	0.27	1.38	0.48	1.69E-03	1.68E-03	275	1,375	20%	2,105
Earth / Mars Ratio (Totals)	13%		42%	-	56%	-	2231%	-	15%	28%	52%	-

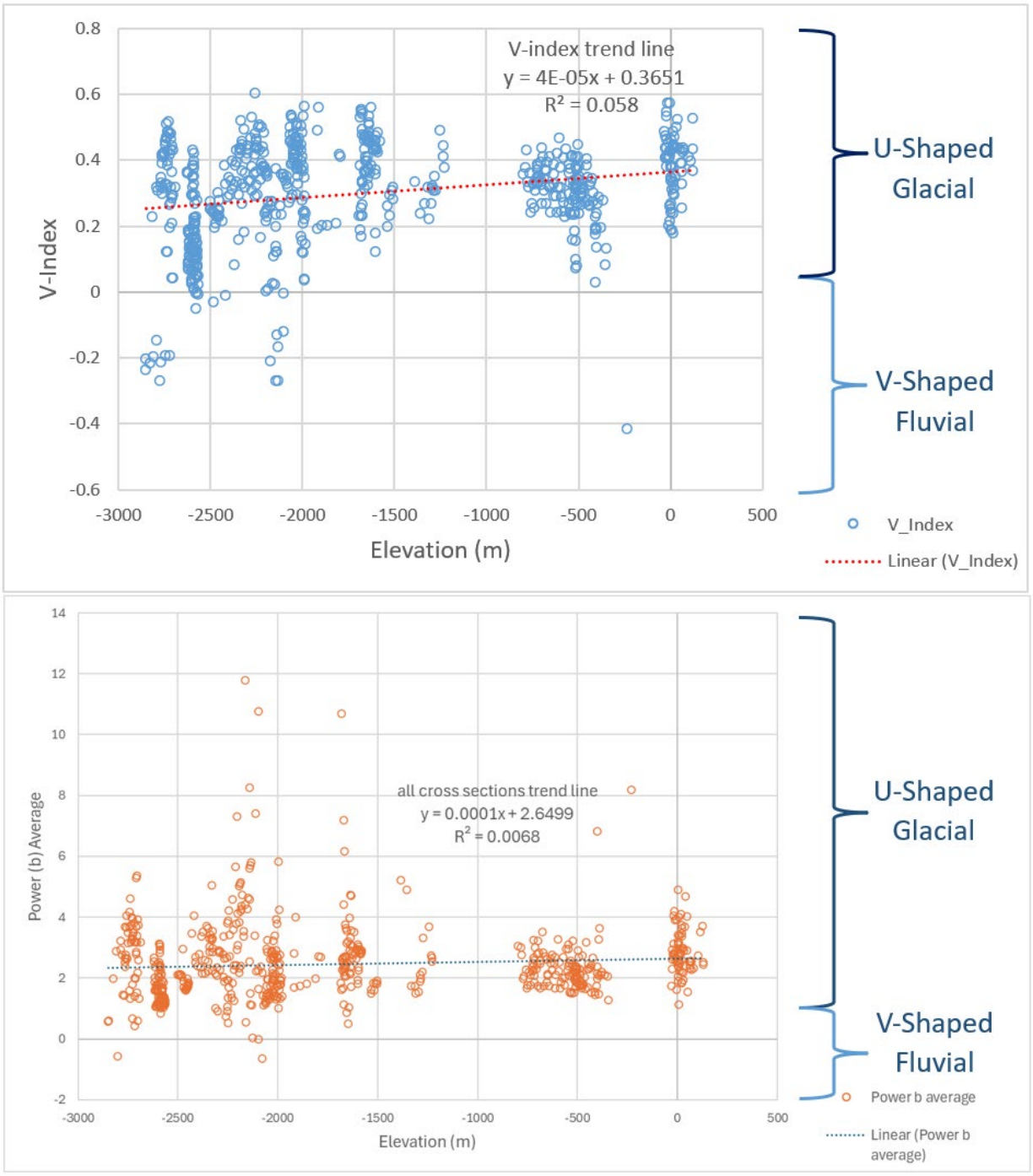

Figure 2. a) Relationship between V-index and elevation in the study area. Valley V-index (blue circles) and V-index trend line shown in (dashed red line). Data does indicate a positive correlation between elevation and increasing U-shaped cross-sectional form. The trendline (R^2) of 0.058 for Martian V-index is similar to terrestrial V-index for glaciated valleys study (0.060). **b)** Relationship

between power b average and elevation in the study area. Valley power b average (orange circles) and power b average trendline (dashed blue line). Data indicates slight correlation between power b average values and elevation with a trendline R^2 of 0.0068.

3.4 Discussion/Interpretation

The analysis of valley cross sections is an established technique for evaluating the effects of glacial erosion for terrestrial valleys, however, issues commonly arise with automatic valley morphometric extraction and analysis due to valley wall irregularities and poor quadratic and power form valley fit. Therefore, the V-index was created by Zimmer and Gabet (2018) to help solve this problem. In this study, we use the V-index method that was originally developed to fit terrestrial valley morphometry to classical parabolic curves. The use of this previously validated method brings a new semi-automated technique of assessing past valley glacial modification by extracting and quantifying valley morphometric variability in bulk from Martian digital elevation models (DEMs).

The majority of the calculated v-index values for the twenty-eight valleys assessed within our study area align well to values associated with terrestrial valleys known to have been modified by glacial processes. The average V-index for the Martian valley cross section is larger (0.30) than the terrestrial analogs (average = 0.13) (Table 1), indicating that either Martian valleys represent a more ideal parabola or that the box shaped valley cross section could drive the V-index to higher values. It is also important to note that Martian valleys are on average 28% wider with 15% more vertical relief than their terrestrial counterparts (Table 1). This has been observed on other valleys (Banks et al., 2008) and glacially derived landforms (Williams et al., 2023a) on Mars and could be due to a combination of glacier dynamics act under lower gravity

or differences in lithologic strength of the valley material. Form ratios (relief/width) for the Martian valleys studied were on average 39%, while terrestrial analogs approximately 20% (Table 1). Thus, Martian valleys are larger and deeper than documented terrestrial analogs (Zimmer & Gabet, 2018). Boxed shaped valleys with a flat floor have also been observed and characterized by within the Argyre Planitia, Mars (Banks et al. 2008). One likely mechanism for this box shaped form is infilling after the primary glacial modification occurred, or potentially from differences in lithologic strength between the valley floor and walls. It is also possible, but less likely given the form profiles observed for these martian valleys, that other formative processes such as catastrophic flooding events (Baker & Milton, 1974; Banks et al., 2008; Rodríguez et al., 2014) escarpment recession, volcanic activity, and mass wasting may have produced these U-shaped forms (Sharp, 1973; Kochel & Peake, 1984).

3.4.1 Possible Martian ELA

The V-index plotted against the elevation shows a positive correlation (trend line R^2 = 0.058) of higher U-shaped valleys (glacial) with increasing elevation. Power b values plotted against elevation also showed a slight, but positive trend of increasing U-shaped valleys with elevation. This alone suggests that there could have been an Equilibrium Line Altitude (ELA) associated with these forms across the study area. A similar glaciated trendline R^2 value (0.060) was documented within the Sierra Nevada study area with an ELA associated with the last glacial maximum. A Martian ELA would only be possible with a thicker than present Martian atmosphere capable of supporting a dynamic water ice cycle however the timing of this climatic state could be anywhere from the Amazonian to the last Martian glacial maximum (LMGM) (Schon et al., 2009).

3.4.2 Aeolian modification

Many of the U-shaped valleys analyzed have a box shaped with a flat valley floor. One possible reason for this flat floor could be infilling by aeolian reworking. Today aeolian processes are by far the dominant formative agent on Mars. Evidence of aeolian reworking on some of the study areas valley floors exists in the form of yardangs and dunes. Additionally, aeolian erosion or deflation of the surface may have resulted in the shallowing and smoothing of the valley walls (Williams et al., 2022). However, most valley floors have a significant number of craters scarring the surface, suggesting that the floor was not significantly modified since cratering occurred. While it is beyond the scope of this study, these cratered surfaces could be used in a future study to ascertain the relative ages of the valley floors through crater statistics.

3.4.3 Formative scenarios

If glacial processes are the dominant formative process responsible for the Martian U-shaped valleys, then warm based glaciation would likely have produced the basal scouring observed (Baroni et al., 2008; Arnscheidt & Rothman, 2020). Other studies suggest glacial processes could have formed cirque glaciers within the study area (Williams et al., 2023a). Warm based cirque glaciers could facilitate glacial rotational flow that produced the basal scouring and over deepening traditionally seen in cirque alcoves previously documented in the study area. This type of glaciation would only be possible if the ambient atmospheric temperature was above 0 °C. This in turn would require a higher atmospheric pressure than currently found on Mars. If this was the case for the U-shaped valleys and cirque-like alcoves identified in the Williams et al., 2023 study, then this would imply an environment that was more like terrestrial analogs.

It is important to note that the past environment of Mars could have been tied to obliquity oscillation with the Martian cryosphere ebbing and waning over time. Further, obliquity oscillation could have also modified the Martian atmosphere allowing CO_2 reserves and O_2 to be released into the thickening atmosphere (Jakosky et al., 1995). It is therefore likely that the any glacial processes on the equatorial surface could have experienced both warm and cold based glaciation vacillating between the two in accordance with the obliquity oscillations. Another possible scenario is that these forms are much older and date to the Amazonian/Hesperian boundary when the Martian atmosphere was thought to be much more substantial, and the cryosphere and liquid water cycles were more active.

There are other possible formative scenarios to explain the current geomorphic expression of these valleys. One such scenario is a headward retreat of groundwater sapping features (Carr, 2001). This could, in theory, have eroded and transported large quantities of sediment and therefore could be responsible for most of the current landform geometry. Further, groundwater sapping channels or other forms of mass wasting do not completely explain transport and removal of surface and subsurface materials associated with the fretted terrain. The fretted terrain geometry and morphology could have been formed early in the planet's history, likely because of mass wasting along scarps, accompanied by water-lubricated creep of the resulting debris, and subsurface erosion and solution (Carr, 2001). The headward extension of the short tributaries could have been altered by means of mass wasting with the aid of groundwater. This is typically seen in terrestrial valleys analogs thought to have formed by sapping (Kochel & Piper, 1986). It is therefore conceivable that the resulting debris would move down valley by mass wasting and not by fluvial transport. However, this does not explain the wide shallow cirque-like amphitheaters or the U-shaped valleys. Alternatively, these U-shaped

valley forms may have been created through entirely different processes on Mars due to environmental processes and changes not typically seen on the Earth. Other postulated explanations are mega flooding or infilling of previous fluvially cut V-shaped valleys (Baker, 2009).

Previous studies suggest that groundwater sapping could be a primary formative process to explain U-shaped cross-sectional profiles of fretted valleys on Mars (Carr, 1995). However, as (Carr, 2001) notes in their study of cirque alcove depressions and concentric lobate ridges, sapping cannot account for the totality of geomorphologic features located withing our equatorial study area. Groundwater sapping is commonly observed in association with terrestrial glacial processes (Forsberg, 1996) because warm based glaciers represent sources of subglacial meltwater that can contribute to the erosion of valley walls by groundwater discharge (Davila et al., 2013).

3.4.4 Future Work

Building evidence suggests that the equatorial zone was been heavily modified by glacial processes (Rivera-Hernández & Palucis, 2019; Putnam & Palucis, 2021; Williams et al., 2023a). An obliquity driven climate change is a possible driver for a cold wet, possibly near-term climate capable of supporting glacial processes. It is therefore possible that these U-shaped valleys could have been modified by glacial processes more near term than what is currently thought. The valley floors appear to have ample crater scaring that can be measured and morphometrics extracted for crater statistics. To better understand the relative timing of glacial processes we will use crater statistics to determine the relative age of valley floor emplacement and alteration. This in turn can be used to constrain the relative timing of glacial processes at the Martian equator.

Furthermore, if these forms date younger than the Hesperian/Amazonian boundary then this would help us better understand Mars obliquity oscillation driven climate change.

3.5 Conclusions

Evidence from this and related studies supports the hypothesis that the martian cryosphere expanded equatorward during periods of high obliquity in the recent past (<3 Ga) (Head et al., 2005; Forget et al., 2006; Hepburn et al., 2019; Williams et al., 2023a). However, the timing and extent of these periods remains poorly understood (Williams et al., 2018; Williams et al., 2023b). If the U-shaped valleys forms were created through glacial processes these equatorial glaciers could be ancient, and the relative timing of their creation could be as old as the Hesperian to Amazonian transition (~3 Ga). However, these formations could have formed during the equatorward migration of the Martian cryosphere during more recent periods of high obliquity oscillations and ELA migration. If glacial processes on Mars are episodic, then the ebbing and waning of the cryosphere could be responsible for these relic glacial forms. Other glacial forms observed in the study area including cirques (Williams et al., 2023a) help support this glacial hypothesis that these forms could be chronologically tied to obliquity oscillations (>35°).

3.6 Contributions

Conceptualization, J.M.W. and L.A.S.; methodology, J.M.W. and L.A.S.; software, P.D.Z and J.M.W.; formal analysis, J.M.W., L.A.S., P.D.Z.,H.E.N.; investigation, J.M.W., L.A.S., H.E.N.; resources, L.A.S.; data curation, J.M.W.; writing—original draft preparation, J.M.W. and L.A.S.; writing—review and editing, J.M.W., L.A.S., H.E.N.; visualization, J.M.W., L.A.S.; supervision,

L.A.S.; project administration, L.A.S.; All authors have read and agreed to the published version of the manuscript.

REFERENCES

Arnscheidt, C. W., & Rothman, D. H. (2020). Routes to global glaciation. *Proceedings of the Royal Society A*, *476*(2239), 20200303.

Baker, V. R. (2001). Water and the Martian landscape. *Nature*, *412*(6843), 228-236.

Baker, V. R. (2009). Megafloods and global paleoenvironmental change on Mars and Earth. *Preservation of Random Megascale Events on Mars and Earth: Influence on Geologic History, Geological Society of America Special Paper*, *453*, 25-36.

Baker, V. R., & Milton, D. J. (1974). Erosion by catastrophic floods on Mars and Earth. *Icarus*, *23*(1), 27-41.

Bandfield, J. L. (2007). High-resolution subsurface water-ice distributions on Mars. *Nature*, *447*(7140), 64-67.

Banks, M. E., McEwen, A. S., Kargel, J. S., Baker, V. R., Strom, R. G., Mellon, M. T., Gulick, V. C., Keszthelyi, L., Herkenhoff, K. E., & Pelletier, J. D. (2008). High Resolution Imaging Science Experiment (HiRISE) observations of glacial and periglacial morphologies in the circum-Argyre Planitia highlands, Mars. *Journal of Geophysical Research: Planets*, *113*(E12).

Baroni, C., Fasano, F., Giorgetti, G., Salvatore, M. C., & Ribecai, C. (2008). The Ricker Hills tillite provides evidence of Oligocene warm-based glaciation in Victoria Land, Antarctica. *Global and Planetary Change*, *60*(3-4), 457-470.

Besse, S., & Grotheer, E. (2021). 3D IMAGING TOOLS AND GEOSPATIAL SERVICES FROM JOINT EUROPEAN-USA COLLABORATIONS.

Beyer, R. A., Alexandrov, O., & McMichael, S. (2018). The Ames Stereo Pipeline: NASA's open source software for deriving and processing terrain data. *Earth and Space Science*, *5*(9), 537-548.

Bibring, J.-P., Langevin, Y., Mustard, J. F., Poulet, F., Arvidson, R., Gendrin, A., Gondet, B., Mangold, N., Pinet, P., & Forget, F. (2006). Global mineralogical and aqueous Mars history derived from OMEGA/Mars Express data. *Science*, *312*(5772), 400-404.

Bouquety, A., Sejourné, A., Costard, F., Mercier, D., & Bouley, S. (2019). Morphometric evidence of 3.6 Ga glacial valleys and glacial cirques in martian highlands: South of Terra Sabaea. *Geomorphology*, *334*, 91-111.

Buffo, J., Ojha, L., Meyer, C., Ferrier, K., & Palucis, M. C. (2022). Revisiting subglacial hydrology as an origin for Mars' valley networks. *Earth and Planetary Science Letters*, *594*, 117699.

Bull, W. B., & McFadden, L. D. (2020). Tectonic geomorphology north and south of the Garlock fault, California. In *Geomorphology in arid regions* (pp. 115-138). Routledge.

Carr, J. R., Stokes, C., & Vieli, A. (2014). Recent retreat of major outlet glaciers on Novaya Zemlya, Russian Arctic, influenced by fjord geometry and sea-ice conditions. *Journal of Glaciology*, *60*(219), 155-170.

Carr, M., & Head, J. (2015). Martian surface/near-surface water inventory: Sources, sinks, and changes with time. *Geophysical Research Letters*, *42*(3), 726-732.

Carr, M. H. (1995). The Martian drainage system and the origin of valley networks and fretted channels. *Journal of Geophysical Research: Planets*, *100*(E4), 7479-7507.

Carr, M. H. (2001). Mars Global Surveyor observations of Martian fretted terrain. *Journal of Geophysical Research: Planets*, *106*(E10), 23571-23593.

Cassanelli, J. P., & Head, J. W. (2019). Assessing the formation of valley networks on a cold early Mars: Predictions for erosion rates and channel morphology. *Icarus*, *321*, 216-231.

Christensen, P., Engle, E., Anwar, S., Dickenshied, S., Noss, D., Gorelick, N., & Weiss-Malik, M. (2009). JMARS-a planetary GIS. AGU Fall Meeting Abstracts,

Coles, R. J. (2014). *The cross-sectional characteristics of glacial valleys and their spatial variability* University of Sheffield].

Conway, S. J., Butcher, F. E., de Haas, T., Deijns, A. A., Grindrod, P. M., & Davis, J. M. (2018). Glacial and gully erosion on Mars: A terrestrial perspective. *Geomorphology*, *318*, 26-57.

Davila, A. F., Fairén, A. G., Stokes, C. R., Platz, T., Rodriguez, A. P., Lacelle, D., Dohm, J., & Pollard, W. (2013). Evidence for Hesperian glaciation along the Martian dichotomy boundary. *Geology*, *41*(7), 755-758. https://doi.org/10.1130/g34201.1

Dickson, J. L., Head, J. W., & Marchant, D. R. (2008). Late Amazonian glaciation at the dichotomy boundary on Mars: Evidence for glacial thickness maxima and multiple glacial phases. *Geology*, *36*(5). https://doi.org/10.1130/g24382a.1

Dundas, C. M., Mellon, M. T., Posiolova, L. V., Miljković, K., Collins, G. S., Tornabene, L. L., Rangarajan, V. G., Golombek, M. P., Warner, N. H., & Daubar, I. J. (2023). A large new crater exposes the limits of water ice on Mars. *Geophysical Research Letters*, *50*(2), e2022GL100747.

Emmett, J. A., Murphy, J. R., & Kahre, M. A. (2020). Obliquity dependence of the formation of the Martian polar layered deposits. *Planetary and Space Science*, *193*, 105047.

ESRI. (2023). *ESRI Inc. ArcGIS Pro 3.2.1. Redlands, CA: Esri Inc.* In

Faillettaz, J., Funk, M., & Vagliasindi, M. (2016). Time forecast of a break-off event from a hanging glacier. *The Cryosphere*, *10*(3), 1191-1200.

Forget, F., Haberle, R., Montmessin, F., Levrard, B., & Head, J. (2006). Formation of glaciers on Mars by atmospheric precipitation at high obliquity. *Science*, *311*(5759), 368-371.

Forsberg, C. F. (1996). Possible consequences of glacially induced groundwater flow. *Global and Planetary Change*, *12*(1-4), 387-396.

Fowler, A. C., & Chapwanya, M. (2014). An instability theory for the formation of ribbed moraine, drumlins and mega-scale glacial lineations. *Proceedings of the Royal Society A: Mathematical, Physical and Engineering Sciences*, *470*(2171), 20140185.

Glasser, N. F., & Bennett, M. R. (2004). Glacial erosional landforms: origins and significance for palaeoglaciology. *Progress in physical geography*, *28*(1), 43-75.

Graf, W. L. (1970). The geomorphology of the glacial valley cross section. *Arctic and Alpine Research*, *2*(4), 303-312.

Gulick, V. C. (2001). Origin of the valley networks on Mars: A hydrological perspective. *Geomorphology*, *37*(3-4), 241-268.

Harbor, J. M. (1992). Numerical modeling of the development of U-shaped valleys by glacial erosion. *Geological Society of America Bulletin*, *104*(10), 1364-1375.

Harbor, J. M. (1995). Development of glacial-valley cross sections under conditions of spatially variable resistance to erosion. *Geomorphology*, *14*(2), 99-107.

Head, J. W., & Marchant, D. (2009). Inventory of ice-related deposits on Mars: Evidence for burial and long-term sequestration of ice in non-polar regions and implications for the water budget and climate evolution. 40th Annual Lunar and Planetary Science Conference,

Head, J. W., Marchant, D., Agnew, M., Fassett, C., & Kreslavsky, M. (2006a). Extensive valley glacier deposits in the northern mid-latitudes of Mars: Evidence for Late Amazonian obliquity-driven climate change. *Earth and Planetary Science Letters*, *241*(3-4), 663-671.

Head, J. W., & Marchant, D. R. (2003). Cold-based mountain glaciers on Mars: western Arsia Mons. *Geology*, *31*(7), 641-644.

Head, J. W., & Marchant, D. R. (2014). The climate history of early Mars: insights from the Antarctic McMurdo Dry Valleys hydrologic system. *Antarctic Science*, *26*(6), 774-800.

Head, J. W., Marchant, D. R., Agnew, M. C., Fassett, C. I., & Kreslavsky, M. A. (2006b). Extensive valley glacier deposits in the northern mid-latitudes of Mars: Evidence for Late

Amazonian obliquity-driven climate change. *Earth and Planetary Science Letters*, *241*(3-4), 663-671.

Head, J. W., Marchant, D. R., Dickson, J. L., Kress, A. M., & Baker, D. M. (2010). Northern mid-latitude glaciation in the Late Amazonian period of Mars: Criteria for the recognition of debris-covered glacier and valley glacier landsystem deposits. *Earth and Planetary Science Letters*, *294*(3-4), 306-320. https://doi.org/10.1016/j.epsl.2009.06.041

Head, J. W., Marchant, D. R., & Kreslavsky, M. A. (2008). Formation of gullies on Mars: Link to recent climate history and insolation microenvironments implicate surface water flow origin. *Proceedings of the National academy of Sciences*, *105*(36), 13258-13263.

Head, J. W., Neukum, G., Jaumann, R., Hiesinger, H., Hauber, E., Carr, M., Masson, P., Foing, B., Hoffmann, H., & Kreslavsky, M. (2005). Tropical to mid-latitude snow and ice accumulation, flow and glaciation on Mars. *Nature*, *434*(7031), 346-351.

Hepburn, A. J., Holt, T., Hubbard, B., & Ng, F. (2019). Creating HiRISE digital elevation models for Mars using the open-source Ames Stereo Pipeline. *Geoscientific Instrumentation, Methods and Data Systems*, *8*(2), 293-313.

Hirano, M., & Aniya, M. (1988). A rational explanation of cross-profile morphology for glacial valleys and of glacial valley development. *Earth Surface Processes and Landforms*, *13*(8), 707-716.

Hobbs, S., Clarke, J., & Paull, D. (2016). Analysis of crater valleys, Noachis Terra, Mars: Evidence of fluvial and glacial processes. *Geomorphology*, *261*, 244-272.

Holo, S. J., Kite, E. S., & Robbins, S. J. (2018). Mars obliquity history constrained by elliptic crater orientations. *Earth and Planetary Science Letters*, *496*, 206-214.

Hubbard, B., Milliken, R. E., Kargel, J. S., Limaye, A., & Souness, C. (2011). Geomorphological characterisation and interpretation of a mid-latitude glacier-like form: Hellas Planitia, Mars. *Icarus*, *211*(1), 330-346. https://doi.org/10.1016/j.icarus.2010.10.021

Hubbard, B., Souness, C., & Brough, S. (2014). Glacier-like forms on Mars. *The Cryosphere*, *8*(6), 2047-2061. https://doi.org/10.5194/tc-8-2047-2014

Irwin III, R. P., Watters, T. R., Howard, A. D., & Zimbelman, J. R. (2004). Sedimentary resurfacing and fretted terrain development along the crustal dichotomy boundary, Aeolis Mensae, Mars. *Journal of Geophysical Research: Planets*, *109*(E9).

Jakosky, B. M., Henderson, B. G., & Mellon, M. T. (1995). Chaotic obliquity and the nature of the Martian climate. *Journal of Geophysical Research: Planets*, *100*(E1), 1579-1584.

James, L. A. (1996). Polynomial and power functions for glacial valley cross-section morphology. *Earth Surface Processes and Landforms*, *21*(5), 413-432.

James, L. A. (2003). Glacial erosion and geomorphology in the northwest Sierra Nevada, CA. *Geomorphology*, *55*(1-4), 283-303.

Kereszturi, A. (2005). Cross-sectional and longitudinal profiles of valleys and channels in Xanthe Terra on Mars. *Journal of Geophysical Research: Planets*, *110*(E12).

Kochel, R. C., & Peake, R. T. (1984). Quantification of waste morphology in Martian fretted terrain. *Journal of Geophysical Research: Solid Earth*, *89*(S01), C336-C350.

Kochel, R. C., & Piper, J. F. (1986). Morphology of large valleys on Hawaii: Evidence for groundwater sapping and comparisons with Martian valleys. *Journal of Geophysical Research: Solid Earth*, *91*(B13), E175-E192.

Lange, L., Forget, F., Vincendon, M., Spiga, A., Vos, E., Aharonson, O., Millour, E., Bierjon, A., & Vandemeulebrouck, R. (2023). A reappraisal of subtropical subsurface water ice stability on Mars. *Geophysical Research Letters*, *50*(21), e2023GL105177.

Lucchitta, B. K. (1984). Ice and debris in the fretted terrain, Mars. *Journal of Geophysical Research: Solid Earth*, *89*(S02), B409-B418.

Ma, Y., Xiao, Z., Luo, F., Cao, W., & Xu, R. (2023). SHARAD observations for layered ejecta deposits formed by late-Amazonian-aged impact craters at low latitudes of Mars. *Icarus*, *404*, 115689.

Madeleine, J.-B., Forget, F., Head, J. W., Levrard, B., Montmessin, F., & Millour, E. (2009). Amazonian northern mid-latitude glaciation on Mars: A proposed climate scenario. *Icarus*, *203*(2), 390-405.

Malin, M. C., Bell III, J. F., Cantor, B. A., Caplinger, M. A., Calvin, W. M., Clancy, R. T., Edgett, K. S., Edwards, L., Haberle, R. M., & James, P. B. (2007). Context camera investigation on board the Mars Reconnaissance Orbiter. *Journal of Geophysical Research: Planets*, *112*(E5).

Melosh, H. J. (2011). *Planetary surface processes* (Vol. 13). Cambridge University Press.

Montgomery, D. R. (2002). Valley formation by fluvial and glacial erosion. *Geology*, *30*(11), 1047-1050.

Morgan, A. M., Wilson, S. A., & Howard, A. D. (2022). The global distribution and morphologic characteristics of fan-shaped sedimentary landforms on Mars. *Icarus*, *385*, 115137.

Morgan, G. A., Head, J. W., & Marchant, D. R. (2011). Preservation of Late Amazonian Mars ice and water-related deposits in a unique crater environment in Noachis Terra: Age relationships between lobate debris tongues and gullies. *Icarus*, *211*(1), 347-365.

Morgan, G. A., Putzig, N. E., Perry, M. R., Sizemore, H. G., Bramson, A. M., Petersen, E. I., Bain, Z. M., Baker, D. M., Mastrogiuseppe, M., & Hoover, R. H. (2021). Availability of subsurface water-ice resources in the northern mid-latitudes of Mars. *Nature Astronomy*, *5*(3), 230-236.

Muller, J.-P., Tao, Y., Putri, A. R. D., & Conway, S. J. (2021). 3D MULTI-RESOLUTION MAPPING OF MARS USING CASP-GO ON HRSC, CRISM, CTX AND HIRISE. *The International Archives of the Photogrammetry, Remote Sensing and Spatial Information Sciences*, *43*, 667-671.

Neukum, G., Jaumann, R., Hoffmann, H., Hauber, E., Head, J., Basilevsky, A., Ivanov, B., Werner, S., Van Gasselt, S., & Murray, J. (2004). Recent and episodic volcanic and glacial activity on Mars revealed by the High Resolution Stereo Camera. *Nature*, *432*(7020), 971-979.

Palacios, D., Rodríguez-Mena, M., Fernández-Fernández, J. M., Schimmelpfennig, I., Tanarro, L. M., Zamorano, J. J., Andrés, N., Úbeda, J., Sæmundsson, Þ., & Brynjólfsson, S. (2021). Reversible glacial-periglacial transition in response to climate changes and paraglacial dynamics: a case study from Héðinsdalsjökull (northern Iceland). *Geomorphology*, *388*, 107787.

Pelletier, J. D., Comeau, D., & Kargel, J. (2010). Controls of glacial valley spacing on Earth and Mars. *Geomorphology*, *116*(1-2), 189-201.

Putnam, A. R., & Palucis, M. (2021). The Hydrogeomorphic History of Garu Crater: Implications and Constraints on the Timing of Large Late-Stage Lakes in the Gale Crater Region. *Journal of Geophysical Research: Planets*, *126*(5), e2020JE006688.

Putzig, N. E., Morgan, G. A., Sizemore, H. G., Hollibaugh Baker, D. M., Petersen, E. I., Pathare, A. V., Dundas, C. M., Bramson, A. M., Courville, S. W., & Perry, M. R. (2023). Ice resource mapping on Mars. In *Handbook of space resources* (pp. 583-616). Springer.

Qin, X., Ren, X., Wang, X., Liu, J., Wu, H., Zeng, X., Sun, Y., Chen, Z., Zhang, S., & Zhang, Y. (2023). Modern water at low latitudes on Mars: Potential evidence from dune surfaces. *Science Advances*, *9*(17), eadd8868.

Rivera-Hernández, F., & Palucis, M. C. (2019). Do deltas along the crustal dichotomy boundary of Mars in the Gale crater region record a northern ocean? *Geophysical Research Letters*, *46*(15), 8689-8699.

Rodríguez, J. A. P., Gulick, V. C., Baker, V. R., Platz, T., Fairén, A. G., Miyamoto, H., Kargel, J. S., Rice, J. W., & Glines, N. (2014). Evidence for Middle Amazonian catastrophic flooding and glaciation on Mars. *Icarus*, *242*, 202-210.

Scanlon, K., Head, J., & Marchant, D. (2015). Remnant Buried Ice in the Arsia Mons Fan-Shaped Deposit, Mars. Lunar and Planetary Science Conference,

Schon, S. C., Head, J. W., & Milliken, R. E. (2009). A recent ice age on Mars: Evidence for climate oscillations from regional layering in mid-latitude mantling deposits. *Geophysical Research Letters*, *36*(15).

Schorghofer, N., & Forget, F. (2012). History and anatomy of subsurface ice on Mars. *Icarus*, *220*(2), 1112-1120.

Sharp, R. P. (1973). Mars: Fretted and chaotic terrains. *Journal of Geophysical Research*, *78*(20), 4073-4083.

Shean, D. E. (2005). Origin and evolution of a cold-based tropical mountain glacier on Mars: The Pavonis Mons fan-shaped deposit. *Journal of Geophysical Research*, *110*(E5). https://doi.org/10.1029/2004je002360

Souness, C. J., & Hubbard, B. (2013). An alternative interpretation of late Amazonian ice flow: Protonilus Mensae, Mars. *Icarus*, *225*(1), 495-505.

Squyres, S. W. (1978). Martian fretted terrain: Flow of erosional debris. *Icarus*, *34*(3), 600-613.

Squyres, S. W. (1979). The distribution of lobate debris aprons and similar flows on Mars. *Journal of Geophysical Research: Solid Earth*, *84*(B14), 8087-8096.

Squyres, S. W., Clifford, S., Kuzmin, R., Zimbelman, J. R., & Costard, F. (1992). Ice in the martian megaregolith. *Mars*.

Svensson, H. (1959). Is the cross-section of a glacial valley a parabola? *Journal of Glaciology*, *3*(25), 362-363.

Wheeler, D. A. (1984). Using parabolas to describe the cross-sections of glaciated valleys. *Earth Surface Processes and Landforms*, *9*(4), 391-394.

Williams, J., Scuderi, L., McClanahan, T., Banks, M., & Baker, D. (2023a). Comparative Planetology – Comparing cirques on Mars and Earth using a CNN. *Geomorphology*.

Williams, J., Scuderi, L., McClanahan, T., Banks, M., & Baker, D. (2023b). Computer Automation for Identification and Morphometric Extraction of Cirque Glaciers on Mars. Proceedings of the Lunar and Planetary Science Conference, The Woodlands, TX, USA,

Williams, J. P., van der Bogert, C. H., Pathare, A. V., Michael, G. G., Kirchoff, M. R., & Hiesinger, H. (2018). Dating very young planetary surfaces from crater statistics: A review of issues and challenges. *Meteoritics & Planetary Science*, *53*(4), 554-582.

Williams, R. M., & Phillips, R. J. (2001). Morphometric measurements of Martian valley networks from Mars Orbiter Laser Altimeter (MOLA) data. *Journal of Geophysical Research: Planets*, *106*(E10), 23737-23751.

Zimmer, P. D., & Gabet, E. J. (2018). Assessing glacial modification of bedrock valleys using a novel approach. *Geomorphology*, *318*, 336-347.